Nanomechanical and Phononic Properties of Structured Soft Materials

Dissertation

zur Erlangung des Grades

‘Doktor der Naturwissenschaften’

(Dr. rer. nat.)
im Promotionsfach Chemie

am Fachbereich Chemie, Pharmazie und Geowissenschaften
der Johannes Gutenberg–Universität Mainz

vorgelegt von

Nikolaos Gomopoulos (M. Sc.)

geboren in Athen, Griechenland

Mainz, 2009

Die vorliegende Arbeit wurde im Zeitraum von September 2006 bis November 2009 am Max-Planck-Institut fr Polymerforschung in Mainz unter der Anleitung von Herrn Prof. Dr. xxxxx xxxxx und Herrn Prof. Dr. x xxxx angefertigt.

Tag der mündlichen Prüfung:	dd.mm.2009
Dekan:	Prof. Dr. xxxxxxxx
Erster Berichterstatter:	Prof. Dr. xxxxxxxxxx
Zweiter Berichterstatter:	Prof. Dr. xxxxxxxxxxx

Contents

Abstract

Significant interest in nanotechnology, is stimulated by the fact that materials exhibit qualitative changes of properties when their dimensions approach ”finite-sizes”. Quantization of electronic, optical and acoustic energies at the nanoscale provides novel functions, with interests spanning from electronics and photonics to biology. The present dissertation involves the application of Brillouin light scattering (BLS) to quantify and utilize material displacements for probing phononics and elastic properties of structured systems with dimensions comparable to the wavelength of visible light. The interplay of wave propagation with materials exhibiting spatial inhomogenities at sub-micron length scales provides information not only about elastic properties but also about structural organization at those length scales. In addition the vector nature of q allows, for addressing the directional dependence of thermomechanical properties. To meet this goal, one-dimensional confined nanostructures and a biological system possessing high hierarchical organization were investigated. These applications extend the capabilities of BLS from a characterization tool for thin films to a method for unraveling intriguing phononic properties in more complex systems.

1. Introduction

Moving forward in the development of new and miniaturized components in the age of nanotechnology, polymers have played integral roles in advanced materials fabrication in which feature sizes are equal to or much less than the wavelength of visible light. The emerging fields of microelectronics and photonics are largely predicated on the ability to construct mechanical, electrical and optical devices with sub-micrometer dimensions. Polymers are increasingly finding specialized applications in which the structures on nanometer scales create novel or improved materials properties. In fact, a recent explosion of nanotechnology has taken place across materials science, spanning from biomedical to microelectronics and photonic applications. Significant challenges exist for understanding how polymers behave when confined to dimensions near their own size. From a theoretical perspective, surface and interface effects start to dominate bulk properties in high surface area nanostructures. Experimentally, it is difficult to probe such quantities as glass transition temperature or mechanical moduli of such microscopic features. New opportunities for engineering at the nanoscale arise from these size-dependent optical, electronic, magnetic, or mechanical properties [1, 2].

Just as quantum confinement introduces novel properties in semiconductors and metals [3, 4], material confinement can induce qualitative changes in small molecule and polymeric glass formers. Many properties subject to so-called "finite-size" and chain confinement effects have been studied, from mass density and thermal expansion to surface dynamics [5, 6] and glass transition temperature [7–10]. In most polymers, a characteristic length scale is the diameter of a chain molecule, with typical random coil end-to-end radius in the range of $\sim$5-50 nm. Thus, it is expected that thickness dependent behavior appears in structures as large as 50-100 nm. Evidence for dimension dependent properties of amorphous polymers has been observed in measurements of the glass transition temperature, T_g. Several research groups have reported that for thin films T_g can be significantly different from the corresponding bulk value [7]. In the bulk, transport properties such as diffusion coefficient increases by several orders of magnitude in the narrow range of temperature over which the material undergoes a transition from a glass to a rubber [11, 12]. Similarly, mechanical properties such as the Young's modulus decrease by two to four orders of magnitude over this same temperature range.

Although the dimension dependence of T_g is now fairly well documented, less is known about the relaxation behavior and mechanical properties of polymers that are likely also dimension dependent [13–16]. The elastic moduli of amorphous polymeric glasses have traditionally been characterized at length scales at which the material is treated as a mechanically homogeneous continuum. Atomic-level studies of metallic glasses or polycrystalline materials have shown that such systems become spatially and mechanically heterogeneous at atomistic length scales. In the particular case of glassy polymers however, the length scale at which

mechanical heterogeneities occur is not known. These findings are of interest in light of recent experimental observations related to the existence of dynamic heterogeneities in glasses, which are believed to arise at comparable length scales. The origin of dynamic heterogeneities is not well understood, but it is plausible to expect them to be driven by heterogeneities of the stress. It is therefore of great interest to determine whether local mechanical properties are correlated with the rates of local molecular relaxation.

One-dimensionally confined nanostructures represent potential candidates for studying these effects. The dramatically increased surface-to-volume ratio and the restriction on the chain conformation in the film thickness direction are believed to influence the mobility of the molecules and consequently lead to different viscoelastic properties of the thin film compared to the bulk . Interactions between polymers and interfaces become more pronounced when confinement takes place at length scales near polymer's equilibrium dimensions. The concept of local density is often comprised in studies of polymer's heterogeneities at interfaces [17] and based on that, the presence of thin layers of different density and thus different stiffness localized at the boundaries of the film have been reported [18]. This spatial discontinuity near the polymer interfaces could result in a stress gradient that introduces orientation variation in the thickness of the film, thus leading to a directional dependence of the elastic constants.

It has been realized that the properties of a material depend not only on its dimension but also on its composition. The control and improvement of the physical properties often involves processes from the simple combination of homogeneous phases to the complex fabrication of intricate structural designs, resulting in systems with effective properties significantly different from those corresponding to the constitutive blocks. In addition a wide range of novel phenomena has been realized related. For example, composite materials with specially designed periodic variation of dielectric constant, or photonic crystals [19–28], offer the possibility of complete control over light propagation. Soon after the birth of this emerging field of light manipulation, theoretical work embarked on the propagation of acoustic waves in structures with periodic variations of density and/ or sound velocities, these structures are coined phononic crystals [29–33] by analogy with their optical counterparts. A major effort is the search for phononic bandgaps that forbid the propagation of acoustic waves within certain energy ranges. Phononic crystals could achieve the same level of control over elastic energy as photonic crystals do on light and semiconductors on electrons.

Recently, self-assembly and lithography techniques made it possible to fabricate and control periodic structures at nanoscale comparable to wavelength of light. Hypersonic phononic crystals that operate at gigahertz (GHz) frequency regions are extremely interesting since they possess potential for various simultaneous controls of light and sound. In most cases, acousto-optical techniques have been employed to investigate the phonon dispersion relations of hypersonic phononic crystals. The first experimental observation of a hypersonic phononic bandgap in three-dimensional colloidal composite materials has been reported by Cheng et al [34]. Tuning the bandgap was possible by using different infiltrate materials and particle sizes. Furthermore, Still et al. have discovered two hypersonic phononic handgaps of different coexisting nature in three-dimensional colloidal films [35]. One is a Bragg gap occuring at the edge of the first Brillouin zone and the other is a hybridization gap of crystalline and

amorphous films, which originates from interaction of particle eigenmodes with the acoustic effective-medium band.

New technologies are finding ways to mimic the amazing functionality of biological nanostructures. The packaging and release mechanisms of the capsid shells of viruses, as well as their monodispersity, shape, size and multivalent, site-specific surface functionality make them attractive for a broad array of applications, ranging from targeted drug delivery and gene therapy, to templates for complex photonic (figure 1a) and electronic materials [36–41]. Cylindrical viruses offer controlled, uniform anisotropy, an elusive characteristic for nanoparticles and have been utilized as templates for metallic and semi-conducting nanowires and as scaffolds for nanoparticle arrays with potential as data storage devices [42], light-harvesting systems[43], and batteries [44, 45]. Studies of photonics in nature reveal diverse examples of sub- wavelength structural features that create observed colors through thin layered or multilayered interference, diffraction, zero order diffraction, and light scattering. Iridescent beetles (figure 1b), butterflies, certain sea organisms, and many birds derive their color from the interaction of light with the structure or morphology.

As advances in nanotechnology lead to novel materials properties, a realm of nano-biotechnology is emerging, in which emphasis is being placed on understanding the structure-function complex relationships of biological nanostructures. For example the strength and toughness (among other remarkable properties such as torsional shape memory) of spider dragline silk (figure 1c) outperforms the best synthetic fibers, yet, little is known about its structure. The proper use of biological systems for various applications depends on a number of characteristics, including the mechanical properties of the building blocks and their assemblies. As a template for material synthesis, the mechanical properties ultimately determine the structure stability and durability, thus define the useful process and performance window of these biological systems. As with polymeric nanostructures, development of analytical methods is necessary for accurate testing of mechanical properties of biological structures at the nanoscale.

Novel applications at the nanoscale require reliable characterization of materials properties, for both basic understanding and technological advancement. At the fundamental level, the variety of findings for size-dependent properties are leading to stimulating discussions, experiments and theories regarding confinement, molecular dynamics and the glass transition phenomenon. On the practical side, nanostructures fabricated in the semiconductor industry demand a reliable technique to characterize mechanical properties, as pattern collapse continues to hinder miniaturization. New bio-inspired technologies are investigating the use of biological macromolecules and complexes (e.g. viruses) for self assembling templates. These are just few examples of the astounding growth in nanotechnology that rely on the ability to characterize materials properties at the level of single assembly units. The number of variables affecting the behavior of materials at the nanoscale creates a strong demand for reliable metrologies to quantify mechanical properties.

It is the scope of the present thesis to introduce Brillouin spectroscopy as a versatile method to obtain a multitude of information from the mechanical properties of nanostructures to elastic wave's propagation in inhomogeneous medium. Brillouin light scattering yields inelastic

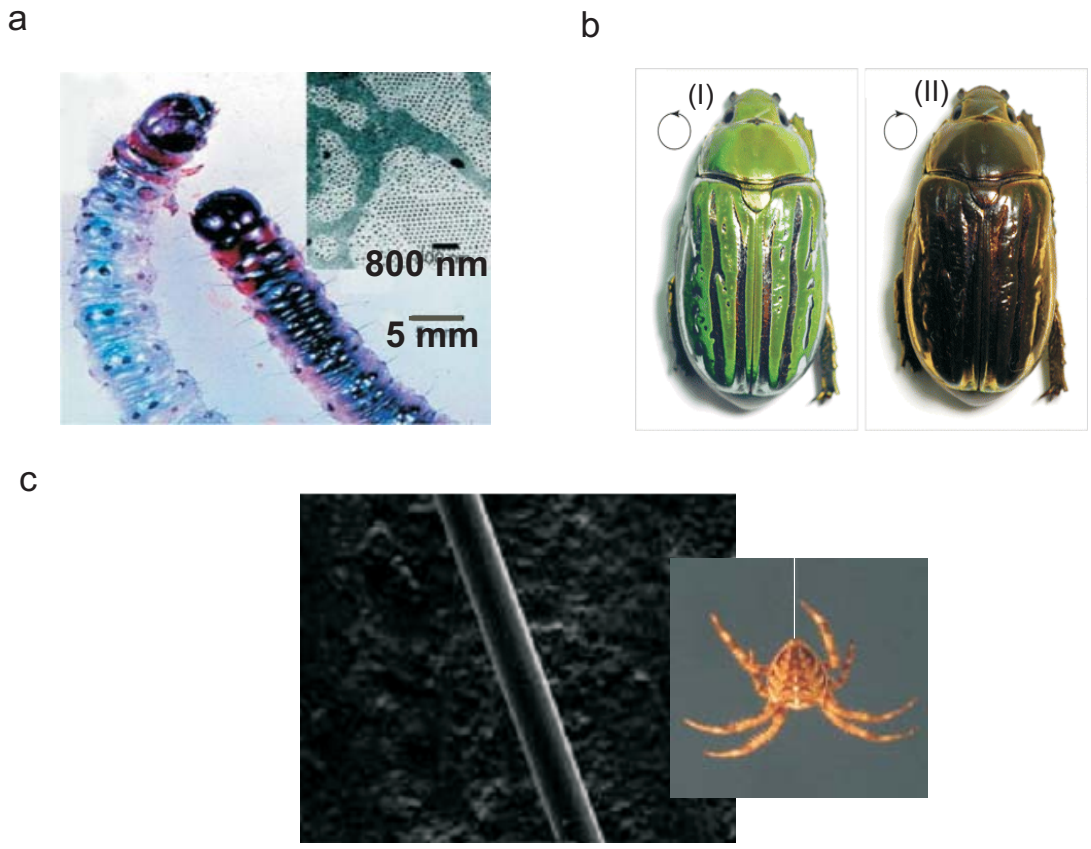

Figure 1.1.: **a,** Larvae of the greater maxmoth, Galleria mellonella, uninfected (right) and infected (left) with WIV. The close-packed structure of WIV in the cell cytoplasm (inset) causes the highly infected larva to display slight discoloration and very-faint iridescence. **b,** Photographs of the beetle C. gloriosa. (I) The bright green color, with silver stripes as seen in unpolarized light or with a left circular polarizer. (II) The green color is mostly lost when seen with a right circular polarizer.**c,**Scanning electronmicrograph of a dragline. The thread's unusual torsional propertiesprevent an abseiling spider from swinging, a movement that might attract predators(inset).

frequency shifts of light energy scattered from thermally excited acoustic phonons with submicron wavelengths λ. Structures with critical dimensions near or below λ_{phonon} will display a rich Brillouin spectrum of modes related to the mechanical properties of the structure. Although wavelengths lie in the range of 500 nm, visible light is used to probe materials with sub-100 nm dimensions. BLS avoids the complications of and improves upon techniques that require physical manipulation of nanoscale materials or the use of short wavelength ener-

gies. Probing the interplay of elastic energy propagation with meso and nanoscopic structures would contribute to deeper insights into the fundamental problem of elastic wave propagation in inhomogeneous systems.

The thesis is organized in the following way: Chapter 2 introduces the theoretical background of elastic wave propagation and the physical principles of the BLS method. The experimental technique used in this work is then reviewed. This includes instrumentation and settings for Brillouin light scattering from bulk and confined systems where boundaries are present. Chapter 3 presents the moduli directional dependence studies in thin films. In Chapter 4, the utility of Brillouin spectroscopy is extended from thin films to periodic polymer stacks. Propagating and localized vibrations are observed that provide a means to monitor modulus of single nanolayers as a function of thickness and periodicity. Furthermore the phononics of a hybrid multilayer film are studied and compared to the behavior of the previous system. Finally, Chapter 5 describes the use of Brillouin light scattering to measure the mechanical properties of a biomaterial and gain information about its complex structural organization.

2. Methodology

2.1. Elastic Waves in Solids

2.1.1. Basic Concepts

The deformation of a solid body under external forces is followed by structural arrangements which originate from internal stresses that tend to restore the body to equilibrium [46]. The total internal force on a closed volume V can be represented by $\int_V \mathbf{F}dV$, with $\mathbf{F}$ being the force per unit volume and $\mathbf{F}dV$ the force on a volume element dV in V. By applying Gauss's divergence theorem we have

$$\int_V \mathbf{F}dV = \int_S \mathbf{n}\boldsymbol{\sigma}dS \tag{2.1}$$

Here $\mathbf{F}$ is expressed as the divergence of a second rank tensor , the stress tensor $\boldsymbol{\sigma}$

$$\mathbf{F} = \nabla\boldsymbol{\sigma} \tag{2.2}$$

The stress tensor completely characterizes the state of stress of the solid body at any given point P. That is, compeletely defines the forces per unit area acting on the faces of a cubic volume element located at a ponit P within the solid body. The distance between any two infinitesimally adjacent points in the undeformed and deformed state is given by

$$dl = \sqrt{dx_i^2} \tag{2.3}$$

$$dl' = \sqrt{dx_i'^2} \tag{2.4}$$

and by introducing the displacement vector $\boldsymbol{u}$

$$\boldsymbol{u} = \boldsymbol{r} - \boldsymbol{r}' \tag{2.5}$$

with $\boldsymbol{r}$, $\boldsymbol{r}'$ the position vectors before and after the deformation,we obtain

$$dl^{'2} = dl^2 + 2\frac{\partial u_i}{\partial x_k}dx_i dx_k + \frac{\partial u_i}{\partial x_k}\frac{\partial u_i}{\partial x_l}dx_k dx_l \tag{2.6}$$

For small deformations the higher order terms in equation 2.6 can be ignored, therefore

$$dl^{'2} = dl^2 + 2\frac{\partial u_i}{\partial x_k}dx_i dx_k \tag{2.7}$$

Defining a second-rank tensor u_{ik} as

$$u_{ik} = \frac{1}{2}\left(\frac{\partial u_i}{\partial x_k} + \frac{\partial u_k}{\partial x_i}\right) \tag{2.8}$$

equation 2.7 becomes

$$dl^{'2} = dl^2 + 2u_{ik}dx_i dx_k \tag{2.9}$$

The tensor u_{ik} is called the strain tensor and from its definition is self evident that is a symmetrical tensor, that is u_{ik}= u_{ki}

For a perfectly elastic body, Hook's law can be generalized to state that each component of stress is linearly related to each component of strain, namely

$$\sigma_{ik} = c_{iklm}u_{lm} \tag{2.10}$$

where c_{iklm} is a fourth-rank tensor called the elastic constant tensor or stiffness tensor. In the most general case, c_{iklm} has 81 components. The number of independent components in the stiffness tensor is determined by the material symmetry and for general anisotropic materials is reduced to 21 , as a result of the following symmetry relations,

$$c_{iklm} = c_{kilm} = c_{ikml} = c_{lmik} \tag{2.11}$$

For systems that exhibit transverse isotropic symetry, i.e. the in and out of plane elastic constants are different, the above number is further reduced to 5. In that case the stiffness tensor has the form

$$\boldsymbol{c} = \begin{pmatrix} c_{11} & c_{12} & c_{13} & 0 & 0 & 0 \\ c_{12} & c_{11} & c_{13} & 0 & 0 & 0 \\ c_{13} & c_{13} & c_{33} & 0 & 0 & 0 \\ 0 & 0 & 0 & c_{44} & 0 & 0 \\ 0 & 0 & 0 & 0 & c_{44} & 0 \\ 0 & 0 & 0 & 0 & 0 & c_{66} \end{pmatrix} \tag{2.12}$$

where the tensor component c_{66} is given by

$$c_{66} = \frac{1}{2}(c_{11} - c_{12}) \tag{2.13}$$

For an isotropic body, symmetry considerations show that the stiffness matrix has the following form

$$\boldsymbol{c} = \begin{pmatrix} c_{11} & c_{12} & c_{13} & 0 & 0 & 0 \\ c_{12} & c_{11} & c_{13} & 0 & 0 & 0 \\ c_{13} & c_{13} & c_{33} & 0 & 0 & 0 \\ 0 & 0 & 0 & c_{44} & 0 & 0 \\ 0 & 0 & 0 & 0 & c_{44} & 0 \\ 0 & 0 & 0 & 0 & 0 & c_{44} \end{pmatrix} \tag{2.14}$$

In fact, there are only two independent elastic constants as the following relation holds

$$c_{11} = c_{12} + 2c_{44} \tag{2.15}$$

Conventionally two elastic parameters, the so-called Lame$'$ coefficients λ and μ are often used to describe the elastic properties of an isotropic body. Their relation to the elastic constants is

$$\lambda = c_{11} \qquad and \qquad \mu = c_{44} \tag{2.16}$$

μ is also called shear modulus , denoted by G. Some other elastic parameters are also often encountered, e.g., the bulk modulus, the Young's modulus and the Poisson's ratio.

Bulk modulus *K* is a measure of the response of the material's change in size due to isotropic pressure, ans related to the Lame$'$ coefficients by

$$K = \lambda + \frac{2}{3}\mu \tag{2.17}$$

Young's modulus *E*, also known as tensile modulus or modulus of elasticity, is defined as the ratio of stress to strain components in a uniaxial direction of mechanical elongation or compression. In terms of the bulk and shear moduli is expressed as

$$E = \frac{9KG}{3K + G} \tag{2.18}$$

Finally ,the ratio of the lateral strain to the longitudinal strain is called the Poisson's ratio,

$$\sigma = -\frac{u_{22}}{u_{11}} = \frac{\lambda}{2(\lambda + \mu)} \tag{2.19}$$

2.1.2. Infinite Isotropic Body

The equation of motion for an elastic body can be obtained by equating the resultant force due to the internal stresses to the product of acceleration and mass per unit volume. By referring to Eq. 2.2, we have

$$\frac{\partial \sigma_{ik}}{\partial x_k} = \rho \frac{\partial^2 u_i}{\partial t^2} \tag{2.20}$$

where ρ is the density and u_i is the displacement vector. For an infinite homogeneous and isotropic medium, after applying Hook's law and adopting the Lame, coefficients representation, the equation of motion is found to have the following form

$$(\lambda + \mu)\nabla(\nabla \mathbf{u}) - \mu \nabla \times (\nabla \times \mathbf{u}) - \rho \partial_t^2 \mathbf{u} = 0 \tag{2.21}$$

In the case of a harmonic elastic wave of angular frequency ω, the displacement vector **u** can be written as

$$\mathbf{u}(\mathbf{r}, t) = Re\left[\mathbf{u}(\mathbf{r}) e^{-i\omega t}\right] \tag{2.22}$$

and Eq. 2.21 can be reduced to the following time-independent form

$$(\lambda + \mu)\nabla(\nabla \mathbf{u}) - \mu \nabla \times (\nabla \times \mathbf{u}) - \rho \omega^2 \mathbf{u} = 0 \tag{2.23}$$

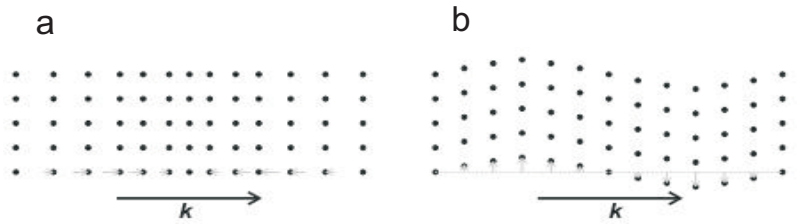

Figure 2.1.: Propagation of **a** longitudinal and **b** transverse elastic plane waves.

If the displacement vector **u** is expressed as the sum of two orthogonal vectors **u**= $\mathbf{u}_l$ + $\mathbf{u}_t$ such that

$$\nabla \times \mathbf{u}_l = 0 \qquad \text{and} \qquad \nabla \mathbf{u}_t = 0 \tag{2.24}$$

Eq. 2.23 can be decomposed into two independent Helmholtz equations of motion

$$(\nabla^2 + k_l^2)\mathbf{u}_l = 0 \tag{2.25}$$

$$(\nabla^2 + k_t^2)\mathbf{u}_t = 0 \tag{2.26}$$

Here k_l= ω_l/c_l and k_t= ω_t/c_l are the wavenumbers of the longitudinal and transverse waves, respectively. The solutions of these two equations represent two elastic waves which propagate independently: the longitudinal wave with a phase velocity $c_l = \sqrt{c_{11}/\rho} = \sqrt{(\lambda+\mu)/\rho}$, also called the longitudinal sound velocity; and $c_t = \sqrt{c_{44}/\rho} = \sqrt{\mu/\rho}$ the transverse or shear wave with a phase velocity , also called the transverse or shear sound velocity.

For the longitudinal wave the particle displacement is in the direction of wave propagation, while for the transverse one the particle displacement is perpendicular to the direction of propagationas as shown in Fig.2.1 . The transverse wave has two possible polarizations which are orthogonal to each other. Note also that the longitudinal wave involves changes in the volume of the medium, i.e. dilatation or compression of a local volume element. On the other hand, the transverse wave causes no volume change

2.1.3. Thin Layers

In the preceding discussion of the elastic wave propagation in an isotropic body, it was assumed that the body is infinitely large so that the boundary effect can be ignored. However in the case where the size of the specimen is comparable to the wavelength of the elastic wave, the existence of the boundaries will have a substantial influence on the wave propagation and

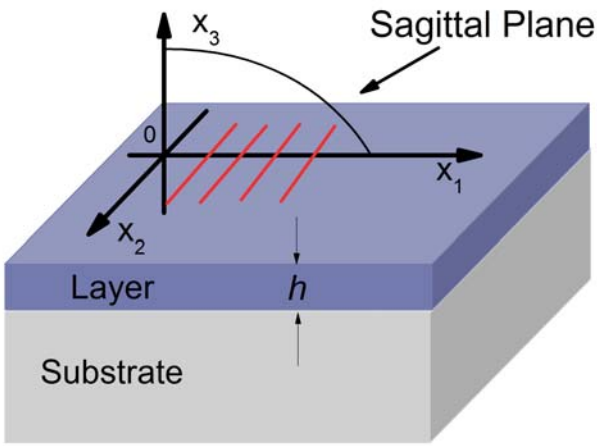

Figure 2.2.: Coordinate system for elastic wave propagation in thin layers

hence cannot be neglected. Regarding the boundary effects, an important case of much theoretical and practical interest is wave propagation in supported thin layers. This section will give a brief introduction to this subject.

Considering the following system consisting of a substrate and a thin layer on top as shown in Fig.2.2, both the substrate and the layer are infinite in the directions parallel to their interface and are treated as isotropic. It can be seen that the $x_3 = 0$ plane is the interface between the layer and the substrate while the plane $x_3 = h$ is the free surface of the layer. To study elastic waves in the thin supported layer, the wave equation 2.21 is still workable and has to be applied to both the layer and the substrate. The major difference now is that the mechanical boundary conditions must be taken into account. More explicitly, the continuity of the stress and the strain at the interface ($x_3 = 0$) and the vanishing of the stress at the free surface ($x_3 = h$)must be satisfied, which leads to much more complicated wave propagation compared to the bulk.

It is easily appreciated from symmetry considerations that the waves of interest will be "straight crested" in the sense that there are no variations of any of the displacement components in a direction parallel to the free surface and perpendicular to the direction of propagation. The direction of propagation will be taken as the x_1 direction in Fig.2.2, thus the disturbance has constant phase and amplitude for each component along any line parallel to the x_2 axis. However, the nature of the waves will be such that they decay with depth into the substrate and in general become of negligible amplitude a few wavelengths below the interface. In fact, this nature is in accordance with the assumption that the waves of interest are surface or film excitations. Therefore one is seeking for straight-crested propagating waves of the following form

$$u_i = \alpha_j \exp(ikbx_3) \exp\left[ikx_1 - vt)\right] \tag{2.27}$$

It will be seen below that *b* is in general complex and it gives, in this interpretation, the variation with depth of the amplitude and phase of the partial waves measured on a "plane of constant phase", namely, a plane perpendicular to x_1. The α_j (j=1, 2, 3) give the relative amplitudes of the different components of each partial wave.

Substituting Eq.2.27 into Eq.2.21 results in the following relation between v, *b* and α in the isotropic substrate consideration

$$\begin{bmatrix} \Gamma_{11}-\rho\nu^2 & \Gamma_{12} & \Gamma_{13} \\ \Gamma_{12} & \Gamma_{22}-\rho\nu^2 & \Gamma_{23} \\ \Gamma_{13} & \Gamma_{23} & \Gamma_{33}-\rho\nu^2 \end{bmatrix} \begin{bmatrix} \alpha_1 \\ \alpha_2 \\ \alpha_3 \end{bmatrix} = 0 \tag{2.28}$$

where $\Gamma_{11} = c_{44}\, b^2 + c_{11}$, $\Gamma_{12} = 0$, $\Gamma_{13} = (c_{11}- c_{44})b$, $\Gamma_{22} = c_{44}(\, b^2 + 1)$, $\Gamma_{23} = 0$, $\Gamma_{33} = c_{11}\, b^2 + c_{44}$

In order to have nontrivial solutions, the determinant of the square matrix in Eq.2.28 must be set equal to zero, which produces the secular equation of the form

$$\left|\Gamma_{rs} - \delta_{rs}\rho\nu^2\right| = 0 \qquad\qquad r,s = 1,2,3 \tag{2.29}$$

The sagittal-plane displacements, α_1 and α_3 of Eq.2.27, are completely uncoupled in the equations of motion from the transverse displacements, α_2. Thus, Eq.2.29 separates into two equations

$$\begin{aligned} (c_{44}b^2 + c_{44} - \rho\nu^2)(c_{11}b^2 + c_{11} - \rho\nu^2) &= 0 \\ c_{44}b^2 + c_{44} - \rho\nu^2 &= 0 \end{aligned} \tag{2.30}$$

Similar equation as Eq.2.28 can be found for the displacement components in the isotropic layer, involving layer material parameters referred to the same axes. In the final solution, all the partial waves (Eq. 2.27) in the substrate and layer will have the same phase velocity. The roots and corresponding eigenvectors for the two media are

I. For transverse motion in the substrate

$$b^{(\alpha)} = -i\left[1 - (\nu/{\nu_t}^2)\right]^{1/2} \qquad\qquad \boldsymbol{\alpha}^{(\alpha)} = [0,1,0] \tag{2.31}$$

II. For transverse motion in the layer

$$\begin{aligned} b^{(1)} &= +i\left[1 - (\nu/\widehat{\nu}_t)^2\right]^{1/2} \qquad & \boldsymbol{\alpha}^{(1)} &= [0,1,0] \\ b^{(2)} &= -i\left[1 - (\nu/\widehat{\nu}_t)^2\right]^{1/2} \qquad & \boldsymbol{\alpha}^{(2)} &= [0,1,0] \end{aligned} \tag{2.32}$$

III. For sagittal motion in the layer

$$\begin{aligned} b^{(5)} &= +i\left[1-(\nu/\widehat{\nu}_t)^2\right]^{1/2} & \boldsymbol{\alpha}^{(1)} &= \left[-b^{(5)},1,0\right] \\ b^{(6)} &= +i\left[1-(\nu/\widehat{\nu}_t)^2\right]^{1/2} & \boldsymbol{\alpha}^{(2)} &= \left[0,1,b^{(6)}\right] \\ b^{(7)} &= -i\left[1-(\nu/\widehat{\nu}_t)^2\right]^{1/2} & \boldsymbol{\alpha}^{(1)} &= \left[-b^{(7)},1,0\right] \\ b^{(8)} &= -i\left[1-(\nu/\widehat{\nu}_t)^2\right]^{1/2} & \boldsymbol{\alpha}^{(2)} &= \left[0,1,b^{(8)}\right] \end{aligned} \tag{2.33}$$

IV. For sagittal motion in the substrate

$$\begin{aligned} b^{(c)} &= +i\left[1-(\nu/\widehat{\nu}_t)^2\right]^{1/2} & \boldsymbol{\alpha}^{(1)} &= \left[-b^{(c)},1,0\right] \\ b^{(d)} &= -i\left[1-(\nu/\widehat{\nu}_t)^2\right]^{1/2} & \boldsymbol{\alpha}^{(2)} &= \left[0,1,b^{(d)}\right] \end{aligned} \tag{2.34}$$

where $\nu_t = (c_{44}/\rho)^{1/2}$ and $\widehat{\nu}_t = (\widehat{c}_{44}/\widehat{\rho})^{1/2}$ are the transverse sound velocities for bulk waves in the substrate and the layer, respectively, while $\nu_l = (c_{11}/\rho)^{1/2}$ and $\widehat{\nu}_l = (\widehat{c}_{11}/\widehat{\rho})^{1/2}$ are the corresponding bulk longitudinal sound velocities. Notice that for the substrate only values of *b* lying in the lower half of the complex plane are retained, as the solutions desired (Eq.2.27) are to represent surface waves.

Under the isotropic assumption, it can be easily shown that the boundary-condition equations also separate into two uncoupled sets, one set involving roots α, 1 and 2 and hence the in-plane (x_1x_2-plane) displacement components only, and the second set involving the roots 5, 6, 7, 8, *c*, and *d* and thereby sagittal-plane displacements only. Thus for the isotropic case, the final solutions for elastic wave propagation in supported thin layers are divided into two categories:

I. Love modes
II. Lamb modes

Love modes have only in-plane displacements, in contrast, only sagittal-plane displacements are involved in Lamb modes. Their displacements are schematically depicted in Fig.2.3. It is seen that only Lamb modes can cause interface or surface corrugation, which is important for the determination of Lamb modes on an opaque substrate by light scattering techniques thus the following discussion will be restricted to Lamb modes, since it is the Lamb modes that have been probed in this work.

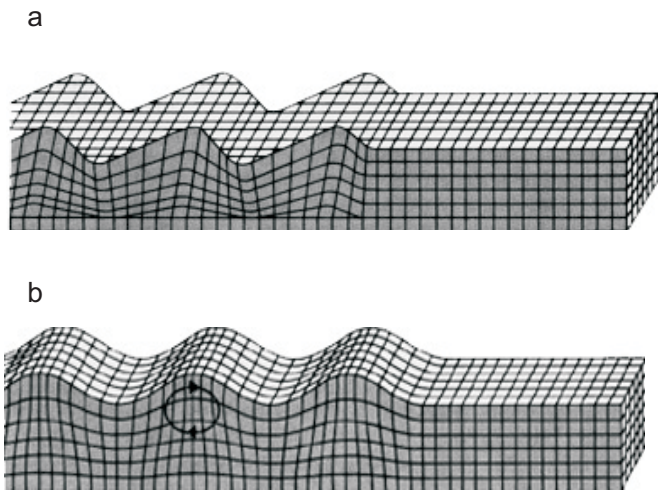

Figure 2.3.: Schematic show of the displacements of the two uncoupled surface modes. **a**, Love modes. **b**, Lamb modes.

The mechanical boundary conditions for the sagittal-plane displacements lead to the following equation:

$$\begin{bmatrix} b^{(5)} & -1 & -b^{(5)} & -1 & -b^{(c)} & 1 \\ -1 & -b^{(6)} & -1 & b^{(6)} & 1 & b^{(d)} \\ 1-b^{(5)2} & 2b^{(5)} & 1-b^{(5)2} & -2b^{(5)} & -r(1-b^{(c)2}) & -2rb^{(d)} \\ 2b^{(5)} & -(1-b^{(5)2}) & -2b^{(5)} & -(1-b^{(5)2}) & -2rb^{(c)} & r(1-b^{(c)2}) \\ (1-b^{(5)2})e^{(ikb^{(5)}h)} & 2b^{(6)}e^{(ikb^{(6)}h)} & (1-b^{(5)2})e^{(-ikb^{(5)}h)} & -2b^{(6)}e^{(-ikb^{(6)}h)} & 0 & 0 \\ 2b^{(5)}e^{(ikb^{(5)}h)} & -(1-b^{(5)2})e^{(ikb^{(6)}h)} & -2b^{(5)}e^{(-ikb^{(5)}h)} & -(1-b^{(5)2})e^{(-ikb^{(6)}h)} & 0 & 0 \end{bmatrix} \begin{bmatrix} c_5 \\ c_6 \\ c_7 \\ c_8 \\ c_c \\ c_d \end{bmatrix} = 0 \tag{2.35}$$

Substituting Eq. 2.33 and Eq. 2.34 into Eq. 2.35 and equating the determinant of the square matrix to zero, one actually defines an implicit function, ν, which is a function of *kh*, the product of the wavenumber of the surface wave and the film thickness. This relation ν=ν(kh), is often referred to as the dispersion relation.

First, a special case will be considered, that is, the substrate has a free surface, or equivalently, the layer thickness *h*=0. In this instance, *kh* is always zero. By referring to Eq. 2.35 it can be easily seen that all the exponential terms in the square matrix will vanish and be replaced by 1. Consequently, the solution ν for a given set of elastic parameters of the substrate is a constant, which represents a non-dispersive mode, the so-called Rayleigh mode. Love modes at this time degenerate into the horizontally polarized bulk shear waves propagating parallel to the substrate surface.

With the presence of a layer on top of the substrate surface, $h \neq 0$, and the phase velocities then become *kh* dependent. We consider two cases:

I. Layer stiffens the substrate ($\widehat{\nu}_t > \nu_t$)
II. Layer loads the substrate ($\widehat{\nu}_t < \nu_t$))

When $\widehat{\nu}_t > \nu_t$, the layer is said to ”stiffen” the substrate because the presence of the layer in-

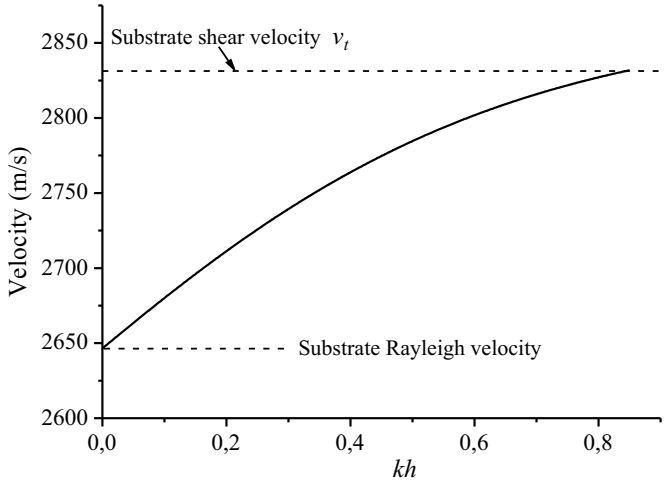

Figure 2.4.: Silicon layer on ZnO substrate, the stiffening case. ZnO: ν_l=6000 m/s, ν_t=2831 m/s, ν_R=2649 m/s; silicon: ν_l=8945 m/s, ν_t=5341 m/s, ν_R=4890 m/s.

creases the surface wave velocity above that of the Rayleigh velocity of the substrate, whereas when $\widehat{\nu}_t < \nu_t$), the layer is said to "load" the substrate because the velocity of the free-surface Rayleigh mode on the substrate is decreased by the presence of the layer.

For the stiffening situation, it is characteristic for the dispersion curve ($\nu \sim kh$) to start from *kh*=0 at the substrate Rayleigh velocity and increase until the substrate shear velocity is reached at a particular value of *kh*; for larger values of *kh* this mode of propagation does not exist. For the material combination of this type, only one Lamb mode can propagate and that only for a limited range of *kh*. An example of the dispersion curve of this type is given in Fig. 2.4 for a silicon layer on a ZnO substrate.

When the layer loads the substrate, a significant feature is the existence of an unlimited number of higher order Lamb modes, sometimes also called Sezawa modes [47]. In this case, the dispersion curve for the first Lamb mode, often referred to simply as Rayleigh mode, starts with negative slope at the Rayleigh velocity of the substrate, for *kh*=0. As *kh* increases, the phase velocity continues to decrease and for layer thickness large compared to the wavelength, $kh \gg 1$, it tends asymptotically to the Rayleigh velocity of a free surface of the layer material. The higher order Lamb modes all have a low frequency cutoff at which the phase velocity is equal to the substrate shear velocity. Their phase velocities also decrease with increasing kh and have a high frequency asymptote at the layer shear velocity. An example of the dispersion relation of this type of material combination is given in Fig.2.5 for a ZnO layer on a silicon substrate.

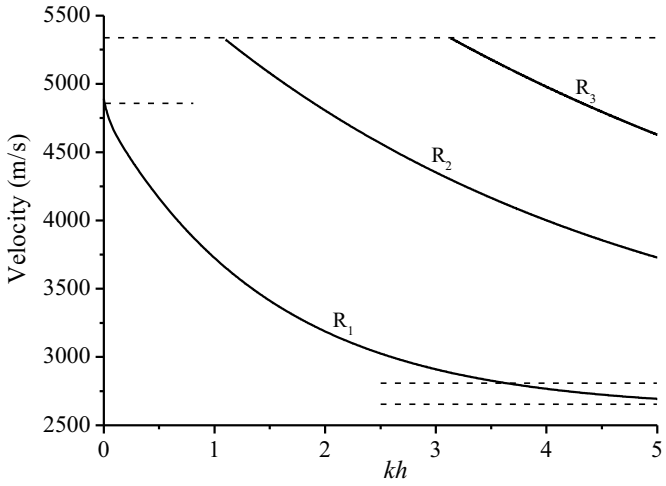

Figure 2.5.: ZnO layer on silicon substrate, the loading case. Only the first three Lamb modes (R1, R2 and R3) are shown.

2.2. Light scattering

Visible light spectroscopies are useful tools for studying materials properties. For example, molecular dynamics, chemical composition, and acoustic mode velocities can be analyzed using light scattering. In bulk materials, spectroscopy techniques probe discrete energy levels within a continuous distribution of energies based on selection rules. Energy levels within nanostructured materials, in contrast, are quantized due to geometrical confinement. Material length scales on the order of the excitation wavelength induce novel electronic, optical, and phononic characteristics. Therefore, spectroscopy provides a logical means to study quantized energies of nanostructures.

2.2.1. Fundamental light scattering theory

The optical property of an isotropic medium (nonmagnetic, nonconducting, nonabsorbing) is usually characterized by the dielectric constant ϵ_0. This is an average value since the dielectric constant associated with a local volume is actually fluctuating around ϵ_0 owing to the thermal motion of the molecules of the medium. Taking into account possible anisotropy introduced by the fluctuation of the relative orientations of anisotropic molecules, the local dielectric constant, in its most general form, becomes a tensor quantity, and can be written as

$$\boldsymbol{\epsilon}_(\mathbf{r},t) = \epsilon_0\mathbf{I} + \delta\epsilon(\mathbf{r},t) \tag{2.36}$$

where $\delta\epsilon(\mathbf{r},t)$ is the dielectric constant fluctuation tensor at position $\mathbf{r}$ and time t, $\mathbf{I}$ is the second-rank unit tensor. For an incident plane wave of the form

$$\mathbf{E}_i(\mathbf{r},t) = \mathbf{n}_i E_0 \exp i(\mathbf{k}_i\mathbf{r} - \omega_i t) \tag{2.37}$$

where $\mathbf{n}_i$ is a unit vector in the direction of the incident electric field, E_0 is the field amplitude, $\mathbf{k}_i$ is the wave vector, and ω_i is the angular frequency. The scattered electric field $\mathbf{E}_s(\mathbf{R},t)$ at a large distance *R* from the scattering volume can be computed by demanding that the total field $\mathbf{E} = \mathbf{E}_i + \mathbf{E}_s$ satisfy the Maxwell equations throughout all space.

The component of the scattered electric field at a large distance *R* from the scattering volume with polarization $\mathbf{n}_s$, propagation vector $\mathbf{k}_s$, and frequency ω_s is

$$E_s(R,t) = \frac{E_0}{4\pi R\epsilon_0} \exp ik_s R \int_V d^3r \exp i(\mathbf{qr} - \omega t) \left[\mathbf{n}_s \left[\mathbf{k}_s \times (\mathbf{k}_s \times (\delta\boldsymbol{\epsilon}(\mathbf{r},t)\mathbf{n}_i))\right]\right] \tag{2.38}$$

In Fig. 2.6 a large portion of the scattering volume *V* is indicated by the irregular region in gray, *O* inside the scattering volume is the origin of the established reference coordinate system. The detector of the scattered light is located at the position **R** with respect to the origin, *r* is the position of an infinitesimal volume element inside the scattering volume, and the distance vector between the volume element and the detector is given by $\boldsymbol{R} - \boldsymbol{r}$, here $R \gg r$ (2.6 a). The so-called scattering wavevector **q** is defined as the vector difference between the wavevector of the incident light ($\mathbf{k}_i$) and that of the scattered light ($\mathbf{k}_s$), whose magnitude can be readily calculated as follows by referring to 2.6 b

$$\begin{aligned} q^2 &= |\mathbf{k}_s - \mathbf{k}_i|^2 = k_s^2 - k_i^2 - 2\mathbf{k}_i\mathbf{k}_s = 2k_i^2 - 2k_i^2\cos(\theta) = 4k_i^2 \sin^2\frac{\theta}{2} \\ q &= 2k_i \sin\frac{\theta}{2} = \frac{4\pi n}{\lambda_i}\sin\frac{\theta}{2} \end{aligned} \tag{2.39}$$

In the above, the equality $|\mathbf{k}_i| \cong |\mathbf{k}_s|$ was used , since the incident wavelenght has negligible changes in the scattering process.

In Eq. 2.38, the integration is performed over the whole space within the scattering volume *V*, and it only influences terms in the integrand containing the space coordinates **r**. Eq. 2.38 can be then rewritten as

$$E_s(R,t) = \frac{E_0}{4\pi R\epsilon_0} \exp i(k_s R - \omega_i t) \left[\mathbf{n}_s \left[\mathbf{k}_s \times (\mathbf{k}_s \times ((\int_V d^3r \exp i\mathbf{qr}\delta\boldsymbol{\epsilon}(\mathbf{r},t))\mathbf{n}_i))\right]\right] \tag{2.40}$$

The term $\frac{E_0}{4\pi R\epsilon_0} \exp i(k_s R - \omega_i t)$ represents a spherical wave emitted from the origin O in the scattering volume. The integral $\int_V d^3r \exp i\mathbf{qr}\delta\boldsymbol{\epsilon}(\mathbf{r},t)$ accounts for the interference effect between the wavelets emitted from different volume elements within the finite scattering volume and is actually the spatial Fourier transformation of the dielectric fluctuation $\delta\boldsymbol{\epsilon}(\mathbf{r},t)$

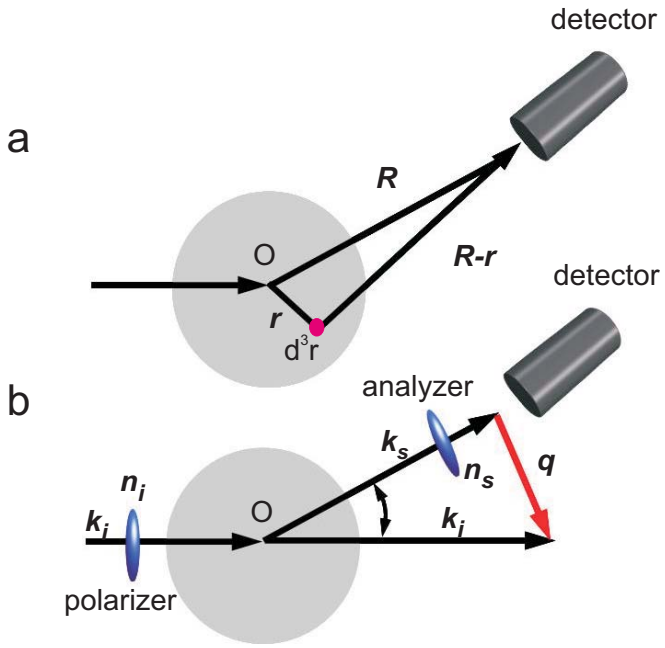

Figure 2.6.: Scheme of light scattering geometry. **a**, The relative position of the scattering volume V and the detector,where the gray region denotes a large portion of the scattering volume. The total scattered field at the detector is the superposition of the fields radiated from all infinitesimal volumes d^3r at position $\boldsymbol{r}$ with respect to the center of the scattering volume. **b**, The light scattering process. The incident light impinges onto the sample and is scattered in all directions. The position of the detector determines the scattering geometry which further defines the scattering wavevector $\boldsymbol{q}$= $\mathbf{k}_i$-$\mathbf{k}_s$. The polarizer and the analyzer are used to select the polarization state of the incident and the scattered light, respectively.

$$\delta\boldsymbol{\epsilon}(\mathbf{q},t) = \int_V d^3r \exp i\mathbf{q}\mathbf{r}\delta\boldsymbol{\epsilon}(\mathbf{r},t) \tag{2.41}$$

Eq. 2.40 then becomes

$$E_s(R,t) = \frac{E_0}{4\pi R\epsilon_0} \exp i(k_s R - \omega_i t)\,[\mathbf{n}_s\,[\mathbf{k}_s \times (\mathbf{k}_s \times (\delta\boldsymbol{\epsilon}(\mathbf{q},t)\mathbf{n}_i))]] \tag{2.42}$$

or by working out the vector product Eq. 2.42 can be simplified

$$E_s(R,t) = \frac{-k_s^2 E_0}{4\pi R\epsilon_0} \exp i(k_s R - \omega_i t)\delta\epsilon_{is}(\mathbf{q},t) \tag{2.43}$$

where $\delta\epsilon_{is}(\mathbf{q},t) = \mathbf{n}_s\delta\boldsymbol{\epsilon}(\mathbf{q},t)\mathbf{n}_i$ is the component of the dielectric constant fluctuation tensor along the initial and final polarization directions.

The time-correlation function of E_s can be computed as

$$\langle E_s^*(R,0)E_s(R,t)\rangle = \frac{k_s^4E_0^2}{16\pi^2R^2\epsilon_0^2}\langle\delta\epsilon_{is}^*(\mathbf{q},0)\delta\epsilon_{is}(\mathbf{q},t)\rangle\exp i(-\omega_i t) \tag{2.44}$$

The spectral density of the scattered light reads

$$\begin{aligned} I_{is}(\mathbf{q},\omega_s,R) &= \int dt\exp i\omega_s t\,\langle E_s^*(R,0)E_s(R,t)\rangle \\ &= \frac{k_s^4E_0^2}{16\pi^2R^2\epsilon_0^2}\int dt\,\langle\delta\epsilon_{is}^*(\mathbf{q},0)\delta\epsilon_{is}(\mathbf{q},t)\rangle\exp i(\omega_s-\omega_i t) \\ &= \frac{k_s^4E_0^2}{16\pi^2R^2\epsilon_0^2}\int dt\,\langle\delta\epsilon_{is}^*(\mathbf{q},0)\delta\epsilon_{is}(\mathbf{q},t)\rangle\exp i(\omega t) \end{aligned} \tag{2.45}$$

where $\omega = \omega_s - \omega_i$ is the frequency shift in the scattering process, and $I_0 = E_0^2$is the incident beam intensity.

For a given scattering experiment, the proportionality coefficient in Eq.2.45 is a constant and the scattering intensity is then determined by the integral which is the spectral density of the dielectric constant fluctuations

$$I_{is}(\mathbf{q},\omega) = \int dt\,\langle\delta\epsilon_{is}^*(\mathbf{q},0)\delta\epsilon_{is}(\mathbf{q},t)\rangle\exp i\omega t \tag{2.46}$$

If $\delta\epsilon_{is}(\mathbf{q},t)$ is time-independent, then has non-zero values only when ω= 0. This means that ”frozen” fluctuations (static optical inhomogeneities) can only lead to elastic scattering, in which the frequency of the scattered wave coincides to the frequency of the incident wave. The frequency changes only when $\delta\epsilon_{is}(\mathbf{q},t)$ varies with time.

From the above discussion it is easy to appreciate that the light scattering spectrum $I_{is}(\mathbf{q},\omega)$ directly measures the local dielectric constant fluctuations in a medium, which is in turn caused by various thermal fluctuations, e.g. density fluctuations, and or orientation fluctuations for anisotropic molecules. Therefore light scattering can in principle provide valuable information about diverse dynamic processes in a system.

2.2.2. BLS theory

Brillouin scattering can be understood as the inelastic scattering of incident energy by thermally excited elastic waves, or acoustic phonons, in a sample.It is often described as a scattering event following criteria for Braggs Law and the Doppler Effect.That is, the total momen-

tum and energy between the incident energy and excitation (phonon), must be conserved in the scattering process. These two conservation laws can be more easily appreciated by viewing the scattering event in terms of inelastic photon-phonon collisions. An incident photon with energy $h\omega_i$ and momentum $h\mathbf{k}_i$ is inelastically scattered by a phonon of energy $h\omega$ and momentum $h\mathbf{k}$ in the scattering medium. During this process a phonon is either created with the scattered photon losing the corresponding energy, or annihilated with the scattered photon gaining the corresponding energy. Conservations of momentum and energy in the scattering process require

$$h\mathbf{k}_s = h\mathbf{k}_i \pm h\mathbf{q} \qquad Momentum \qquad conservation \tag{2.47}$$

$$h\omega_s = h\omega_i \pm h\omega \qquad Energy \qquad conservation \tag{2.48}$$

The plus sign corresponds to the phonon annihilation (anti-Stokes scattering), while the minus sign indicates the phonon creation (Stokes scattering). A phonon is an elastic analogue of a photon, that is, a piece of quantized elastic energy and in the context of this thesis, phonons are refered to high frequency (GHz) thermally excited elastic waves.

In a simple approach BLS can be pictured as constructive interference between multiply reflected light beams by sound waves. To appreciate this, let's refer to Fig.2.7 where the interaction of the incident light and the propagating sound wave is schematically depicted assuming a plane wave form with a wavelength Λ. The existence of such an elastic wave in the medium modulates the local dielectric constant which also assumes plane wave form of identical wavelength traveling along the same direction.

Due to the large discrepancy between the speed of light (3x10^8 m/s) and sound (3x10^5 m/s), at any given instant when a single light scattering event happens, the spatial variation of the dielectric constant in the medium can be regarded as "frozen", i.e. static dielectric inhomogeneities described by a spatial plane wave. The travel of the beam inside the medium is then very similar to that in a periodic multilayer stack with periodicity Λ as shown in Fig. 2.7, where the light beam undergoes multiply reflections. The maximum reflected intensity, or the scattering, will occur only when the condition for constructive interference is satisfied, namely

$$2n\Lambda \sin\frac{\theta}{2} = \lambda_i \tag{2.49}$$

where, n is the refractive index of the medium, λ_i is the wavelength of the incident light in vacuum, and θ is the angle between the incident and reflected beams. The Bragg condition, Eq. 2.49, can be rewritten as

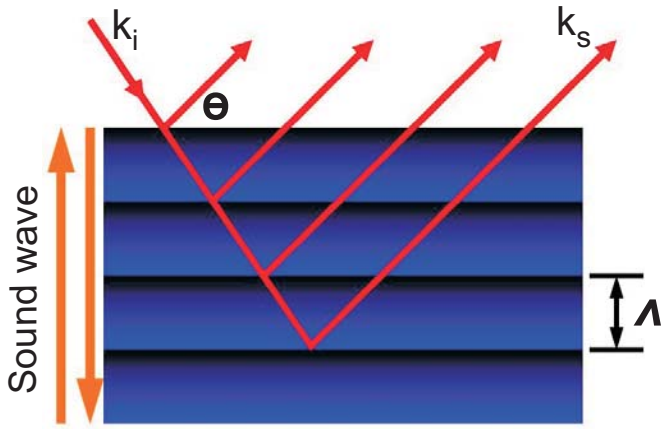

Figure 2.7.: The scattering process can be regarded as constructive interference between multiply reflected beams at the interface between two adjacent ”layers”. Each ”layer” has a thickness corresponding to the wavelength (Λ) of the sound producing the ”mutilayers”.

$$\frac{2\pi}{\Lambda} = \frac{4\pi n}{\lambda_i} \sin\frac{\theta}{2} \tag{2.50}$$

Comparing Eq. 2.50 and Eq. 2.39 we have that

$$q = \frac{2\pi}{\Lambda} \tag{2.51}$$

Eq. 2.51 indicates that the wavevector $\mathbf{k}(k = 2\pi/\Lambda)$ of the sound wave is equivalent to the scattering wavevector **q**. By changing the scattering angle θ, a different **q** is selected and correspondingly different sound waves are probed by BLS. The equality $\mathbf{q} = \mathbf{k}$ reflects the exchange of momentum between the sound wave and the light during the scattering process.

The traveling sound wave has a certain phase velocity, say ν, therefore the frequency f_s of the scattered light seen by the detector suffers a Doppler shift, that is

$$f_s = f_i(1 \pm 2\frac{\nu}{c} \sin\frac{\theta}{2}) \tag{2.52}$$

where f_i is incident light frequency and $c = f_i\lambda_i/n$ is the velocity of light within the scattering medium. The plus and minus signs correspond to the two possible propagation directions of the sound wave: one is toward the detector (+) leading to an increase in the frequency of the scattered light (anti-Stokes scattering), the other is away from the detector (-) leading to a frequency decrease (Stokes scattering). Eq. 2.52 can be further simplified to

$$\begin{aligned} f_s &= f_i \pm \frac{2\nu}{c}\frac{4\pi n}{\lambda_i}\sin\frac{\theta}{2}) \\ &= f_i \pm \frac{\nu}{2\pi}q \end{aligned} \tag{2.53}$$

In terms of angular frequency

$$\omega = \omega_s - \omega_i = \pm\nu q \tag{2.54}$$

From the above it is clear that in the scattering spectrum $I_{is}(\mathbf{q},\omega)$ there is a doublet centered at the frequency $\omega = \pm\nu q$. Since q is also the wavenumber of the sound wave (Eq. 2.51) traveling at a speed ν, then ω naturally becomes the angular frequency of the sound wave. Therefore Eq. 2.54 reflects the energy exchange between the sound wave and the light.

2.3. Utilities of Optical Spectroscopy

The frequency shift involved in BLS generally ranges from 10^9 to 10^{11} Hz. This is rather small compared to the incident laser frequency in the visible spectrum which lies on the order of 10^{14} Hz. To achieve such a high spectroscopic resolution, the frequently encountered diffraction grating spectrometers widely used in Raman scattering and fluorescence spectroscopy do not suffice. Spectrometers based on the Fabry-Perot (FP) interferometer have to be used. The FP interferometer, capable of providing extremely high resolving power, is the most crucial element of the whole BLS experimental setup.

2.3.1. Standard Fabry-Perot Interferometer

The FP interferometer is a multiple beam interferometer and in its simplest configuration consists of two planes, parallel and highly reflected surfaces separated by some distance *d*. If the enclosed gap (usually is air) can be mechanically varied by moving one of the mirrors, it's referred to as an interferometer. When the mirrors are held fixed and adjusted for parallelism by screwing down some sort of spacer, it's said to be an etalon.

In practice, two semisilvered or aluminized glass optical flats form the reflecting boundary surfaces. The introduction of a thin metal layer is to increase the reflectivity, as we have seen already that high resolving power can only be achieved with large r. In the absence of light absorption, the equation $tt' + r^2 = 1$ holds. Since in most cases it is the reflected and transmitted beam intensity that are concerned, another two useful parameters are defined, the reflectance R, the reflected fraction of the incident intensity, and the transmittance T, the transmitted fraction of the incident intensity. It can be easily shown that $R = r^2$. Following the energy conservation, obviously we have $R + T = 1$. In reality, there is always some loss

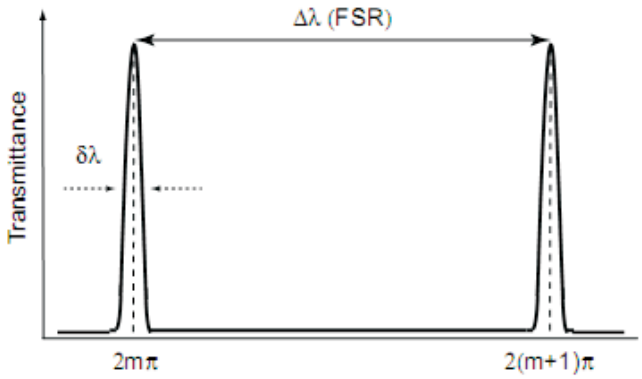

Figure 2.8.: Optical transmission function of a single-pass Fabry-Perot mirror.

of energy, e.g. transformation to heat. If the absorbed fraction, referred to as the absorptance, is denoted by *A*, the above relation then becomes $R + T + A = 1$.

The single-pass transmission function of a planer mirror Fabry-Perot interferometer can be expressed as

$$T = \frac{T_0}{1 + (4F^2/\pi^2)\sin^2(2\pi L/\lambda)} \tag{2.55}$$

where T_0 is the overall single-pass transmission, F is the effective single-pass finesse, L is the mirror spacing and λ is the wavelength of light. Eq.2.55 indicates that the FP only transmits light with wavelengths λ, satisfying the relation

$$L = \frac{1}{2}m\lambda \tag{2.56}$$

for an integer m. The optical transmission function is illustrated in fig.2.8

The width at half-maximum $\delta\lambda$, as indicated in Fig.2.8 describes how rapidly the intensity drops off on either side of the maximum. To a very good approximation, represents the smallest phase increment separating two resolvable peaks, which actually determines the resolving power of a FP interferometer. Another quantity of particular interest is the ratio of the separation of adjacent maxima to the peak width at half-maximum, known as the finesse $F = 2\pi/\gamma$. Over the visible spectrum, the finesse of most ordinary FP instruments is about 30. In practice, the finesse cannot be made much greater than about 100 due to limitations on the quality of mirror substrates and coatings, as well as deviations of the mirrors from plane parallelism. Note that as the finesse increases, the width at half-maximum decreases, thus the higher the resolving power is, but at the expense of the transmission intensity.

The FP interferometer is used as a high resolving power spectrometer by varying the spacing

d between the two mirrors so as to select light transmission at different wavelengths. Since the maximum transmission happens at $\delta/2 = (k_0 L/2)$, *m*=1,2,3,, where δ the phase difference between adjacent rays, we have

$$m\lambda_0 = 2n_f d\cos\theta_t \tag{2.57}$$

where $\lambda_0 = 2\pi/k_0$ is the light wavelength in vacuum. For nearly normal incidence,$\cos\theta_t = 1$, then

$$m\lambda_0 = 2n_f d \tag{2.58}$$

For a given spacing *d*, the transmitted light does not necessarily have the same wavelength because the change in wavelength can be compensated by the corresponding change in the integer number *m*. This makes an unambiguous interpretation of the spectrum impossible, unless it is known a priori that the spectrum of interest entirely falls into a certain wavelength span $(\Delta\lambda_0)_F SR$, the so-called free spectral range (FRS). For a fixed *d*, differentiating Eq. 2.58 leads to

$$\frac{(\Delta\lambda_0)}{\lambda_0} = -\frac{\Delta m}{m} \tag{2.59}$$

The separation between the two adjacent transmission maxima (Fig.2.8) is 2π, and the corresponding change of *m* is 1, namely, Δm=1. Therefore, Eq.2.59 becomes

$$\frac{(\Delta\lambda_0)_F SR}{\lambda_0} = -\frac{1}{m} \tag{2.60}$$

In combination with Eq. 2.58, we have

$$(\Delta\lambda_0)_{FSR} = \lambda_0^2/2n_f d \tag{2.61}$$

or in terms of frequency

$$(\Delta f_0)_{FSR} = c/2n_f d \tag{2.62}$$

where *c* is the light speed in vacuum. The FSR is a very important instrumental parameter to be set before using the FP interferometer for spectroscopic purposes.

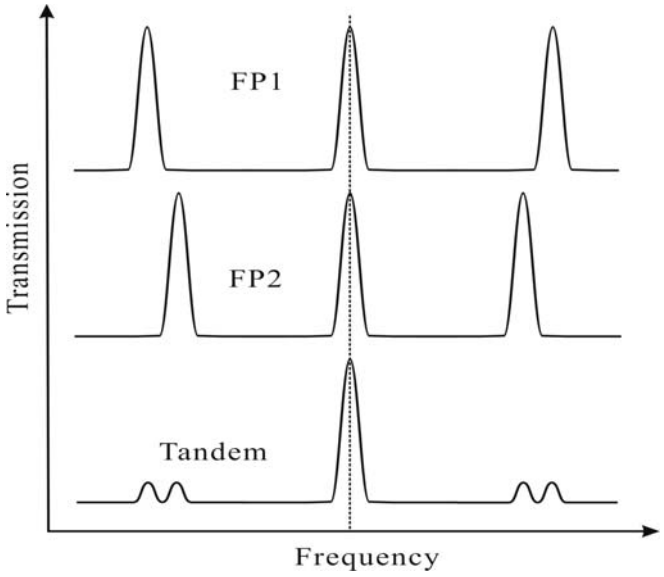

Figure 2.9.: Suppression of higher order transmission in a Tandem Fabry-Perot.

2.3.2. Tandem Fabry-Perot Interferometer

The standard FP interferometer has too low contrast to allow weak Brillouin signals to be observed in the presence of normally extremely intense elastically scattered light. This problem was overcome with the use of the high contrast, multipass FP interferometer. However, a multipass FP interferometer, like the simple configuration, still suffers from the overlapping of neighboring interference orders. which makes the interpretation of the measured spectra somewhat ambiguous, especially for rich or broad spectral features.

One solution to suppress this effect is to use a tandem arrangement, i.e. two FP interferometers (FP1 and FP2) in series with slightly different FSR. In this case, the neighboring order transmission peaks of the two FP interferometers cannot coincide due to the slight difference in their FSR as illustrated in Fig. 2.9. As a result, the adjacent interference orders of one of the two interferometers are blocked by the other, leading to a significant suppression of interference higher order transmission. In order for the tandem interferometer to function as a spectrometer, the wavelengths transmitted by the two FP combinations must satisfy the following two equations simultaneously for all wavelengths within the relevant FSR

$$\begin{aligned} m_1\lambda_0 &= 2n_f d_1 \qquad (FP1) \\ m_2\lambda_0 &= 2n_f d_2 \qquad (FP2) \end{aligned} \tag{2.63}$$

This implies that the scanning of the two FP interferometers has to be synchronized, such that

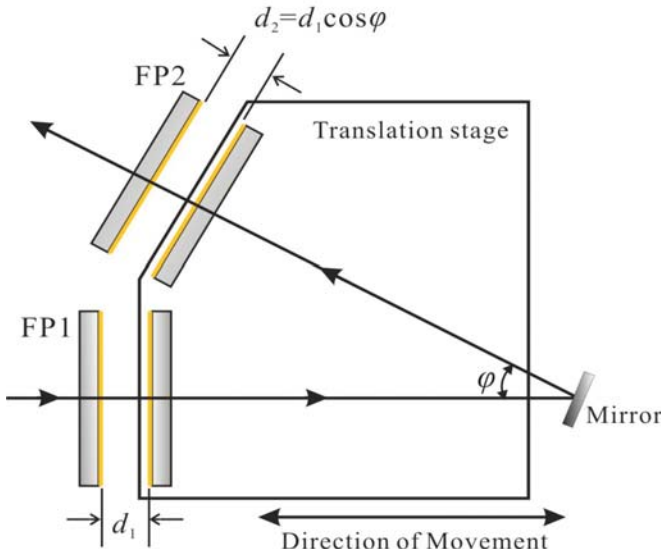

Figure 2.10.: Principle of the tandem scanning of a tandem Fabry-Perot.

$$\frac{\Delta d_1}{\Delta d_2} = \frac{d_1}{d_2} \tag{2.64}$$

The principle of the tandem scan is demonstrated in Fig.2.10. The first interferometer FP1 is arranged to lie in the direction of the translation stage movement. One mirror sits on the translation stage, the other on a separate angular orientation device. The second interferometer FP2 lies with its axis at an angle ϕ to the scan direction. One mirror is mounted on the translation stage and the other mirror on an angular orientation device which can also allow a small translation of the mirror for adjustment purposes. The relative spacings of the mirrors are set so that a movement of the translation stage to the left would bring both sets of mirrors into simultaneous contact. A movement of the translation stage to the right then sets the spacings to d_1 and $d_1 \cos\phi$. Moreover, a scan Δd_1 of the translation stage produces a change of spacing Δd_1 in FP1 and $\Delta d_1 \cos\phi$ in FP2. In other words, Eq. 2.64 is satisfied.

In the present thesis, all the experiments were carried out in a six-pass tandem Fabry-Perot. The related tandem optics configuration is briefly sketched in Fig. 2.11. The scattered light enters the system at the adjustable pinhole P1. Mirror M1 reflects the light towards the lens L1 where it is collimated and directed via mirror M2 to the first interferometer FP1. Then the light hits mirror M3 and is directed to the second interferometer FP2. After transmission through FP2 the light strikes the 90^o prism PR1 where it is reflected downwards and returned parallel to itself towards FP2. Upon the reflection by M3 it continues to pass through FP1, after transmission through lens L1 it travels underneath mirror M1 and is focused on to mirror M4. This mirror returns the light through lens L1 where it is again collimated and directed through FP1. The combination of lens L1 and mirror M4 lying at its focus acts as a spatial

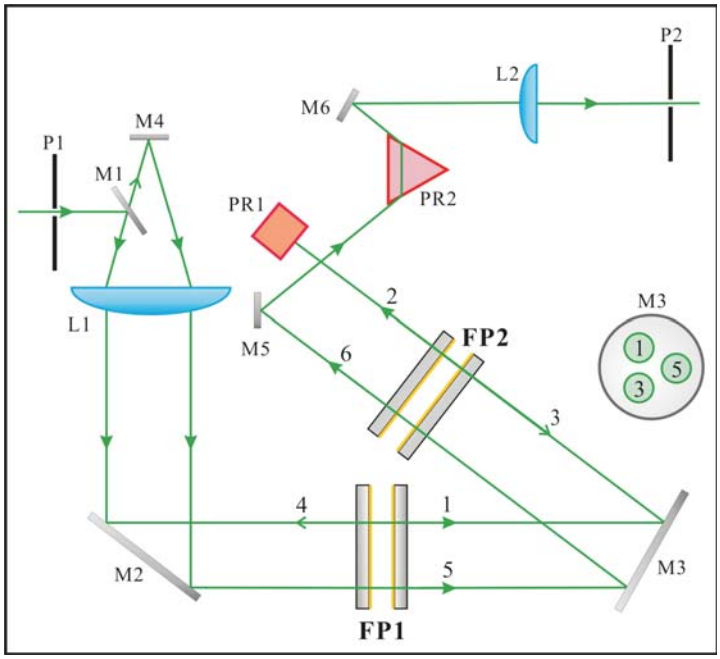

Figure 2.11.: **Optics inside a six-pass tandem Fabry-Perot interferometer**: The scattered light enters the Tandem system via the pinhole P1 and leaves via the pinhole P2. Before it finally reaches the photodetector, the scattered light passes the two interferometers (FP1 and FP2) six times.

filter which filters out unwanted beams such as the beam reflected from the rear surfaces of the interferometer mirrors. After the final pass through FP2, the light strikes mirror M5 where it is directed to the prism PR2. This prism, in combination with the mirror M6, the lens L2 and the output pinhole P2, forms a bandpass filter with a width determined by the size of the pinhole.

2.3.3. Experimental Setup

The whole BLS experimental setup is schematically shown in Fig.2.12. A solid state diode pumped, frequency-doubled Nd:YAG laser (Coherence) with output power of 100 mW (532 nm) is mounted on the rotatory arm of a goniometer (ALV). After passing through a Glan polarizer, the outcoming laser beam with polarization (V) perpendicular to the scattering plane (horizontal plane) is focused into the center of the goniometer where the sample is located. The focusing size is around 200 μm in diameter. The scattered light along a well-defined direction is collected by an aperture and focused into the entrance pinhole of the tandem Fabry-Perot (JRS Scientific Instruments) after successive transmission througth two conjugated lenses. A Glan-Thompson analyzer is inserted between the two confocal lenses to allow the selection of the scattered light with polarization either perpendicular (V) or parallel (H) to the scatter-

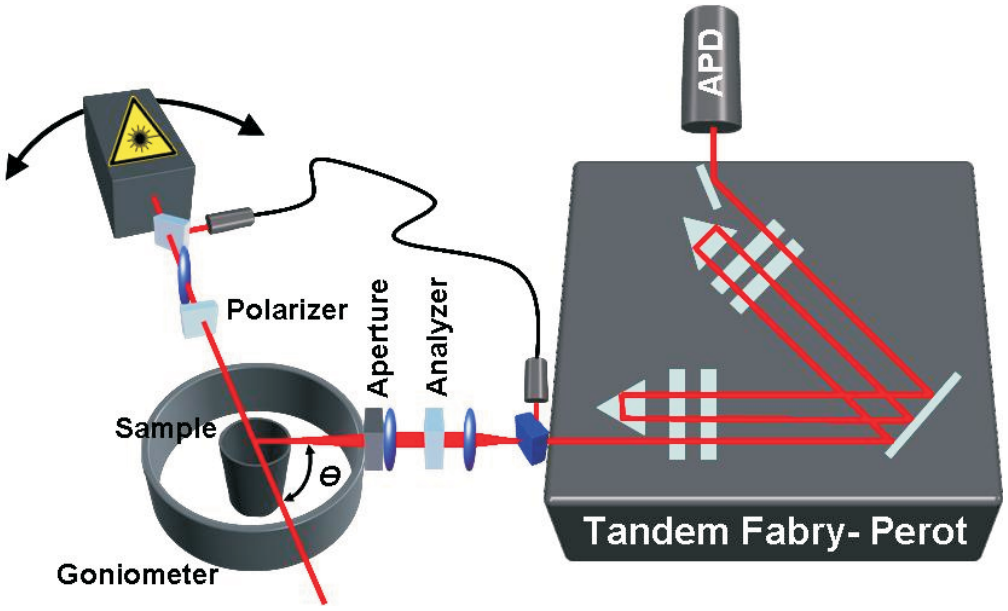

Figure 2.12.: **Scheme of the BLS setup**: The sample is sitting at the center of the goniometer, the variation of the scattering angle θ is realized by rotating the laser mounted on the goniometer. The scattered light is collected by two conjugated lenses into the six-pass tandem Fabry-Perot interferometer.

ing plane. After passing through the tandem Fabry-Perot which acts as a spectrometer, the scattered light is detected by a single-photon avalanche photodiode (APD) and the resulting electronic signal is processed by a multi-channel analyzer (MCA). A tiny fraction of the incident laser intensity is separated from the incident beam and introduced as a reference beam via an optical-fiber into the tandem Fabry-Perot to achieve a long period (up to several weeks) stabilization of the interferometer. The experimental change of the scattering angle θ, hence the scattering wavevector **q**, is accomplished by rotating the goniometer with an electronically controlled motor, which could cover a broad range, roughly from 8^o to 160^o.

For measurements of extension characteristics, a custom- build micro scale materials testing setup was used (Fig. 2.13). A special sample holder allowed BLS measurements at elevated strains. The samples were mounted onto the cross heads of the tensile instrument. Depending on the size of the sample the initial length L_0 could be adjusted. The applied strain could be controlled by a pair of micrometer screws (Mitutoyo S151-112) with a precision of 10 μm. The holder was placed on a goniometer that allowed variations of the angle between the scattering wave vector q and the plane of the sample. With a special adapter, the position of the sample could be adjusted relative to the incident laser beam thus probing elastic excitations at two different scattering geometries.

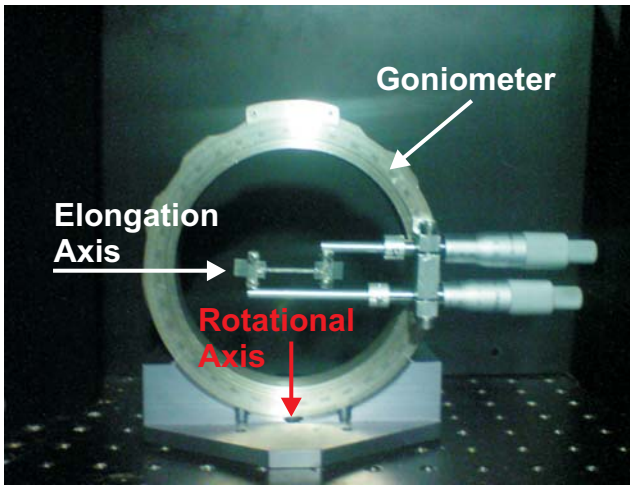

Figure 2.13.: The sample holder allowing BLS experiments to be performed at elevated strains.

2.3.4. Scattering Geometries

Selection of the scattering geometry determines the direction of elastic wave propagation. This is also a very important parameter for BLS measurements as well as the polarization of incident and scattered light. The scattering geomery can be divided into two categories difined by the direction of the incident and the scattered light as shown in Fig. 2.14. The *in-plane* phononic properties can be measured in the transmission geometry (Fig. 2.14(a)), while the *out-of-plane* phononic properties can be measured in the reflection geometry (Fig. 2.14(b)). Since two dimensional nanocomposite materials are investigated in this thesis, using both geometries is very useful to obtain information on phononic anisotropies. Therefore, most experiments described in this thesis were done in both transmission and reflection geometry.

Figure 2.14(a) shows the transmission geometry. The scattering wavevector **q** is inclined relative to the *in-plane* direction of the film.The scattering wavevector **q** is determined by the incident and scattered light in the film. By performing trigonometric operations and applying Snell's law, the scattering wavevector can be expressed as

$$q = \frac{4\pi n}{\lambda} \sin\left[\frac{1}{2}\left\{\sin^{-1}\left(\frac{1}{n}\sin\alpha\right) - \sin^{-1}\left\{\frac{1}{n}\sin(\theta-\alpha)\right\}\right\}\right] \tag{2.65}$$

$$\begin{aligned} q_{\perp} = \frac{4\pi n}{\lambda} \sin\left[\frac{1}{2}\left\{\sin^{-1}\left(\frac{1}{n}\sin\alpha\right) + \sin^{-1}\left\{\frac{1}{n}\sin(\theta-\alpha)\right\}\right\}\right] \\ \times \cos\left[\frac{1}{2}\left\{\sin^{-1}\left(\frac{1}{n}\sin\alpha\right) - \sin^{-1}\left\{\frac{1}{n}\sin(\theta-\alpha)\right\}\right\}\right] \end{aligned} \tag{2.66}$$

where $q_{\perp}$ denotes the parallel component of the scattering wavevector relative to the film. The

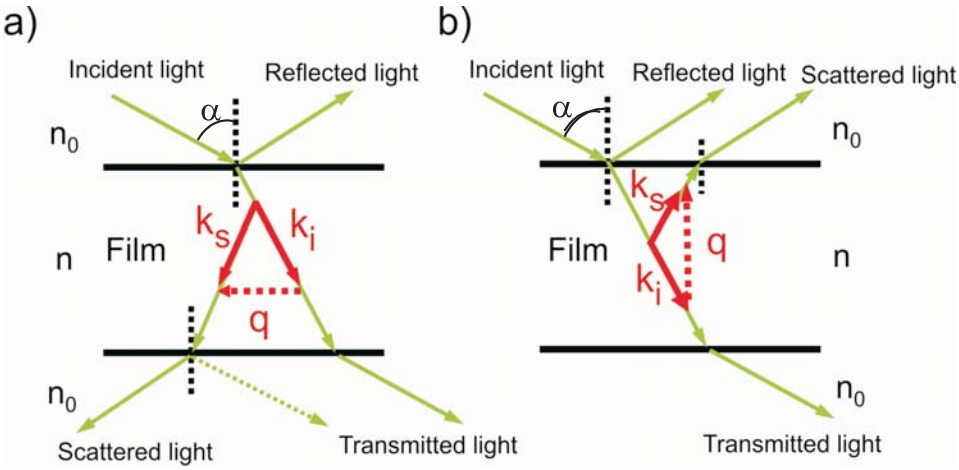

Figure 2.14.: Schematics of scattering geometry: (a) transmission geometry and (b) reflection geometry.

unique advantage of this transmission geometry is that the scattering wave vector does not depend on the refractive index of the sample due to the mutual cancellation of the refraction effects at both top and bottom interfaces of the sample. Since the ratio of $q_\perp/q$ in most cases is more than 0.9, asuuming that the incident angle is half of the scattering angle, i.e. $\alpha = \theta/2$, it can be shown that Equation 2.66 can be simplified as a form

$$q = \frac{4\pi}{\lambda} \sin\frac{\theta}{2} \tag{2.67}$$

The reflection geometry is shown in Fig. 2.14(b). Applying the same trigonometric operations and Snell's law, we can obtain

$$q = \frac{4\pi n}{\lambda} \cos\left[\frac{1}{2}\sin^{-1}\left(\frac{1}{n}\sin\alpha\right) + \frac{1}{2}\sin^{-1}\left\{\frac{1}{n}\sin(\theta+\alpha)\right\}\right] \tag{2.68}$$

$$\begin{aligned} q_{\|} = \frac{4\pi n}{\lambda} &\cos\left[\frac{1}{2}\sin^{-1}\left(\frac{1}{n}\sin\alpha\right) + \frac{1}{2}\sin^{-1}\left\{\frac{1}{n}\sin(\theta+\alpha)\right\}\right] \\ &\times \cos\left[\frac{1}{2}\sin^{-1}\left(\frac{1}{n}\sin\alpha\right) - \frac{1}{2}\sin^{-1}\left\{\frac{1}{n}\sin(\theta+\alpha)\right\}\right] \end{aligned} \tag{2.69}$$

where $q_{\|}$ denotes the perpendicular component of the scattering wavevector relative to the film. The detailed calculations of each scattering wavevector are described in appendix A.

2.4. Out of plane Elastic Excitations

The propagation character of elastic excitations strongly depends on the film's thickness. When its size becomes comparable to the wavelength of the elastic wave, existence of boundaries will have a substantial influence on the wave propagation. The finite film thickness implies a discretization of the eigenfrequencies, and this is the reason of an infinite number of different discrete branches in the dispersion diagram. In the particular case where $q_{||}$ = 0, i.e., in the direction perpendicular to the film, modes of mixed polarization are decoupled and have either purely longitudinal or purely transverse character, with corresponding eigenfrequencies that can be obtained from the standing-wave conditions. Propagating through a thin film, a single Longitudinal acoustic (LA) phonon is localized within the distance *d* from the film surface, where *d* is the film thickness. Due to the uncertainty principle, the phonon momentum forms $\Delta p \approx h$/d -wide distribution around the mean value $\hbar$q (here *h*, $\hbar$ are the Planck and reduced Planck constants, respectively). In the other terms, the wavevector *q* is not a certain value any more, but has a distribution $\Delta q \approx 2\pi/d$, and the Brillouin peak has a width $\Delta f \approx \nu$/d.

Multiple reflections of an acoustic excitation from the film surface and interface can form a standing wave. First of all, it should be noted that substantial contrast of the acoustic impedance ($Z = \rho\nu$) between the polymer film and the substrate is the necessary condition for standing wave observation . Multiphase systems with small Z mismatch between phases do not support phonon localization and exhibit an effective medium behavior .

The constructive interference (CI) of the excitations gives the existence criterion for a standing wave of the order *m*:

$$q_m d = \pi m + \frac{\pi}{2} \tag{2.70}$$

where *m* is an integer and π/2 term is the phase shift due to the reflections on film boundaries.

These sub-modes occupy the envelope of the broadened (LA) phonon mode, forming the fine structure with equal interval Δf_m between peaks given by the formula directly obtained from Eq. 2.70:

$$\Delta f_m = \frac{\nu}{2d} \tag{2.71}$$

where ν is the phase velocity for phonon propagation normal to the film.

The fine structure of the BLS spectra for a supported film can be described following similar considerations in the literature [48, 49]. For a non-absorbing film/substrate system, the light scattered at angle θ has a discrete spectrum with intensity $P_s(\vartheta)$ given by:

$$P_s(\vartheta) \propto \sum_m sinc^2\left(q(\theta)\frac{d}{2} - (2m+1)\frac{\pi}{4}\right) \tag{2.72}$$

where the *m*-th term under the sum sign corresponds to the scattering with Brillouin shift $f_m = (2m+1)\frac{\nu}{4d}$ and and sinc is the cardinal sine function sinc(x) = sin(x)/x. In the form of the frequency shift function:

$$P_s(\vartheta) \propto \sum_m sinc^2\left[\frac{\pi d}{\nu}\left(q(\theta)\frac{\nu}{2\pi} - f_m\right)\right] \tag{2.73}$$

Eq.2.73 demonstrates that standing wave modes f_m are localized in the $sinc^2(x)$ envelope around the LA mode with shift $q(\theta)\frac{\nu}{2\pi}$, and the $\frac{\pi d}{\nu}$ coefficient determines the width of the envelope.

The practical importance of the fine structure observation relies to the fact that computing of the elastic modulus from the Δf_m interval requires the mass density ρ and the film thickness *d* value only, which can be measured by a number of methods with adequate accuracy.

$$c_{11} = 4\rho d^2(\Delta f_m) \tag{2.74}$$

3. Mechanical Anisotropy of Polymer Films

3.1. Introduction

Non-destructive probing of elastic properties becomes a state-of-art approach in thin film research and applications, due to recent advances and growing popularity of acousto-optical methods, in particular, Brillouin light scattering [50, 51] and impulsive stimulated thermal scattering (ISTS) [52]. The ability of these methods to measure elastic constants along different directions can hardly be overestimated for anisotropic film samples, frequently found in practical applications (stretched packing films, for example). Mechanical anisotropy correlates with preferred orientation of structural units in tested material; this correlation is extensively used to analyze the effect of processing conditions on structure and mechanical stability of films [53–55]. It should be noted that the other parameter widely used for anisotropy characterization - optical birefringence - shows much less magnitude than elastic moduli ratio in some polymer films [54, 55]. However, so far the progress in non-destructive testing of elastic properties is limited mainly to free-standing films. The presence of complex acoustic modes in spectra of supported films and coatings makes the data difficult to analyze [52, 56]. In a few studies of anisotropic coatings by acousto-optical methods, ISTS is utilized and the films under investigation are substantially thicker than a micron [57, 58]. For the important class of sub-micron coatings (extensively used in microlithography), probing of elastic constants is performed on films with either known or assumed isotropy [51, 59–64] and often limited to one specific direction [51, 63, 64].

From both experimental and theoretical perspective, significant challenges exist for understanding how polymers behave when confined to dimensions near their own equilibrium length scale, where the interactions between polymer and interfaces become more pronounced. Computer simulations [16, 65] attributed anisotropy of the apparent elastic properties of nanostructures to the mechanical inhomogeinity along the confined direction. For the case of supported polymer films, this originates partially from the mismatch of the thermal expansion coefficients (CTE) between the substrate and the polymer, resulting in a stress gradient that introduces orientation variation in the thickness of the film. Based on this, the existence of a very thin polyimide layer of higher anisotropy at the substrate-polymer interface has been reported [66]. On the other hand, a more perfect ordering at the polymer-air interface has been observed [67], as a result of the spatial discontinuity near the surface.

Polyimide coatings are known to possess transverse isotropic symmetry, i.e., in and through

plane elasto-optical constants differ. Their directionally dependent properties result from commonly used fabrication techniques [68] and effects such as spinning speed, substrate material and thermal [68, 69]. Both free-standing and supported polyimide films are often used as model polymer layers [70] with strong uniaxial anisotropy of optical [66, 71–73], mechanical [57, 58, 74–76], and thermal [77, 78] characteristics. Moreover, outstanding mechanical properties, high dimensional and thermal stability, low thermal expansion, low dielectric constant of polyimide make it material of choice for protective coatings [79] and for interlayer dielectrics and passivation layers in microelectronic industry [80]. Aromatic polyimides are the most successful and widely used polymeric high performance materials for space applications [81]. High technological importance of polyimide coatings calls for adequate directionally dependent characterization tools, thus application of BLS to these objects is practically sound.

In this chapter, we show that by employing a novel scattering geometry, we can probe mechanical anisotropy in highly anisotropic films. A systematical check of the thickness-dependent elastic constants of supported polymer films over a large thickness range, from about 100 nm to 20 μm is made. Recent advances in BLS technique make possible independent probing of in-plane and out-of-plane elastic moduli of sub-micron coatings. While in-plane parameters can be determined by utilizing typical transmission scattering geometry, the reflection configuration opens the way to probe standing elastic excitations confined normal to the surface. Combination of these two approaches makes possible adequate and non-destructive characterization of mechanical anisotropy in polymer coatings of micron and sub-micron thickness range.

3.2. Experimental

3.2.1. Sample Preparation

Several types of transparent substrates were used. Type 1, $\oslash$ 25 mm microscope cover slides made by optical borosilicate glass (Fisher-brand 25CIR1D) were used for less than 500 nm thick coatings; type 2, $\oslash$ 100 mm, 0.5 mm thick fused quartz wafers where used for less than 2 μm thick coatings; type 3, $\oslash$ 51 mm, 0.2 mm thick wafers made by Schott D263 borosilicate glass were used for 10 - 20 μm thick coatings. All substrates were cleaned before use by oxygen plasma in PE-200 Oxygen Plasma Surface Treatment and Etching System (Plasma Etch) at 50 cm^3 / min oxygen flow and 250 W radio frequency power for 10 min. Then, the substrates were primed by a 0.1 $\%$ solution of DuPont VM-651 (active component is 3-aminopropyltriethoxysilane) in deionized water. The puddle of the primer stood on a substrate for 20 s. The substrate was spin dried for 60 s at 3000 rpm.

Poly (biphenyl dianhydride - p - phenylenediamine) (BPDA-PDA) polyimide films (Fig. 3.1a) were applied on the primed side of the slides and wafers by spin coating at 1000 - 3000 rpm for 60 s. Both DuPont PI-2610 polyamic acid precursor and its solutions in N-methyl-2-pirrolidone were used. Diluted precursor with concentrations ranging from 40$\%$ and above, were used for thinnest coatings (less than a micron thick). Neat precursor was used for fab-

rication of thicker coatings. Immediately after coating, the slides / wafers were soft-baked at 130 ^{o}C for 90 s on a hot plate. To obtain thick (10 - 20 μ m) films, the multiple-coating technique was used: after soft-bake, the spin-coating was repeated. The final curing was done in a vacuum oven at 350 ^{o}C for 24 h, the ramp rate was 1 ^{o}C / min.

3.2.2. Sample Characterization

Accurate determination of the coating thicknesses is of the key importance for this study. The film thicknesses were obtained by scanning confocal microscope (Nanofocus AG μSurf) equipped with a Nipkow disk which directly measure the depth of a scratch on the films made by a sharp needle tip (Fig. 3.1b). The mean thicknesses were computed by averaging over the whole sampled area. Additionally, the thickness of polyimide layers was verified by two methods. In the first method, the thickness was measured by reflectometry on silicon wafers coated at the same conditions as the glass slides. Filmetrics F20 reflectometer (spectral range 450-900 nm) was used and thicknesses were measured at 3 points for each sample. The second method was weighting of coated wafer on a sensitive balance (Mettler-Toledo XS105 DualRange, 0.01 mg resolution), and computing the thickness by obvious geometric considerations. Density of the polyimide film is 1.40 g / cm^3 [82]. Reflectometry measurements require external parameter - refractive index spectrum for the used range of wavelengths; coating of silicon surface can yield slightly different coating thickness. Weighting results can be biased by the non-uniformity of film thickness, especially on the wafer edges; the accuracy of the measurement rapidly decreases with film thickness. Due to these reasons, the thicknesses measured by the confocal microscope are considered as primary values, while results of reflectometry and weighting are used as controls.

3.2.3. Scattering Geometries

The direction dependence of the elastic moduli is investigated by two scattering geometries [62]. In-plane mechanical properties are probed using the transmission geometry, while the reflection geometry provides access to out-of-plane characteristics. In the transmission arrangement, the wavevector **q** is parallel to the film surface: $q = q_{\parallel}$, where $\parallel$ index denotes the in-plane - oriented component. In the reflection geometry the wavevector q is normal to the film surface: $q = q_{\perp}$, where $\perp$ index denotes the out-of-plane component. Probing elastic excitations with parallel and perpendicular to the film surface wavevector **q** yields information about in-plane and out-of-plane elastic properties, respectively. Both longitudinal and shear moduli can be accessed separately by the light polarization control. In the present study, the polarization of incident laser beam is always perpendicular **(V)** to the scattering plane. Polarization of the scattered light can be selected either perpendicular **(V)** or parallel **(H)** to the scattering plane. Polarized **(VV)** and depolarized **(VH)** Brillouin spectra correspond to light scattering by longitudinal and transverse phonons, respectively. Probing longitudinal and transverse polarizations gives access to longitudinal and shear elastic moduli, respectively.

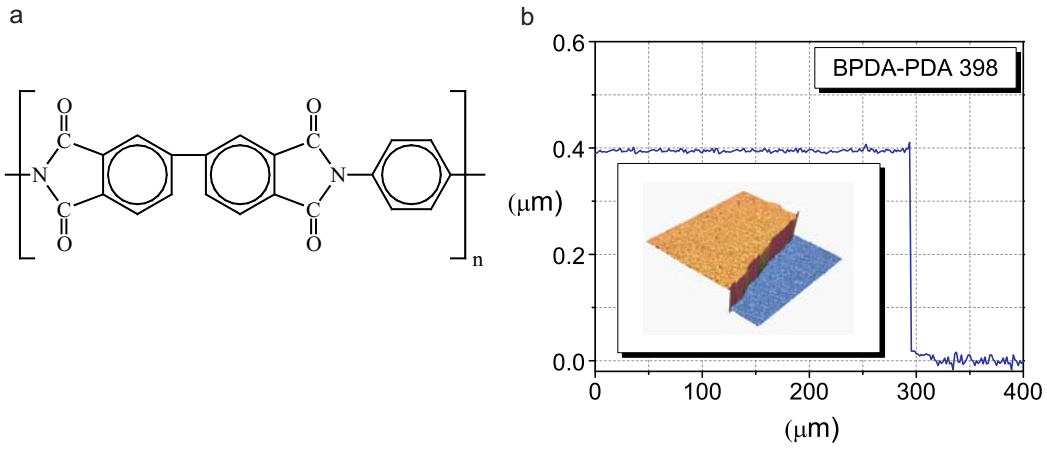

Figure 3.1.: **a,** Chemical structure of BPDA-PDA polyimide. **b,** Scanning confocal microscope (Nanofocus AG μSurf) image showing thickness measurement for 398 nm thick polyimide film. The inset demonstrates the 3D color representation of the step profile.

3.3. Results and discussion

For the most part of this chapter, we will discuss elastic properties in terms of phase sound velocities ν. Lower indices **l** and **t** denote longitudinal and transverse polarizations, respectively. Upper indices $\parallel$ and $\perp$ denote in-plane and out-of-plane directed excitations, respectively.

In order to investigate the potentially size-dependent behavior of the elastic constants, especially close to the limit of molecular level size scales, we characterized films with thicknesses ranging from 20 μm to 97nm. The propagation character of elastic excitations strongly depend on the film's thicknesses. When its size becomes comparable to the acoustic wavelength $\lambda_A = 2\pi$ / q, the dispersion relations for propagation both parallel and normal to the film surface deviate from the simple acoustic-like behavior [47, 83]. Thus, characteristic thickness h_1 for this size effect is determined by the minimal **q** used in our experiments, 0.006 nm^{-1}. It corresponds to $h_1 = 2\pi$ / (0.006 nm^{-1}) = 1 μm.

3.3.1. Acoustic Regime

BLS spectra for h = 10 - 20 μm thick coatings (h $\gg h_1$) are expected to demonstrate simple acoustic behavior: Brillouin shift *f* of a well-shaped mode is proportional to wavevector *q* and does not depend on film thickness. This trivial behavior is demonstrated in Fig. 3.2 for 20 μm thick BPDA-PDA coating for all 4 combinations of geometry and polarization. Mechanical anisotropy is clearly seen as difference in slope (proportional to phase velocity) of linear *f(q)* functions obtained for orthogonal directions both for longitudinal and shear excitations. Table 3.1 presents sound velocities calculated from the slopes of the —Fig. 3.2 plots; the error

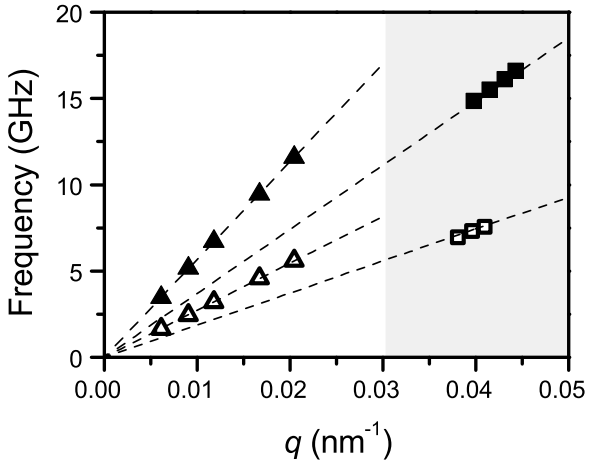

Figure 3.2.: Mechanical anisotropy in a thick (20μm) polyimide (PI) film. Acoustic phonons propagating with longitudinal (solid symbols) and transverse (open symbols) polarization parallel (triangles) and normal (squares) to the film surface. The two scattering configurations relative to the Fabry-Perot interferometer enabling selection of the phonon wave vector q parallel ($\|$) and normal ($\perp$) to the film surface are shown in the white (transmission) and gray background(reflection geometry) respectively

defined as standard deviation of the data does not exceed 1.5 $\%$. Our results are in accordance with previous study of elastic properties of BPDA-PDA at hypersonic frequencies performed by ISTS technique on free-standing films [74].

Wave	In- plane	Out- of- plane
Longitudinal	$\nu_l^{\|}$ = 3560 m/s c_{11} = 17.7 GPa	$\nu_l^{\perp}$ = 2340 m/s c_{33} = 7.67 GPa
Shear	$\nu_t^{\|}$ = 1710 m/s c_{66} = 4.09 GPa	$\nu_t^{\|}$ = 1140 m/s c_{44} = 1.82 GPa

Table 3.1.: Sound velocities and components of the stifness tensor for 20 μm thick BPDA-PDA coating.

3.3.2. Out of Plane Elastic Excitations

Having characteristics of thick BPDA-PDA coatings as a starting point, we can address potential thickness-dependent elastic behavior by probing thinner films, where size effects on the wave propagation are significant. Fine structure of the out-of-plane longitudinal acoustic

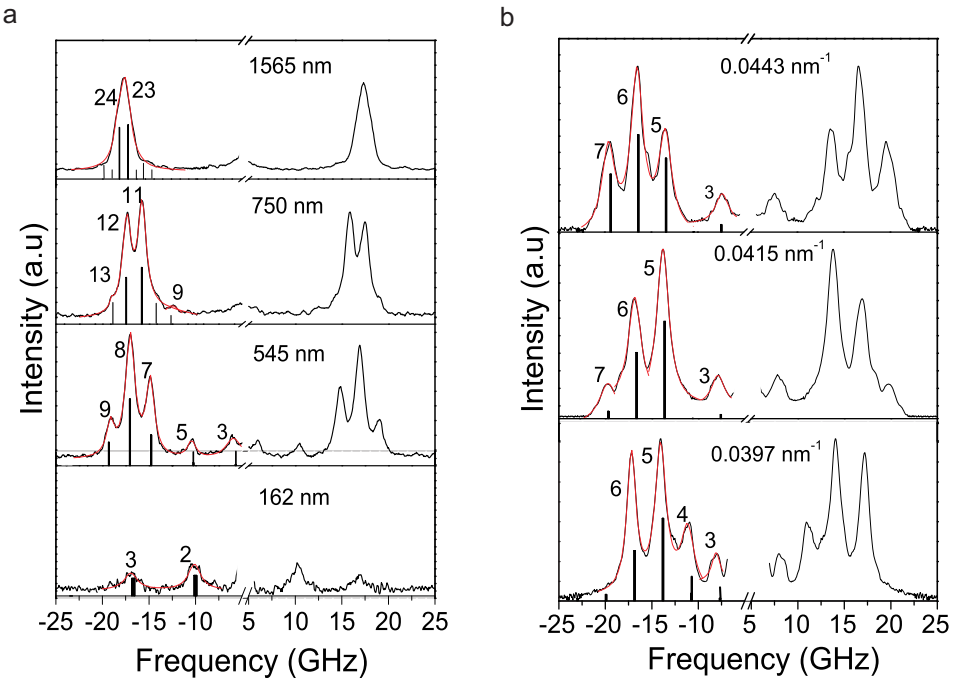

Figure 3.3.: Thickness dependence of the out-of-plane longitudinal elastic excitations. BLS spectra are shown for the BPDA-PDA coatings with four different thicknesses ranging from 162 nm to 1565 nm (Fig. 3.3a) at a scattering angle θ = 150^o ($q_\perp$ = 0.0443 nm^{-1}) and for the film with h = 380 nm at θ = 150^o, 90^o and 60^o (Fig. 3.3b). The corresponding $q_\perp$ values indicated in the plot. The spectra are well represented (red solid lines in the Stokes side) by up to five lorentzian lines. The integers denote the vibration order ***m*** and the vertical lines represent the computed amplitudes of the observed modes [62].

mode detected in sub-micron coatings offers an excellent opportunity to trace size dependence of the corresponding elastic modulus. As shown in Fig. 3.3 (left panel), the BLS spectra of less than 2 μm films obtained for reflection geometry and longitudinal polarization develop a fine structure due to the presence of standing acoustic excitations normal to the film. The experimental line shape is represented by the sum of up to five lorentzian lines centered at frequencies $f_m = (2m+1)\nu_l^\perp/4h$, where m is an integer [62]. The standing wave nature of these excitations is further verified by varying ***q*** while film thickness is fixed. In this test the localized modes have the same Brillouin shift regardless of ***q***, while longitudinal phonon mode envelope shifts up in frequency as ***q*** increases. It is demonstrated in the right panel of Fig.3.3).

The frequency interval Δf between adjacent resonance modes is a function of phase velocity and film thickness only: $\Delta f = \nu_l^\perp/2h$, and can be used to compute the out-of-plane longitudinal sound velocity independently. Fig. 3.4 summarizes $\nu_l^\perp$ obtained both from fine structure spacing (less than 2 μm thick films) and from Brillouin shift of the propagation phonon mode (10 - 20 μm thick coatings). The $\nu_l^\perp$ data demonstrate no size dependence in studied thickness

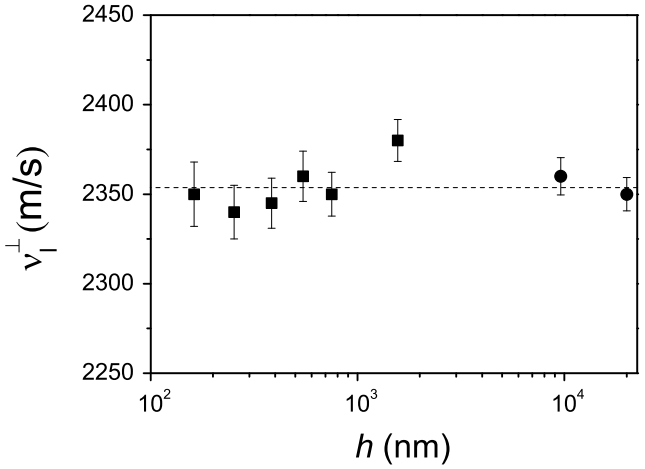

Figure 3.4.: Dependence of out-of-plane longitudinal phase velocity $\nu_l^{\perp}$ on thickness measured by two methods: using Brillouin shift of the propagating acoustic mode (circles, 10 -20 μm films) and using fine structure spacing (squares, less than 2 μm thick films).

interval 0.16 μm - 20 μm. Excellent agreement (within 1.5% experimental error) between μm values obtained by two methods confirm the sufficient accuracy of two used parameters: film thickness measured by confocal microscopy and ordinary index of refraction found from literature.

The fine structure is found for longitudinal acoustic mode only. The reason why depolarized BLS spectra exhibit no standing wave effect can be attributed to the fact that the scattering by shear waves is significantly less intense than the signal from longitudinal phonons. The low signal-to-noise ratio may prevent observing the transverse mode splitting.

3.3.3. In Plane Phonon propagation

Another way to check the independence of elastic properties on thickness is the analysis of dispersion relations as demonstrated for polyimide free-standing films studied by ISTS technique [57]. Six BPDA-PDA coatings with thickness in the 0.1 - 0.75 μm range (less than h_1 characteristic size) are examined in the transmission geometry and observed modes are combined into dispersion diagram shown in Fig. 3.5 These film-guided modes are dispersive, that is, a simple linear **q** dependence of the phonon frequency $f = \nu$ q / 2π is not satisfied, where ν is the phase velocity of the phonon. In the case of thin films, it is usually customary to demonstrate the dispersion relation in terms of phase velocity ν versus qh, the product of the phonon wave number and the film thickness. This is because for a given material combination, the phonon phase velocity is only a function of qh, as pointed out already in Chapter 2. From the measured dispersion relations (symbols) it is evident that at the same qh value, data points

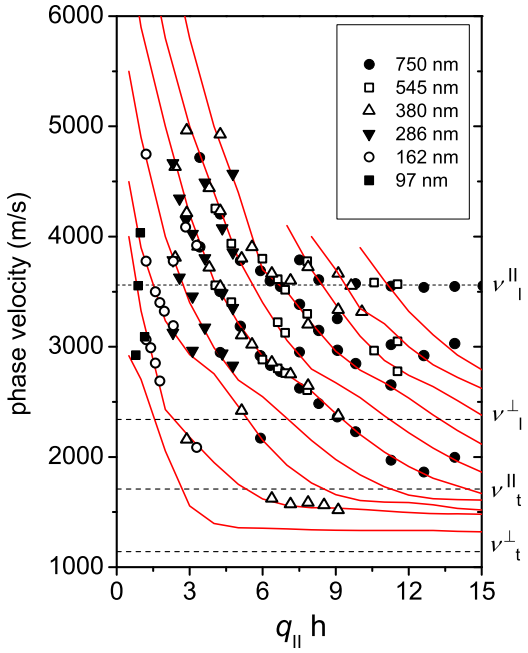

Figure 3.5.: Dispersion diagram of the in-plane elastic excitations in supported BPDA-PDA films. The plot contains data for six different thicknesses in the 0.1 - 0.75 μm range and for q in the 0.006 - 0.022 nm^{-1} range. Correspondence between the symbols and the thickness of coating is given in the inset legend. Red solid lines represent theoretical model with all model parameters predetermined.

measured from different films show very good overlap in the ν vs q*h* plot, suggesting the same or very close elastic properties of these thin films. To theoretically identify the nature of the observed modes and extract the elastic constants, we employ the layer-multiple-scattering method.

This method constitutes a powerful tool for an accurate evaluation of the elastic properties of composite systems consisting of a number of different layers having the same two-dimensional periodicity in the x-y plane (parallel to the layers)[56]. An advantage of the method is that it does not require periodicity in the z direction (perpendicular to the layers). For each layer, the method calculates the transmission and reflection matrices, Q^I and Q^{III} respectively, for a plane wave incident on the layer with given frequency and $k_{||}$ from z$\rightarrow -\infty$ (i.e. with $k_z > 0$), as well as the corresponding matrices Q^{IV} and Q^{II} for incidence from z$\rightarrow \infty$ (i.e. with $k_z < 0$). The transmission and reflection matrices of the composite system are calculated from those of the constituent layers. In the specific case considered here, we deal with the simple situation where a planar interface between two different homogeneous media is considered. The

transmittance, reflectance, and absorbance of a (composite) slab, as well as the corresponding density of states of the elastic field, are obtained from the transmission and reflection matrices of the slab . The eigenfrequencies of possible guided modes are evaluated from the condition to have a wave field localized within the slab. Dividing the slab into a left and a right part, this condition leads to the secular equation: det[I-$Q^{II}_{(left)}Q^{III}_{(right)}$] = 0.

All model parameters used for the theoretical calculation of the dispersion relation are predetermined: $\nu_l^{\parallel}$, $\nu_t^{\parallel}$, $\nu_l^{\perp}$, and $\nu_t^{\perp}$ values for BPDA-PDA coatings are taken from the thick film BLS measurements (Table 1), BPDA-PDA mass density, 1.40 g / cm^3, is given in [82], ν_l, ν_t,and mass density of the substrate are determined beforehand. The theoretical dispersion curves for the observed modes are indicated by the solid lines in Fig. 3.5. As we can see, very good agreement between theory and experiment is obtained without using any adjustable parameter. This tight correspondence of the experimental data and the model for the whole thickness range implies that elastic moduli (and mass density) determined for 10-20 μm thick films are valid down to 0.1 μm film thickness - no size effect is observed.

3.4. Conclusions

While ISTS method has been used for similar studies of 2 - 10 μm thick films, this work extends explored thickness range up to the 0.1 - 20 μm. Both longitudinal and shear moduli for both in-plane and out-of-plane directions are reported. The lower value of sound velocities (and the corresponding moduli) in the direction normal to the film is assessed by the distribution of intramolecular and intermolecular forces in the film. The elastic behavior of the supported films is shown to be size-independent in the whole thickness range investigated. This finding clearly shows that the thinning process has no effective impact on the elastic constants. The apparent insensitivity to thickness variations suggest that the morphology (molecular order, microstructure) is primarily tuned during the fabrication process.

4. One Dimensional Phononic Structures

4.1. Multilayer Polymer Films

4.1.1. Introduction

Layer-multiplying coextrusion [84–86] of incompatible polymers can lead to nanostructured multilayer composite films with superior characteristics, such as improved barrier, thermal and mechanical behavior, which are important to many industry applications including coating and packaging. These multilayer films represent a well-defined 1D periodic structure that consists of hundreds to thousands of thin layers of the two component polymers stacked in a strictly alternating fashion. It has also been shown that by properly designing the periodicity and selectively introducing optical anisotropy to these nanolayers, the resulting film can display extraordinary optical effects [86], e.g. broadband omnidirectional reflection, implying widespread potential applications in optics. The significant practical relevance of such multilayer films demands an advanced control over the film quality which is however highly influenced by the complex structural relaxation characteristic to polymers. For small layer thickness, in addition to the detailed processing conditions the chain dynamics is further complicated by other factors including finite-size and interface effects [87, 88]. As the mechanical properties of a glassy polymer are susceptible to structural relaxation difference during processing, there is a strong desire to probe the mechanical properties of these multilayer films down to the single-layer level.

The periodic structure of these films deserves special attention as studies on photonic [19] and phononic crystals [89] have revealed the potential of periodically structured composite materials in manipulating classical waves. One of the pivotal concerns for the current system is the phonon dispersion behavior. As phonons in dielectric materials play a decisive role for heat transport, a good knowledge of phonon propagation in such structured materials is the precondition to finally realize heat management by structure engineering [90]. The multilayered structure with periodicity commensurate the wavelength of the visible light may allow the occurrence of confinement-induced enhancement of photon-phonon interactions [91, 92], an effect sensitive to phonon dispersion as well. Moreover, phonon dispersion behavior is essentially determined by the elastic parameters and the structure of the system. Therefore it provides valuable details on the structure modulation of phonons and the mechanical properties of the individual layers. The latter suggests that the desired quality control of the multilayer films

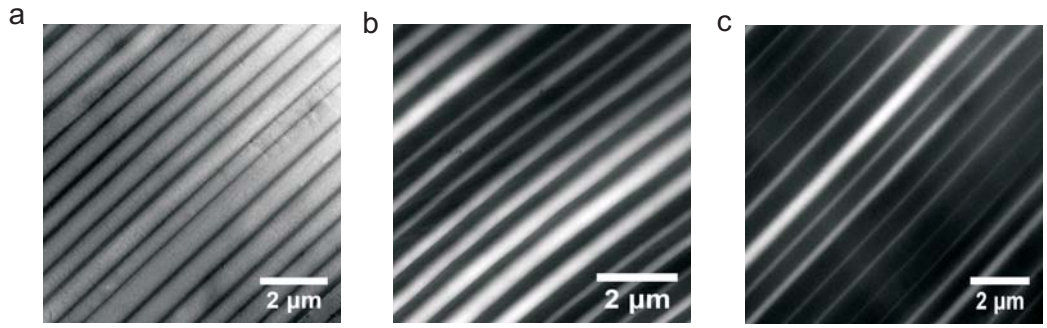

Figure 4.1.: TEM images of the cross section of the PMMA-PC multilayer films with PC composition: a, 20% b, 50% and c, 80%. PMMA and PC layer thickness is 380 nm respectively.

can be achieved by monitoring the phonon propagation in the film. Knowledge on phonon attenuation could further provide information such as structural relaxation and material defects [93]. In spite of the great importance of phonon dispersion in such polymeric nanostructured films with 1D periodicity, the only experimental study so far was performed recently on a film comprised of alternating poly(methylmethacrylate) (PMMA) and poly(ethylene terephthalate) (PET) nanolayers using Brillouin light scattering [94] that probes phonon dispersion via inelastic scattering of light by phonons. Although this preliminary attempt clearly revealed the layer confinement of phonon propagation as well as the impressive mechanical anisotropy, the single film used with strong optical anisotropy excluded a deep insight into such a system.

4.1.2. Film characterization

The PC / PMMA multilayer films of total thickness about 50 μm with different periodicity and composition were fabricated by varying the layer-multiplying number and the volume fractions ϕ of the pure components [84, 85]. For TEM examination, thin sections of about 60 nm were prepared using a Leica EMUC6 ultra-microtome employing a diamond knife at room temperature. TEM experiments were carried out on a JEOL 2010F equipped with a post-column Gatan Imaging Filter (GIF). The zero loss energy filtered images were taken with an energy window of 15 eV.

4.1.3. Dispersion relation for in-plane phonon propagation

For in plane phonon propagation, BLS was used in the transmission geometry. In this case, the scattering wavevector **q** is parallel to the layers and independent of the refractive indices of the layers. Figure 4.2a shows polarized (VV) Brillouin spectra at $q_{\parallel}$ = 0.0152 nm^{-1} and ambient conditions for six PC / PMMA films with symmetric composition (ϕ = 0.5) but different layer

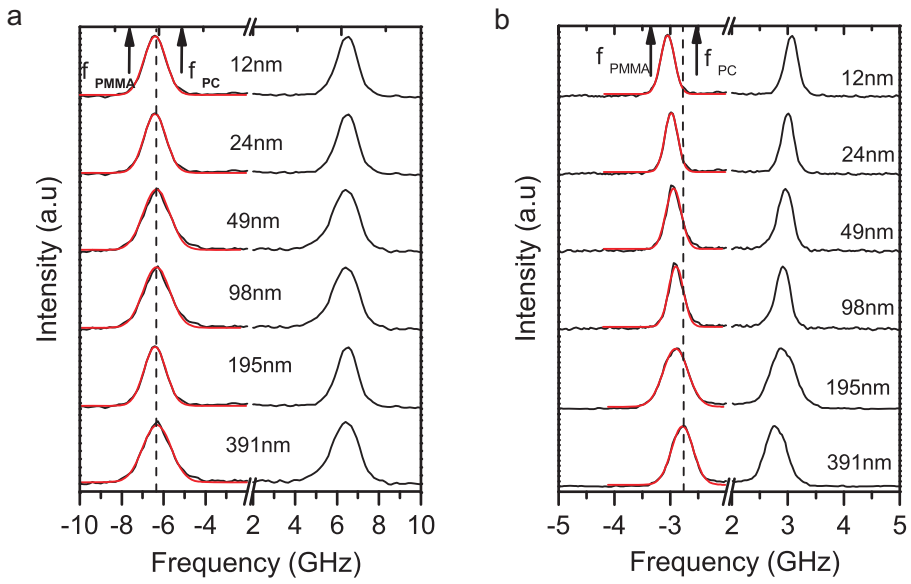

Figure 4.2.: **a,**Isotropic (VV) BLS spectra at $q_{\|}$ = 0.0152 nm^{-1} and 20 ^{o}C for six periodic PC / PMMA multilayer films with symmetric composition but different layer thickness as stated in the plot. The two arrows on the top of the figure denote the frequency of the longitudinal phonon at 0.0152 nm^{-1} in the pure PC (f_{PC}) and PMMA (f_{PMMA}) multilayer films.**b,** Anisotropic (VH) BLS spectra at $q_{\|}$ = 0.0152 nm^{-1} and 20 ^{o}C six periodic PC / PMMA multilayer films with symmetric composition but different layer thickness as stated in the plot. The two arrows denote the frequency of the shear phonon at 0.0152 nm^{-1} in the pure PC and PMMA multilayer films.

thickness between 12 nm and 390 nm.

All spectra show a prominent Brillouin doublet surprisingly at the same frequency in the BLS spectra of Fig.4.2a. The peak frequency f = 6.35 GHz at $q_{\|}$ = 0.0152 nm^{-1} leads to the phase velocity ($c_l = 2\pi f / q_{\|}$) 2625 $\pm$30 m/s for the phonon with longitudinal polarization. This value falls between the longitudinal sound velocities of the two materials ($c_{lPMMA} = 2850\pm$ 40 m/s and $c_{lPc} = 2430\pm$ 30 m/s) measured in pure PMMA and PC films coextruded under the same condition. Assuming a homogeneous ($hq_{II} \ll 1$) two-component medium, application of Wood's law [1] to estimate the sound velocity in a PC / PMMA composite with PC volume fraction ϕ = 0.5 yields c_{eff} = 2615 m/s, in excellent agreement with the experimental value of c_l. The appearance of this distinct longitudinal phonon propagating with the same velocity in

[1] $1/\rho c^2 = \phi/\rho_{PC}c_{PC}^2 + (1-\phi)/\rho_{PMMA}c_{PMMA}^2$, with $c_{PC} = (2430 \pm 30)m/s$ and $c_{PMMA} = (2850 \pm 40)m/s$ assuming the same densities $\rho = \rho_{PMMA} = \rho_{PC}$

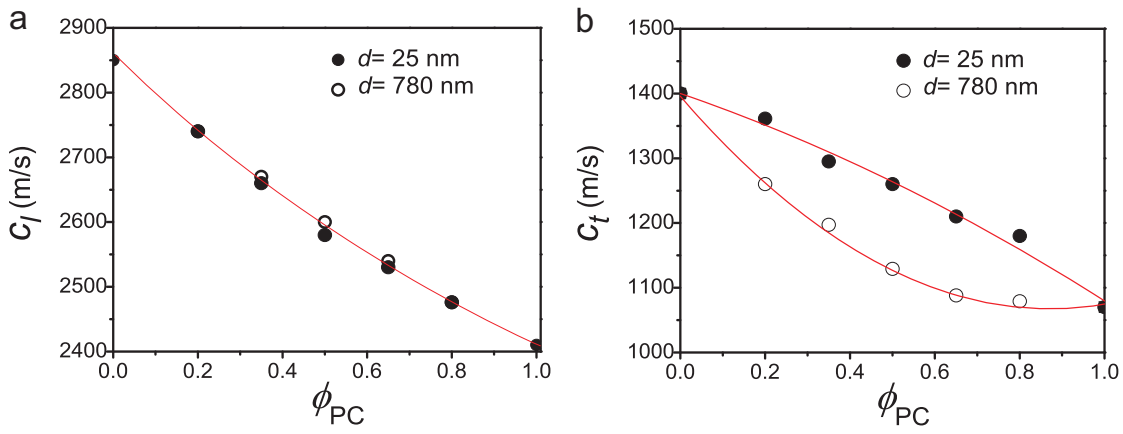

Figure 4.3.: **a,**The longitudinal sound velocity c_l is plotted as a function of PC composition in the PC / PMMA multilayer films with bilayer spacing *d* = 25 nm (solid symbols) and *d* = 780 nm (open symbols). The solid line denotes the representation by Wood's relation14.**b,** The shear sound velocity is plotted as a function of PC composition in the PC / PMMA multilayer films with bilayer spacing *d* = 25 nm (solid symbols) and *d* = 780 nm (open symbols).

all six films indicates effective-medium behavior for all these films, which is rather unexpected for the three films with large layer thickness with $hq_{\|} \gg 1$. For the latter, a closer inspection of the spectra in Fig.4.4 indeed reveals additional spectral features, e.g. a broader lineshape of the main peak . A homogeneous-medium-like behavior is also observed for the PC / PMMA multilayer films at constant periodicity *d* but different compositions.

Figure 4.3a displays the effective-medium longitudinal phonon velocity for five different PC volume fraction ϕ with two extreme periodicities, *d* = 25 nm and *d* = 780 nm. The solid line is the prediction of the Wood's law with no adjustable parameters. The data suggest that the confinement of PC and PMMA layers at nanoscale does not affect the longitudinal modulus, M = ρc_l^2, of the multilayer films assuming a constant density ρ.

Figure 4.2b displays the depolarized (VH) spectra at $q_{\|} = 0.0152\ nm^{-1}$ for the same six films of Fig.4.2a . Since the intensity of the VH spectrum is proportional to the segmental optical polarizability anisotropy [95], the VH spectrum of the pure PMMA "multilayer" film is hardly measurable. The glassy films support shear and hence the single Brillouin doublet in the VH spectrum is assigned to the phonon with transverse polarization. For the pure PC glassy film, the transverse sound velocity c_{tPC} amounts to 1070 m/s whereas for PMMA, c_{tPMMA} = 1400 m/s was obtained from the VH spectrum of a bulk PMMA sample. In clear contrast to the VV spectra of Fig.4.2a, the peak position for the symmetric PC / PMMA multilayers is no longer constant but shifts to higher frequencies with decreasing layer thickness. By monitoring the q - dependence of the spectrum, this transverse phonon is found to show a linear dispersion

(see Fig.4.5 below) for all six films like the longitudinal phonon in Fig.4.2a. Therefore all films exhibit effective-medium behaviour for the transverse phonon propagation. However, the transverse sound velocity shows a monotonic increase from 1130 m/s for the largest layer thickness (*h* = 390 nm) to 1270 m/s for the thinnest layer (*h* = 12 nm).

To further verify this finding, we also measured the VH spectra for the films with two extreme periodicities and different compositions. The same effective-medium and linearly-dispersed transverse phonons are found in all the films and the increased shear modulus with decreasing layer thickness is confirmed as well for asymmetric compositions, as shown in Fig. 4.3b. Thus it is clearly revealed that the confinement effect has an evident impact on the shear modulus of these films despite its negligible influence on the longitudinal modulus, possibly due to the confinement-induced stronger shearing force on polymer chains during processing . This impacts the chain conformation more than the packing density. An analog to the Wood's relation is however not known for shear modulus and the red lines in Fig. 4.3b represent a polynomial least-square fit to the experimental c_t data varying between c_{tPMMA} and c_{tPC} of the pure PMMA and PC, as expected for an effective-medium behavior. The shear modulus, G = ρc_t^2, increases by about 60 $\%$ in the bilayers with *h* = 5nm compared to the bilayers with *h* = 624 nm film with G = 1.5 GPa (ρ = 1.2 g / cm^3).

In addition to the impressive effective-medium behavior, the recorded BLS spectra also carry important information on the structure influence on phonon propagation. For a better visualization of the spectral features ,we plotted the VV spectra in logarithmic intensity scale as shown in Fig.4.4 for the two symmetric-composition films with periodicity *d* = 780 nm and *d* = 100 nm, respectively. For the former with larger layer thickness *h*, the rich features are clearly visualized and up to five modes **(2-6)** are clearly resolved. For the second film with *d* = 100 nm (*h* = 50nm) (lower panel), the single longitudinal **(5)** and transverse **(1)** modes display a complete homogeneous-medium behavior. The barely distinguishable VV spectra for films with low *h* ($hq_{\|} < 1$) and their rich features at high *h* ($hq_{\|} > 1$) are in agreement with the anticipated interaction between wave and structure.

The detailed knowledge of the in-plane phonon propagation including the identification of the spectral features in Fig.4.5 needs the phonon dispersion relation which is a plot of the BLS peak frequency versus $q_{\|}$, as shown in Figure 4.5 for the symmetric-composition film with layer thickness 390 nm. The previously encountered effective-medium longitudinal **(5)** and transverse **(1)** phonons are readily identified by their linear dispersion that yields the longitudinal and transverse phase velocities c_l and c_t respectively. The origin of modes **(2-4)** and **(6)** cannot be identified without computation of the theoretical dispersion relations. However, the experimental dispersion of these modes in Fig.4.5 bears resemblance to layer guided modes [96, 97] suggesting a relation to the multilayer structure. The apparent phase velocities $c_{\|} = 2\pi f/ q_{\|}$ of these "structural" modes fall close to c_t for **(2, 3)** and to c_l for **(6)**.

4.1.4. Finite element analysis (FEA) modeling

Finite element analysis was used to compute phononic dispersion relations and provide interpretation of the observed propagation modes [98]. This model assumes perfectly bonded,

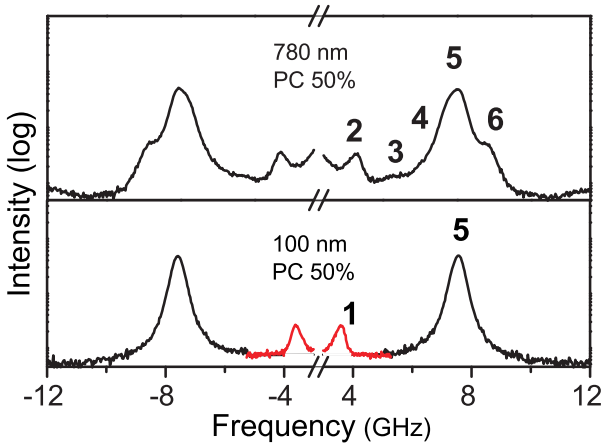

Figure 4.4.: BLS spectra at q_{II} = 0.0181 nm^{-1} and 20 ^{o}C for two periodic symmetric multilayer films with bilayer thickness *d* = 100 nm and 780 nm. The numbers indicate modes with increasing frequency.

ideally flat layers with uniform thickness, no roughness and defects, no spatial variations in elastic properties within a given layer and zero interface thickness. The following densities and elastic constants were used in the model: ρ_{PMMA} = 1190 kg / m^3, E_{PMMA} = 6.26 GPa, σ_{PMMA} = 0.341; ρ_{PC} = 1300 kg / m^3, E_{PC} = 4.11 GPa, σ_{PC} = 0.38. These values of elastic constants are based on independent measurements of c_l and c_t in homogeneous PMMA and PC films. Figure 4.5 shows the comparison of the theoretical dispersion relation and the experimental results for the symmetric-composition film with periodicity *d* = 780 nm, and a good agreement between theory and experiment is found. The predicted quasilongitudinal (QL), quasitransverse (QT) and mixed modes (modes with displacements fields primarily parallel, perpendicular or without preferential orientation to the wave vector, respectively) are shown as solid, dashed and dotted lines, respectfully. Note that scattering from mixed modes is generally very weak and difficult to detect experimentally [98]. In fact, there is an overall good agreement between the experimental and modeling results for all the film compositions and periodicities with no adjustable parameters. The appearance of additional modes **(2-4)** and **(6)** is predicted by theory. Importantly, FEA allows computing the details of the displacement fields, thereby allowing deeper insight into the nature of these modes.

Displacement fields corresponding to QT and QL modes for $q_{||}$ = 0.025 nm^{-1} in the symmetric film with *d* = 780 nm are shown in Figure.4.6, ordered from low to high frequency. There are three distinct QT and three QL modes predicted for this sample, although only two QT modes are resolved experimentally, probably due to close proximity of the QT modes and / or structural imperfections of the layers. Note that, while the various QL and QT modes propagate with essentially the same respective phase velocities (Fig.4.5), the displacements are localized primarily within the individual PC or PMMA layers (Fig.4.6). When the phonon wave vector $q_{||}$ approaches zero, the modes **(2, 3 and 6)** present localized, non propagating eigenvibrations of the periodic bilayers with zero group velocities and frequencies given by *f*

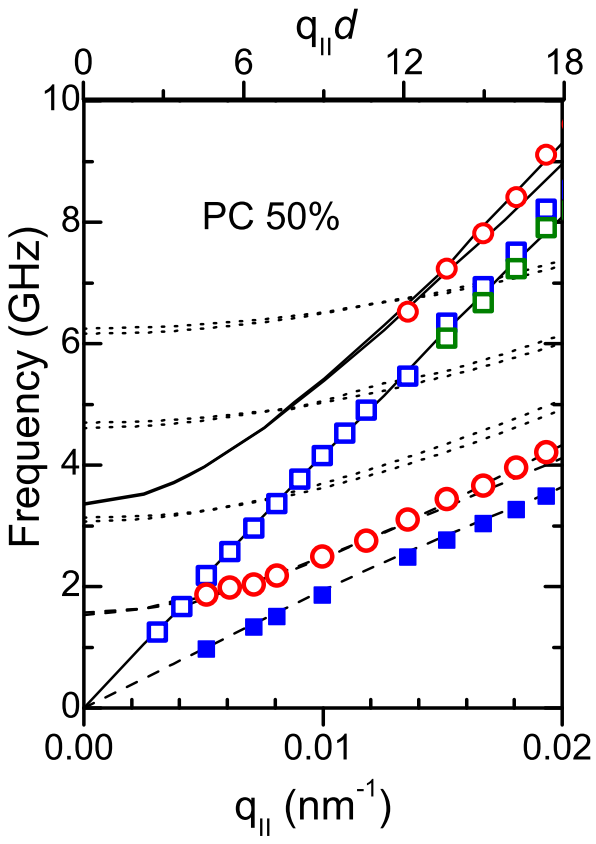

Figure 4.5.: The dispersion relations for a symmetric film having a bilayer thickness d = 780 nm. The lines indicate the theoretical dispersions for the modes with quasi longitudinal (QL) (solid) quasi transverse (QT) (dashed) and mixed (dotted) polarizations. Open and solid symbols refer to the isotropic (VV) and anisotropic (VH) BLS respectively.

= m c_i / d , where m = 1, 2,..., and c_i is either the longitudinal c_l , for **(6)**, or transverse c_t, for **(2, 3)**. For the larger values of $q_{||}$, the displacement fields of these modes evolve into layer guided phonons (Fig.4.6) propagating with group velocities that approach the phase velocities of the medium as seen in the dispersion relations in Fig.4.5.

4.1.5. Temperature dependence of the elastic constants

The biased spatial distribution of the displacement fields for different modes is manifested in their softening temperatures T_s. The phase velocity c(T) of these modes is anticipated to display the characteristic kink at the temperature that corresponds to the T_s of their propagation medium. Thus, the phase velocity c(T) of various phonon modes can be used in combination with the theoretical modeling to provide interpretation on the nature of the observed propaga-

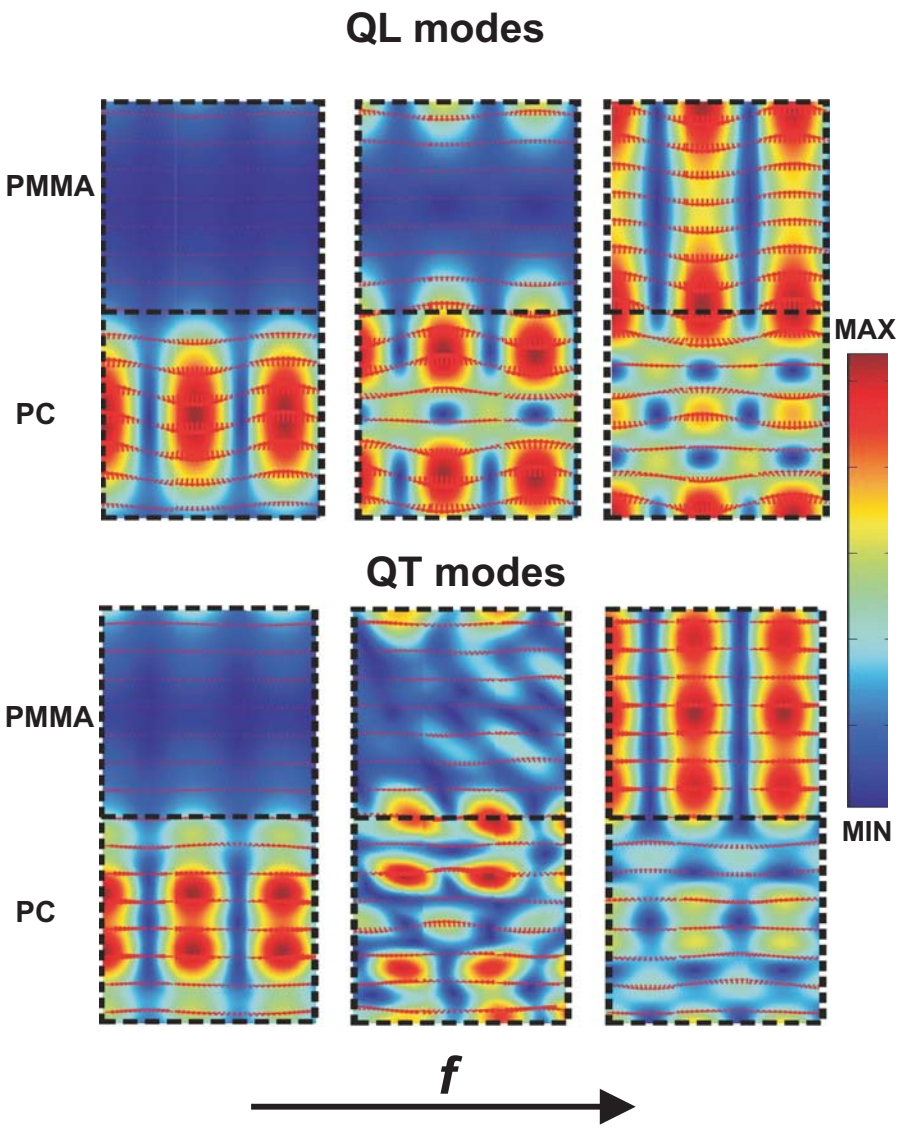

Figure 4.6.: Details of the displacement fields for the quasi-transverse and quasi-longitudinal modes computed for the symmetric 780 nm bilayer film at $q_{II} = 0.025nm^{-1}$

tion modes. Figure 4.7 shows the c(T) for the symmetric bilayer films with periodicity **(a)** *d* = 780 nm and **(b)** *d* = 25 nm. The sample with *d* = 25 nm displays a single T_s of 122 ^{o}C which is intermediate between the T_g of the PMMA (105 ^{o}C) and PC (140 ^{o}C) layers. Thus, phonons propagating in this film do not resolve the presence of individual layers and display a homogeneous medium-like behavior, further supporting the previous conclusion. In contrast, there are three distinct T_s for phonons propagating in the film with *d* = 780 nm. Modes **(1)** and **(4)** have T_s of 135 ^{o}C which is similar to T_g of PC; mode **(6)** has of T_s 105 ^{o}C , which is essentially the T_g of PMMA; while T_s of mode **(5)** is 122 ^{o}C. Therefore, modes **(1)** and **(4)** must propagate

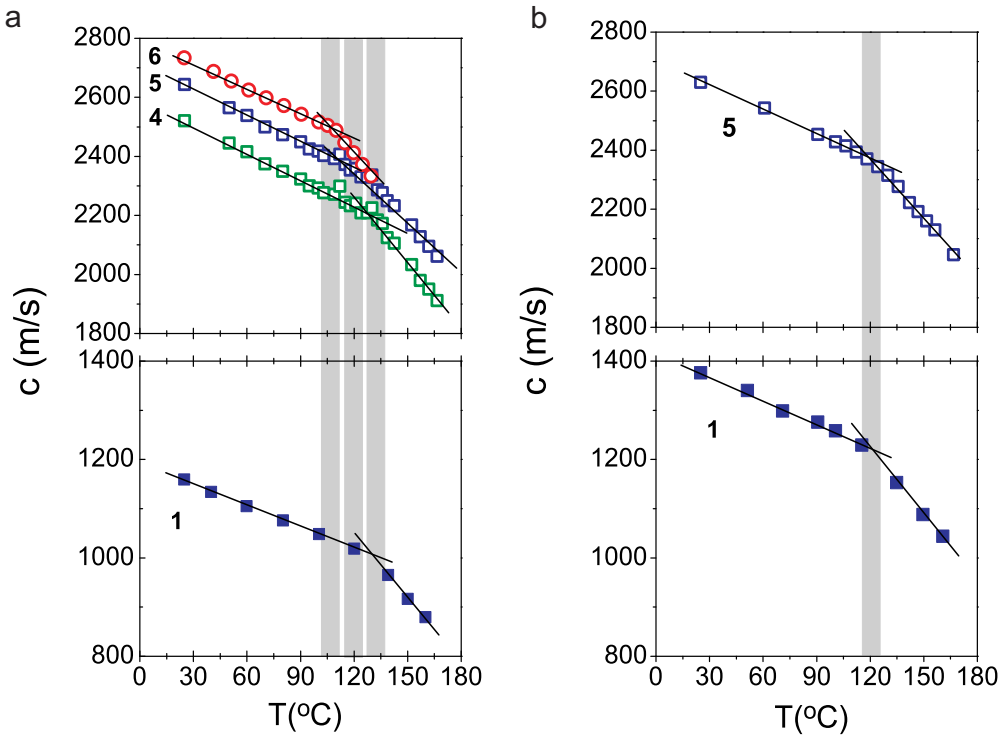

Figure 4.7.: The softening transition temperatures (vertical shaded regions) for the modes **(1,4-6)** of the experimental BLS spectrum of Fig.4.4. Solid lines represent linear fits of the experimental velocities before and after the transition.

primarily in the PC layers; mode **(6)** - primarily in the PMMA layers; and mode **(5)**-in both PC and PMMA layers. This conclusion agrees reasonably well with the theoretical displacement fields shown in Fig.4.6, which suggest that the lowest frequency QT and QL modes should propagate in the PC and PMMA layers, while the mid frequency longitudinal mode **(5)** is not strongly localized.

4.1.6. Out of plane elastic excitations

As a brief digression of the in-plane phonon propagation under discussion, Fig.4.8 shows a VV BLS spectrum for phonon propagation normal to the layers recorded at $q_{\perp} = 0.035\ nm^{-1}$. There are two peaks present: peak **(5)** at roughly 15 GHz corresponding to the effective-medium longitudinal phonon and a "Bragg" peak[96] **(B)** at roughly 12 GHz due to the periodicity modified momentum conservation condition in the scattering process. The phase velocity of the effective-medium phonon is found to be the same as that for in-plane propagation, indicating the mechanical isotropy of the present system at the long wavelength limit. This q value

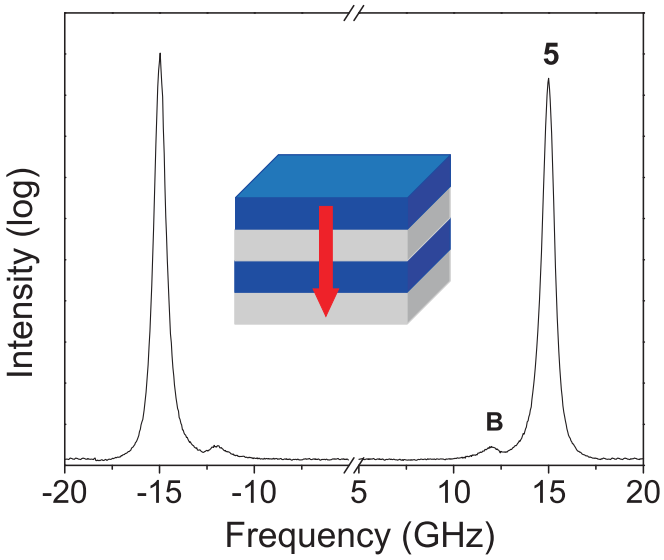

Figure 4.8.: Brillouin spectrum for out-of-plane phonon propagation at $q_{\perp} = 0.035\ nm^{-1}$. The scattering geometry is indicated in the inset. The peak at about 15 GHz corresponds to the longitudinal phonon propagating along the surface normal. The weak feature at about 12 GHz is the Bragg peak due to the periodicity.

corresponds to a phonon with a wavelength of about 180 nm, which should be short enough to distinguish the mechanically different two layers. However, the single phonon spectrum of Fig.4.8 displaying a longitudinal wave propagating with a phase velocity in an effective medium appears to contradict the layered structure of the film. This apparent contradiction with the in-plane phonon propagation , where the two layers do exhibit distinct in-plane sound velocities, is attributed to the sufficiently low elastic contrast between the two layers in the direction of the film normal.

For the out-of-plane phonon propagation, we are actually dealing with a 1D phononic crystal. The phononic band structure of this 1D phononic crystal can be calculated by FEA with the use of the same sets of elastic constants for PMMA and PC, which however reveals negligible small Bragg gaps at the first Brillouin zone boundary. To a good approximation, the phonon propagation along the film normal is isotropic, in accordance with the single experimental phonon spectrum (Fig.4.8). The experimental and theoretical phase velocities of this single phonon are 2625 m/s and 2640 m/s, respectively. The frequency of **(Bragg)** is related to the lattice constant, therefore can be used to estimate *d* and to also check the possible variation of the layer periodicity over the sample within different probed volumes. We found that *d* fluctuates about 20% around the nominal 780 nm thickness[84, 85] at various film spots (beam diameter 100 μm), which is consistent with the thickness variations observed with TEM (Fig.4.1).

4.1.7. Conclusions

The systematic study of in-plane phonon propagation in PC / PMMA multilayer films revealed complex dispersion relations with two or more structure related modes. For periodicities much less than the phonon wavelength, the dispersion relation displays an effective homogeneous medium behavior with the propagation of two phonons with longitudinal and transverse polarization. The confinement in the layered structure impacts only the shear modulus, which was found to increase with decreasing layer thickness. FEA is employed to compute the theoretical dispersion relation and provides a good general agreement with experiment using no fitting parameters. The temperature dependence of the phonon phase velocities is used to identify the nature of the observed propagation modes and provides a measurement of the T_g of the individual polymer nanolayers.

4.2. High impedance contrast 1D-Periodic Hybrid Structures

4.2.1. Introduction

In the previous chapter we considered the case of mechanical waves in nanostructured multilayer films and the influence of boundaries on their propagation nature. Such multicomponent systems with small acoustic impedance mismatch (Z = $\rho\nu$) between the pure phases do not support phonon localization and exhibit an effective medium behavior. Phononic crystals [99] (Fig. 4.9) represent a novel class of materials that enable the systematic manipulation of elastic energy flow and hence opening pathways for exploration of entirely new phenomena. The substantial contrast of the acoustic impedance between the different components is the necessary condition for phonon localization. The mechanical analogues of photonic crystals [100], exhibit periodic modulation in density and / or elastic moduli, giving rise to unique properties, such as the formation of phononic band gaps and negative refraction [100]. Efforts to control the propagation of elastic waves with frequencies ranging from sound ($10^2 - 10^4$ Hz) to heat (10^{12} Hz) resulted in numerous phononic structures [101] with wide meso-scale dimensions.

Recent technological advances allowed the fabrication of periodic materials in the the submicron scale [102, 103], thus shifting the investigation of phononic properties in the hypersonic (GHz) [104, 105] and even sub-THz range [106]. In particular, due to the relative simplicity of fabrication, one-dimensional (1D) superlattices and multilayer films have been extensively investigated for their novel electronic, optical, thermo-mechanical and acoustic properties [107–109]. The potential use of 1D periodic structures as candidates for photonic[100] and phononic[110] applications has been highlighted, yet the experimental realization of hypersonic phononic band gaps so far is restricted in 2D and 3D systems. This limitation mainly stems from the lack of experimental techniques to probe characteristic length scales in the order of the periodicity of such nanostructures. A detailed understanding of phonon propagation in periodic media is the precondition to access fundamental concepts such phonon- photon interactions [111, 112] and heat management [99].

In this chapter, the first direct experimental observation of a hypersonic phononic band gap in a 1D periodic hybrid system will be demonstrated. The dispersion relations of a multilayer stack of alternating SiO_2 and poly-(methyl methacrylate) (PMMA) nanolayers were probed directly for phonon propagation in the periodic direction. Finite element analysis (FEA) was used to study the impact of porosity and interfacial effects on the phononic properties. An excellent agreement with experimental findings was observed.

4.2.2. Experimental

Nanocrystalline materials and amorphous polymers represent excellent candidates for designing 1D phononic crystals due to their intrinsic properties such as high modulus contrast and optical transparency. In addition, a wide range of multicomponent morphologies is feasible due

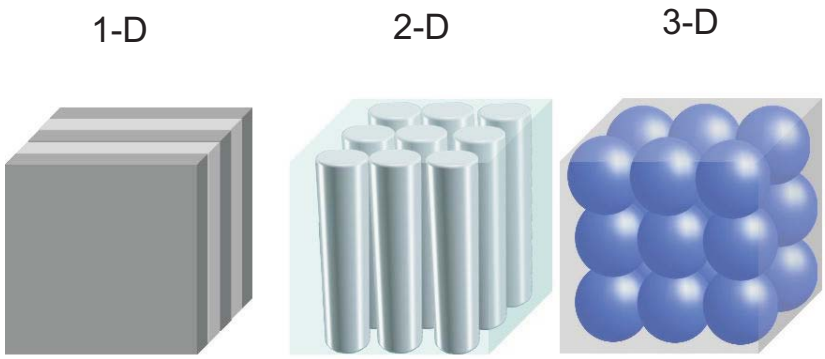

Figure 4.9.: Examples of phononic crystals with periodicities in one, two and three dimensions.**Left**: A one- dimensional phononic crystal consisting of elastic layers made of materials with different mechanical properties. **Center**: A two- dimensional phononic crystal consisting of elastic cylinders in a backround elastic material. **Right**: A three dimensional phononic crystal of spheres in a backround elastic medium.

to their facile processibility. In order to fabricate the hybrid phononic structures (Fig. 4.10a), inorganic SiO_2 nanoparticles and PMMA have been used as high and low elastic modulus materials, respectively. Prior to spincoating, glass and silicon substrates were cleaned in a piranha solution containing conc. sulfuric acid and hydrogen peroxide 30 % (2:1, v / v) for 30 min. Phononic crystals consisting of 20 SiO_2 / PMMA bilayers were built up by sequential spincoating of a 2.2 % (w / v) solution of PMMA (Acros, M_W = 35 kDa) in toluene and 3.4 % LUDOX AS-30 (Aldrich) containing 0.1 % sodium dodecyl sulfate (SDS) in 14 % ammonium hydroxide solution. To control the thickness of individual layers (65 nm of SiO_2 / 35 nm of PMMA), spincoating was performed with speed 5000 rpm, acceleration 5400 rpm/s, for 20 s. After each coating cycle the samples were subjected to heat treatment at 100 ^oC for 15 min.

The direction dependence of phonon propagation is investigated by the two scattering geometries [62] mentioned extensively in previous sections. In-plane mechanical properties are probed using the transmission geometry, while reflection geometry provides access to phonon characteristics along the periodicity direction of the crystal (Fig. 4.10b). In the present study, the polarization of both incident and scattered light was always selected to be perpendicular (V) to the scattering plane.

4.2.3. Results and discussion

4.2.3.1. In-plane phonon propagation

Figure 4.11a displays polarized Brillouin spectra of the pure phases and the hybrid structure, recorded at $q_{||}$ = 0.0167 nm^{-1} for phonon propagation parallel to the surface of the film. The observed linear depedendence $f\,(=\omega/2\pi)$ vs q shows purely acoustic behavior for the phonon

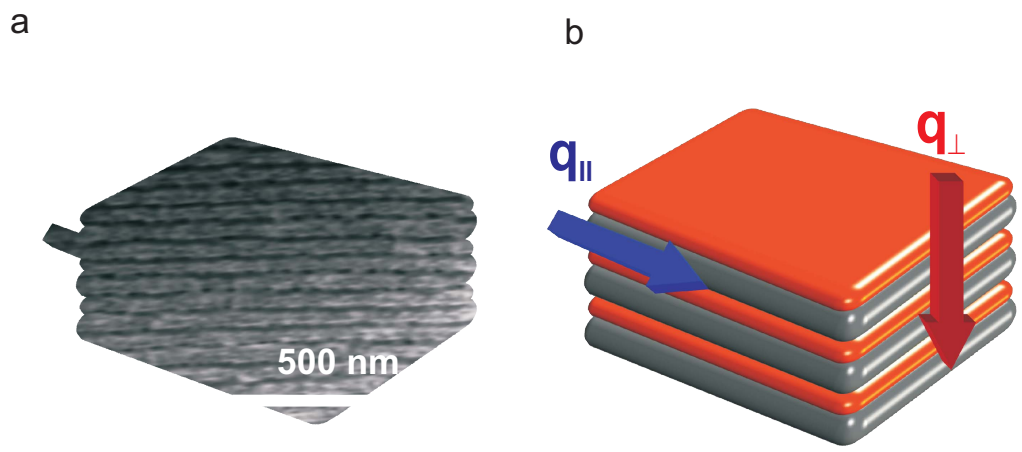

Figure 4.10.: **a,** Scanning electron microscopy (SEM) image of the SiO_2-PMMA multilayer film cross section. **b,** Schematic representation of the scattering geometries. The red and blue arrow correspond to phonon propagation normal and parallel to the plane of the film respectively.

propagation in both phases (Fig. 4.11b). Hence, the longitudinal sound velocity amounts to 2800 ± 30 m/s and 3370 ± 30 m/s for PMMA and SiO_2 respectively. The latter is clearly lower than the longitudinal sound velocity in the conventional glass ($\sim$ 5750 m/s) as indicated by the slope of the solid line in Fig. 4.11b. This reduced value for the present SiO_2 block is attributed to the porosity which is formed during the fabrication process. The hybrid structure also exhibits a single doublet spectral feature (Fig. 4.11a) that suggests a homogeneous structure since the probing length scale $2\pi/q_{\parallel}(\sim 380$ nm) exceeds the bilayer thickness (100 nm). The obtained sound velocity $c_l = (2\pi/q_{\parallel})$ = 3160 $\pm$ 30 m/s (*f* the frequency of the phonon), falls between the sound velocities of the two individual materials. Assuming a homogeneous ($hq_{\parallel} \ll 1, h$ being the thickness) two component medium, the sound velocity c_l in the hybrid material with a SiO_2 volume fraction ϕ = 0.65 can be estimated by the effective medium Wood's law using c_{PMMA} = 2800 m/s and c_{SiO2} = 3370 m/s [2]. The computed value c_l = 3150 m/s is in excellent agreement with the experimental value (3160 $\pm$ 30 m/s).

4.2.3.2. Out-of-plane phonon propagation

For phonon propagation normal to the film, a different behavior is observed. Figure 4.12 shows polarized Brillouin spectra of the hybrid material recorded at three different scattering

[2] $1/\rho c^2 = \phi/\rho_{SiO_2} c^2_{SiO_2} + (1-\phi)/\rho_{PMMA} c^2_{PMMA}$, with $c_{SiO_2} = (3370 \pm 30) m/s$ and $c_{PMMA} = (2850 \pm 40) m/s$ using the values for densities ρ_{PMMA} = 1 gr / cm^3 and ρ_{SiO_2} = 1,42 gr / cm^3

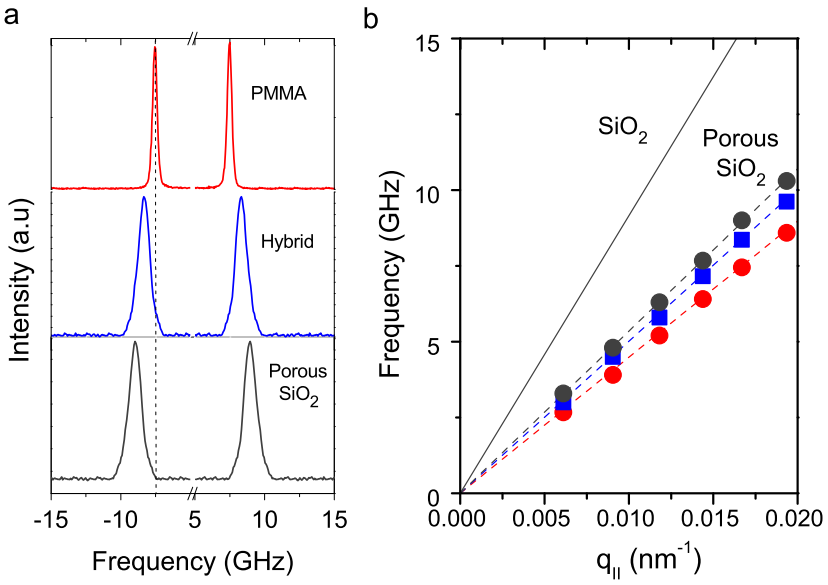

Figure 4.11.: **a,** BLS spectra at $q_{||}$ = 0.0167nm $^{-1}$ for sound propagation parallel to the surface of the pure PMMA, porous SiO_2 layer and hybrid SiO_2 / PMMA multilayer film **b,** Dispersion relations for PMMA (red points), porous SiO_2 (gray points) and the hybrid film (blue squares) for wave propagation parallel to the film whereas the dashed lines indicate the corresponding linear fits. The solid line indicates the linear (acoustic) dispersion in a conventional glass film (SiO_2).

wavevectors near the Brillouin zone (BZ) boundary at $q_{BZ} = G$; for the present 1D stack q_{BZ} = π/h = 0.0341 nm^{-1}. For $q_\perp < q_{BZ}$, the BLS spectrum at 0.0301 nm^{-1} displays a single doublet which splits into a double doublet, when the value of $q_\perp$ crosses q_{BZ} of the first BZ shown for two spectra at 0.0324 nm^{-1} and 0.0349 nm^{-1} . The spectra at the transition range can be well represented (red lines) by either a single or a double Lorentzian line shape. The clear qualitative spectral change across the BZ boundary of the present 1D periodic medium is reminiscent of a stop band of the elastic waves due to their interference as a result of the discrete translational periodicity of the phononic structure.

More detailed information on the out of plane (along the symmetry axis) phonon propagation can be obtained from the dispersion relation, $f^{(i)}$ (i = 1,2) versus $q_\perp$ (Fig. 4.13). For the hypersonic phononic crystal, this dispersion diagram reveals the presence of a unidirectional stop band at a central frequency f = 12.6 GHz with a width Δf = 3 GHz i.e., a relative gate of $\Delta f/f$ = 24% . This stop band opens close to $q_{BZ} \approx$ 0.0314 nm^{-1} for the 1^{st} BZ (blue vertical solid line) and hence coined a Bragg gap. The propagation of hypersonic longitudinal phonons vertical to the layers (unidirectional gap) with frequencies within the marked blue region is forbidden. Due to beam reffraction in the reflection geometry the low $q_\perp$ range is inaccessible and therefore the single BLS spectrum cannot be recorded at long phonon wavelengths ($q_\perp \ll q_{BZ}$). This missing acoustic branch (dashed blue line in Fig. 4.13), however,

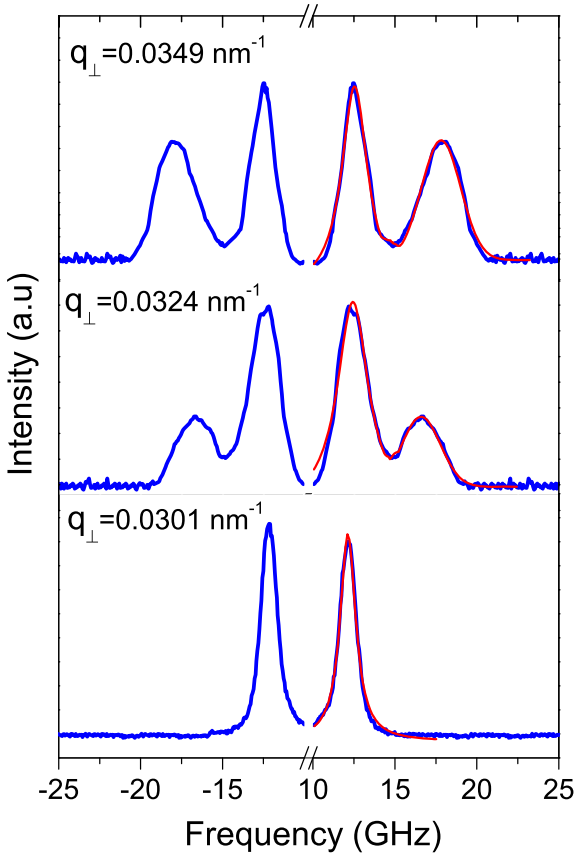

Figure 4.12.: BLS spectra of the hybrid SiO_2 / PMMA film at three different $q_\perp$ values near the Brillouin zone BZ boundary (q_{BZ} = 0.0314 nm^{-1}). The red solid lines, shown only for the transition $q_\perp$ -range can be well represented (red lines) by either a single or a double Lorentzian line shape. The clear qualitative spectral change across the BZ boundary of the Stokes side, denote the representation of the experimental spectra by a single or double Lorentzian lineshapes, respectively below and above q_{BZ}.

is easily accessible for the in-plane phonon propagation (Fig. 4.11b) which is also shown in Fig. 4.13 (solid squares). The in-plane and out-of-plane phonon propagation appears to fall on the same acoustic branch indicative of a single effective medium sound velocity along both symmetry directions . This further implies that the present hybrid SiO_2 / PMMA stack exhibits mechanical isotropy, since the density is expected to be isotropic.

Finite element analysis was performed to compute the phononic band structure [102, 103] by solving the elastic wave equation in an infinite, one-dimensional periodic medium. The model assumes perfectly bonded, ideally flat layers with uniform thickness, no roughness and defects, no spatial variations in elastic properties within a given layer and zero interface thickness. We treated the porous SiO_2 component layer as an effective medium, as verified with a separate

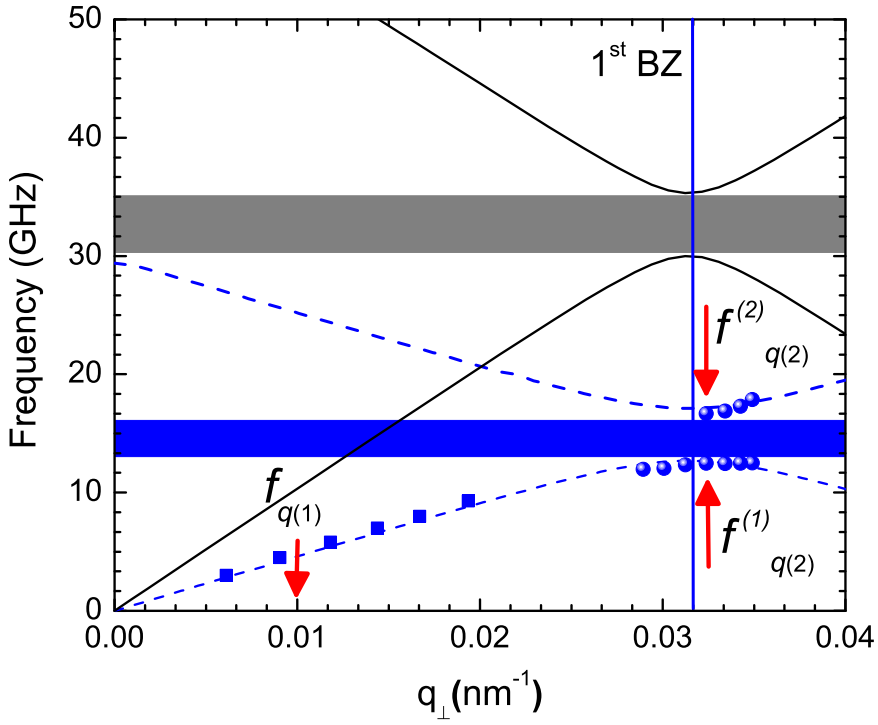

Figure 4.13.: Experimental dispersion relation for phonon propagation along the direction of periodicity. The highlighted blue region indicates the observed hypersonic band gap. The blue dashed and black solid line correspond to the computed band diagram of PMMA / porous SiO_2 and PMMA / pure SiO_2 respectively. The solid circles and squares denote the experimental data for out-of-plane ($q_\perp$) and in-plane ($q_\parallel$, Fig. 4.11) propagation

experimental measurement of a single SiO_2 layer (Fig. 4.11). The experimental values obtained from the single porous SiO_2 and PMMA layers were used directly in the calculations. In general, the interfaces will exhibit some degree of roughness that might lead to incoherent scattering of higher frequency phonons, and further suppression of phonon transport. However, the degree of this incoherent scattering component depends on the ratio of the wavelength of the phonons probed and the characteristic interface roughness; the interface roughness in the structure is typically less than 30 nm, well below the effective medium requirement ($\sim$ 1 / 5 of probing wavelength). Thus, the probed wavelengths are unable to resolve the inhomogenities in the individual SiO_2 layer and hence for the frequency region of interest, we can model the system as an infinite one dimensional periodic medium, with flat interfaces.

Figure 4.13 visualizes the good agreement between the theoretical and the experimental dispersion relations. The blue and black dashed lines correspond to the computed band diagram

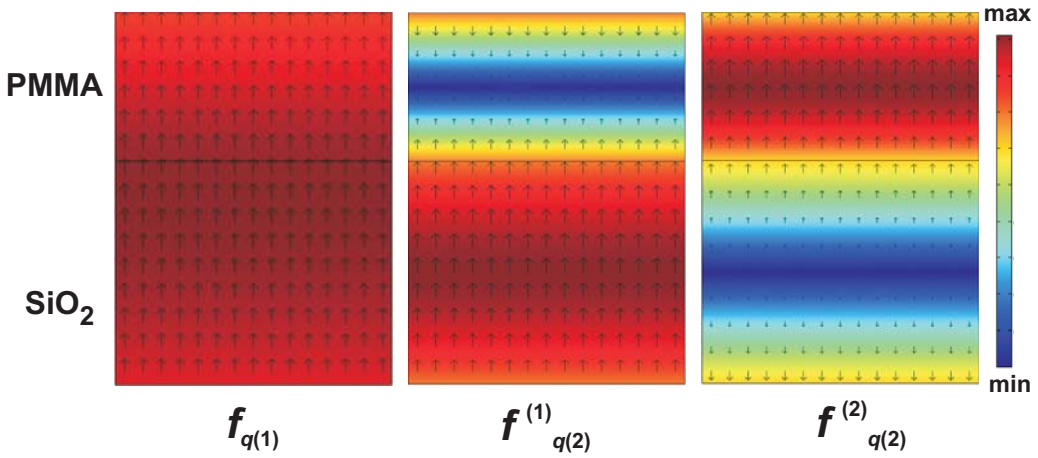

Figure 4.14.: Displacement field of lower band edge mode ($f^{(1)}$ at $q^{(2)}$) (middle), showing that the displacement fields are concentrated in the SiO2 block and displacement field of upper band edge mode ($f^{(1)}$ at $q^{(2)}$) (right), showing that the displacement fields are concentrated in the PMMA block. Color bar shows displacement field variation. Left panel shows the displacement field for a low q value ($q^{(2)}$ = 0.01 nm^{-1}) where the system exhibits an effective medium behavior.

of PMMA / porous SiO_2 and PMMA / pure fused SiO_2 respectively. For the latter system the Bragg gap opens at frequency 30 GHz with a width of about 5 GHz ($\Delta f/f$ = 17 %) as indicated by the grey area. Here, we see a manifestation of the effect of porosity on the phononic properties of the hybrid structure. The width of the gap is directly related to the impedance contrast of the component layers, both in the elastic constants (Modulus, Poisson's ratio) as well as mass density contrast.

The computed displacement fields of the lower and upper band edge modes, within a single repeat unit of a 100 nm layer are shown in Fig. 4.14. The displacement fields reflect the difference in nature of the modes, the lower (upper) modes being concentrated in the stiffer (softer) SiO_2 (PMMA) blocks. This is a consequence of the one-dimensional discrete translational periodicity of the phononic crystal that couples eigenmodes with $\boldsymbol{k}$-vectors of $\boldsymbol{k} = \boldsymbol{G}/2$ and -$\boldsymbol{G}$ / 2. These two modes interact and form the upper and lower band edge modes, opening a band gap in the process. As a result of the translational symmetry, the formed two band edge eigenmodes are stationary modes with the same period as the phononic crystal but their displacement fields are phase shifted with respect to each other by half a period. This is a direct result of the symmetry coupling and is independent of the exact thicknesses of the PMMA and the SiO_2 layer, i.e. the lower (upper) edge mode will have the displacement field concentrated in the stiffer (softer) block, which is lower (higher) energy, and this distinction in the band edge modes is most clearly manifest in the one-dimensional periodic system. As expected for an effective medium behavior, the displacement field is uniformly distributed in both layers for long wavelength phonon propagation (left panel in Fig. 4.14).

4.2.4. Conclusions

We see here a clear agreement between theoretical prediction and experimental measurement on the phononic dispersion of a 1D periodic phononic crystal. It is also seen that a porosity of 30% leads to a 20 GHz reduction in the gap opening frequency; in addition, it is experimentally shown that the porosity does not impede the gap opening in these systems. This demonstrates the possible usage of this PMMA / SiO_2-porous phononic crystal as an efficient passive tunable GHz filter. By tuning the porosity of the SiO_2 block, while maintaining the structural integrity, or even as a dynamic filter, by subsequent infiltration of the same porous SiO_2 with different solvents or reactive agents to tune the Bragg gap for filtering, or sensing applications.

5. Phononic Biomaterials: Spider dragline silk

5.1. Introduction

Many natural and man made materials exhibit structure on more than one lenght scale;in some materials, the structural elements themselves have structure. This hierarchy can play a major role in determining the bulk materials properties. Examples of natural hierarchical materials include wood [113], tendon [114], trabecular bone and silk. Of these systems, spider dragline silk, has been extensively investigated, due to its superior properties compared to synthetic polymers with similar chemical structure, such as polyamides. The dragline is one specific fiber out of seven different silk types which a spider has at hand. The orb webs radii and the webs frame are built from dragline fibers, which have typical diameters in the range of 1-10 μm, depending on the species. Dragline also acts as the spiders life line, catching the spider when she drops from her web in moments of danger. Correspondingly, it is optimized for tensile strength, extensibility, and energy dissipation. Energy dissipation prevents unwanted springlike elasticity in functions related to catching of prey and stopping the spider from a free fall.

Spider dragline silk is a semi-crystalline biopolymer, produced in the spiders major ampullate gland [115–117]. During this process the aqueous solution of the two protein constituents of dragline silk is crystallized, while the macromolecules maintain their high orientation order [118]. Attempts to reproduce this procedure in the lab have been recently published [119, 120]. In spite of the experimental effort, the full elucidation of its structural organization is still missing. The alanine and glycine-rich proteins are organized in oriented β -sheet nanocrystals connected by amorphous chains and less crystalline domains [121–123]. In addition to the known primary and secondary structure, there is non-periodic supramolecular order at larger length scales [124–127]. The two protein constituents are not uniformly distributed and the peptide assembly leads to the formation of nanofibrils with size of a few hundred nanometers [123]. The utilization of X-ray microscopy has identified highly oriented, along the fiber axis, domains with size of the order of the nanofibrils and a total volume fraction of about 30%, dispersed in a moderately oriented dominant medium [126]. These domains are characterized by a high density in nanocrystallites and represent the hard components of the structured composite material.

This multilevel structural organization adds to the spider dragline silk its unusual and tunable mechanical properties including high tensile strength and toughness [117, 128–131]. A key

factor that controls these properties is the pre-strain of the amorphous chains, which is created during spinning, and can be released when silk is exposed to humidity and is allowed to shrink - "supercontract" [129, 132, 133]. The high value of the Young's modulus (in the order of 10 GPa) along the fiber is well documented by mechanical techniques [130, 134] at the low resolution (long wavelength deformation) of typical elastic stress-strain experiments. The elastic modulus in the normal direction, however, is not accessible by these techniques and the effect of the benign fiber processing with regard to mechanical anisotropy still remains unknown. Yet the propagation of elastic (acoustic) waves with short wavelengths, which commensurate characteristic length scales of the spider dragline silk, can reveal unprecedented properties of this fascinating natural product. It is the sensitivity of the wave propagation through structured composites and the vector nature of the elastic field that makes the dispersion relation i.e. frequency (f) vs. wavevector (q) a rich source of information on structure and nanomechanics.

5.2. Experimental

The samples used are major ampullate silk fibers (Fig. 5.1a,b)from Nephila edulis spiders, obtained by forced silking [135] at a speed of $\sim$ 1mm/s, room temperature of 23 $\pm$ 1 ^{o} C and relative humidity 35 $\pm$ 5 $\%$. The silk fibers are wound around two metal rods in order to form a 6 mm long dense double-layer grid (Fig. 5.1c). Fiber thickness at zero strain is measured by laser difraction and is found to be 3.3 μm. Two special scattering geometries are adopted to select the direction of $\mathbf{q}$ either parallel ($\mathbf{q}_{\parallel}$ in Fig. 5.1d) or normal ($\mathbf{q}_{\perp}$ in 5.1e) to the fibers. The magnitude of $\mathbf{q}_{\parallel}$ and $\mathbf{q}_{\perp}$ are given in the caption of 5.1, and only $\mathbf{q}_{\perp}$ depends on the refractive index n = 1.55. The individual fibers (Fig. 5.1b) are sufficiently thick to assure bulk light scattering free of confinement effects.

5.3. Results and discussion

5.3.1. Mechanical strength directionality

First we examine the dispersion for the elastic wave (phonon) propagation normal to the fiber. According to the current picture of the spider dragline silk the dense crystalline (hard) domains are well oriented with their long axis along the fiber. The preferred alignment of most covalent bonds of both crystalline and amorphous regions along the fiber axis implies that in the normal direction the contrast of elastic moduli should be low. Hence the material appears homogeneous over the probing length scale 2π / $q_{\perp}$ ($\sim$ 170 nm). Indeed the experimental BLS spectrum displays a single doublet as seen in the lower panel of 5.2a at $q_{\perp}$ = 0.0365 nm^{-1}. The frequency of the peak ***(1')*** increases linearly with $q_{\perp}$ as indicated by the red dashed line in the shaded region of 5.2b. Its acoustic behavior allows the determination of the effective medium sound velocity $c_{\perp} = \omega / q_{\perp}$ = 3140 $\pm$ 40 m/s and the longitudinal modulus $M_{\perp} = \rho\, c_{\perp}^{2}$ = 12.3 $\pm$ 0.2 GPa (using the bulk density ρ = 1.25 g / cm^3) [136]. This modulus is inaccessible

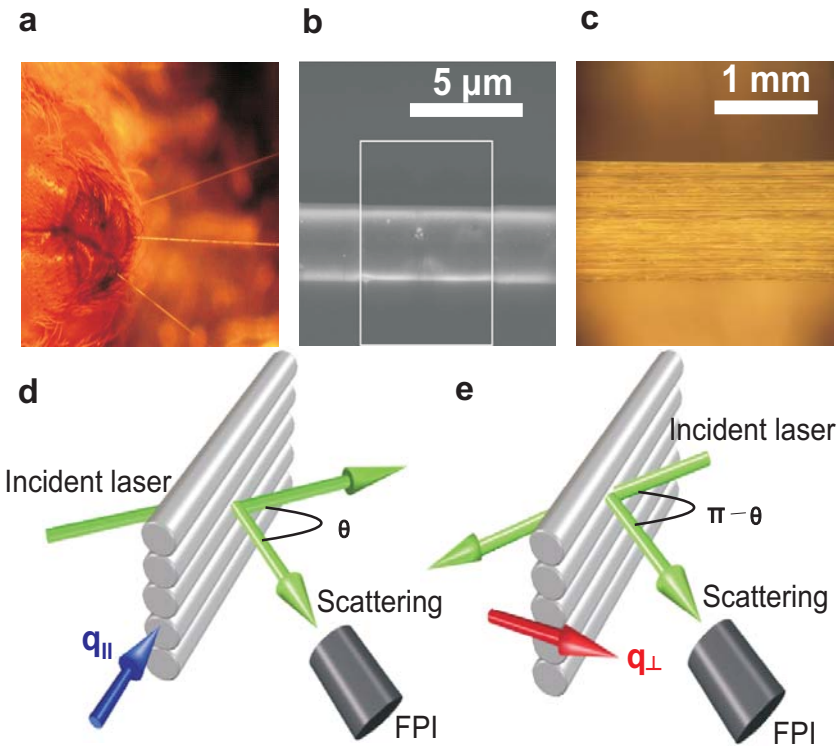

Figure 5.1.: **Access to the mechanical properties along and normal to the spider dragline fiber.** **a,** View of the spider spinnerets under the microscope. Both major and minor ampullate fibers are shown, but only the major (depicted in the frame) is collected and used for the BLS measurements. **b,** Scanning electron microscope image of a spider dragline silk fiber. **c,** Grid of parallel fibers on the cell holder. **d** and **e,** Light scattering geometries allowing for probing the elastic constants either parallel (transmission mode) or normal (reflection mode) to the fiber long axis. The two arrows indicate the direction of the scattering wave vector **q** with magnitudes: $q_{||} = (4\pi/\lambda)sin(\theta/2)$ and $q_{\perp} = (4\pi n/\lambda)sin(\theta/2)$ where θ is the scattering angle and λ the wavelength of the incident laser beam. A high resolution six-path Fabry-Perot Interferometer (FPI) records the Brillouin light spectrum rejecting the elastically scattered photons.

to the conventional techniques and is reported for the first time. It assumes a value typical for synthetic bulk amorphous polymers [137].

A qualitatively different behavior is observed for phonon propagation parallel to the fiber axis. The experimental BLS spectra now exhibit a double doublet spectral line shape as seen in the upper part of Fig. 5.2a for $q_{||} = 0.0167\text{nm}^{-1}$. The nature of the two peaks ***(1)*** and ***(2)*** is

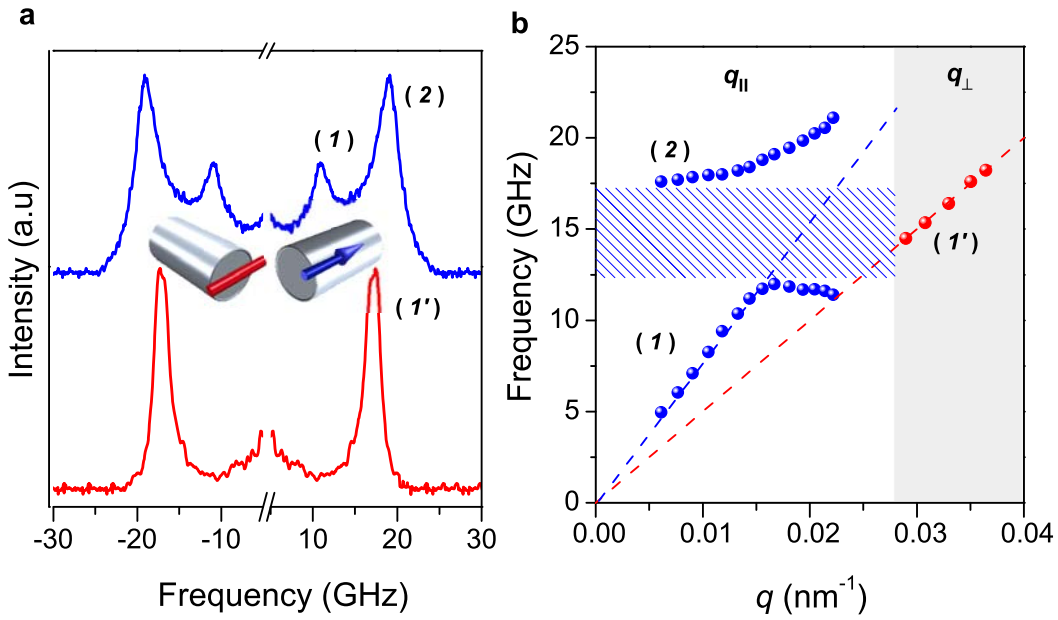

Figure 5.2.: **BLS spectra and experimental dispersion diagram of the native spider dragline silk along two symmetry directions. a,**BLS spectra at $q_{\parallel}$ = 0.0167 nm^{-1} (in blue) with two peaks (***(1)*** and ***(2)***) along the fiber and at $q_{\perp}$ = 0.0365 nm^{-1} (in red) with one peak ***(1')*** normal to the fiber axis. **b,** Dispersion relations for modes ***(1)*** and ***(2)*** (blue points) and mode ***(1)*** (red points) representing elastic wave propagation parallel and normal to the fiber, respectively. The two dashed lines indicate the effective medium sound velocities in the two directions whereas the hatched area denotes the unidirectional stop band.

unraveled in the dispersion plot of 5.2b. At long phonon wavelengths (low $\mathbf{q}_{\parallel}$'s), mode ***(1)*** is acoustic leading to the effective medium sound velocity $c_{\parallel} = \omega / q_{\parallel}$ = 4970 $\pm$ 30 m/s which is about 60% higher than $c_{\perp}$. The high value of the longitudinal modulus $M_{\parallel} = \rho\, c_{\parallel}^2$ = 31$\pm$ 0.1 GPa demonstrates the large mechanical anisotropy $M_{\parallel} / M_{\perp}$ = 2.6$\pm$ 0.05 of native silk. The direction dependence of the mechanical properties is consistent with the high orientation order along the fiber [118, 122, 126, 129, 133, 135]. On the other hand, the low value of the longitudinal modulus normal to the fiber is due to the amorphous dispersion medium and the low modulus of the nanocrystals in this direction.

5.3.2. Structural dependence of Elastic energy flow

The dispersion relation for wave propagation along the fiber in Fig. 5.2b shows the unexpected opening of a large stop band at a frequency f_g = 14.7 GHz with a width Δf_g = 5.3 GHz (hatched area in Fig. 5.2b) i.e., a normalized width Δf_g^*(= Δf_g / f_g) $\sim$ 0.36 at hypersonic frequencies from about 12.5 GHz to 17.5 GHz. To the best of our knowledge this is the first observation of a phononic gap in biological structures. In order to investigate the relation of supramolecular structure and the observed unidirectional gap, a regenerated silk sample is compared. The crystalline structure was destroyed by dissolving the native fiber in hexafluoroisopropanol and subsequent spin-coating and drying at 100 ^{o}C under vacuum for 2 days. The absence of crystallinity was documented using infrared spectroscopy and the finding is in accord with literature reports [138]. The BLS spectra of a $\sim$5 μm thick film of the regenerated silk are single doublets for both in-plane and normal to the film plane directions (Fig. 5.3a). The dispersion diagram of Fig. 5.3b (solid triangles) corresponds to a purely acoustic behavior yielding c = 2890 $\pm$ 30 m/s irrespectively of the propagation direction, characteristic of a homogeneous medium that exhibits isotropic mechanical properties. Notably, the sound velocity (and hence the modulus (8.4 GPa)) is lower than $c_\perp$ (red dashed line) but much slower than $c_\parallel$ (blue dashed line) compared with the values from the native fiber in 5.2b. Post treatment with methanol [139] effectively induces the formation of β -sheet nanocrystals isotropically distributed in the film, but does not recover the long range structural hierarchy of the native fiber. Indeed the dispersion diagram (Fig. 5.3b) (open squares) still exhibits only an acoustic branch independent of the phonon propagation direction, resulting in c = 3070 $\pm$ 30 m/s, i.e., 6% higher than the amorphous regenerated film.

Unlike colloidal crystals [137] and other systems [140] with periodical structure at length scales comparable with the phonon wavelength 2π / q, in this case the gap is not Bragg-type [35]. However, structural techniques suggest the existence of nanofibrils with characteristic size $\sim$ 100 nm [124–126], even though no evidence for their nature is provided. Such a phononic gap has not been observed in other semi-crystalline systems with similar chemical structures, such as polyamides. The BLS spectrum of a 15 μm thick film of Nylon-6 consists of a single doublet for both in-plane and normal to the film plane phonon propagation (Fig. 5.4a). The dispersion diagram of Fig. 5.4b presents a purely acoustic behavior for both directions and the corresponding sound velocities amount to $c_\parallel$ = 3700 $\pm$ 30 m/s and $c_\perp$ = 2830 $\pm$ 30 m/s. The higher in-plane sound velocity is attributed to the high orientation of the chains along this direction. The longitudinal modulus anisotropy $M_\parallel$ / $M_\perp$ = 1.7 (assuming isotropic density in the film) is clearly lower than the native ($M_\parallel$ / $M_\perp$ = 2.6) spider silk fiber. This finding implies that order at longer length scale exists in silk.

In the gap region, the group velocity for mode ***(1)*** becomes zero and elastic energy flow ceases. The high frequency mode ***(2)*** is flat (optic-like) at low $q_\parallel$, i.e. it is localized in real space. Such modes relate to material oscillations of particle-like objects in analogy to the molecular vibrations [35, 137]. In order to resolve such vibrations in a continuous medium, an elastic impedance (Z = ρ c) contrast (ΔZ) between the particle (c_p) and the surrounding medium (c_m) must be present. This requirement is fulfilled since c_p ($> c_\parallel$) and c_m ($> c_\perp$) are

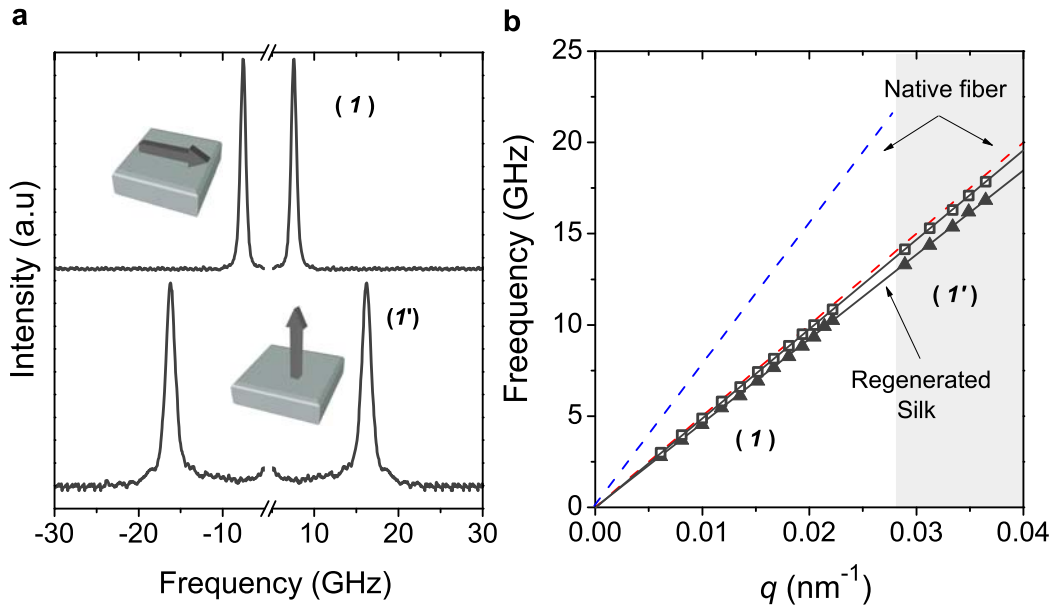

Figure 5.3.: **Erase of the gap and mechanical anisotropy in regenerated amorphous and semicrystalline silk. c,** BLS spectra at $q_{\parallel} = 0.0167\ nm^{-1}$ and $q_{\perp} = 0.0365\ nm^{-1}$ respectively parallel and normal to the amorphous film and **d,** Linear dispersion relation for the acoustic modes ***(1)*** and ***(1')*** in the two directions for the amorphous (solid triangles) and semicrystalline (open squares) regenerated films. The sound velocity for the acoustic branch ***(1')*** in the native fiber (red dashed line) is moderately higher than the sound velocity of the single acoustic phonon in both the regenerated amorphous and semicrystalline films.

different yielding a large ΔZ ($\rho\ c_{\parallel} / c_{\perp}$)-1 0.6. This implies that, despite the lack of periodicity in the fiber [125, 126], the degree of crystallinity and, consequently, the elastic modulus varies at submicronscale consistently with the structure characterization techniques [126, 127]. The observation of the mode ***(2)*** only for $q_{\parallel}$ indicates that the direction of the displacement field is along the fiber axis and hence only coupling with the acoustic mode ***(1)*** and not ***(1')*** is allowed. The interaction between the propagating density fluctuations in the effective medium (acoustic branch ***(1)***) occurs in the $q_{\parallel}$ region when the frequency *f(1)* becomes of the order of the vibration frequency *f(2)*, i.e. at $q^*_{\parallel} \sim 2f(2)/c_{\parallel}$. For a spherical particle in air, *f(2)* = κ (c_p / d) where d denotes the diameter and κ = O(1) is a shape dependent constant [35, 137]. The roughly estimated size (2π / $q^*_{\parallel} \sim$ 280 nm) is clearly larger than the individual nanocrystals.

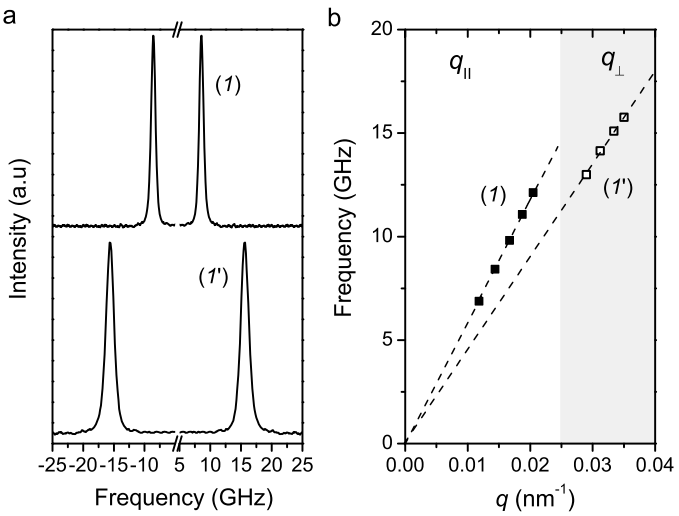

Figure 5.4.: **a,** BLS spectra at $q_{||}$ = 0.012 nm^{-1} (upper panel) and $q_{\perp}$ = 0.035 nm^{-1} (lower panel) parallel and normal to the film respectively, at 25 ^{o}C. **b,** Linear dispersion relation for the acoustic modes normal (open squares) and parallel to the plane of the film (solid squares).

5.3.3. Gap tuning- Effect of Strain and Supercontraction

To further support the association of these structural features with the unexpected phononic properties of the spider dragline silk, we have studied fibers with decreased or increased pre-strain created by supercontracting or stretching, respectively. The breaking of hydrogen bonds in the amorphous regions, allows the chains to reach a conformation closer to equilibrium, while the distribution and orientation of crystals is minimally affected [129, 132, 133, 135]. The reduced pre-strain increases the contrast between nanocrystals and the interconnecting amorphous chains and, therefore, between domains of higher and lower crystallinity. In addition, all spacings along the fiber are inevitable scaled down due to shrinking. These effects are reflected in the dispersion relation for the supercontracted fiber (at -20% strain) Fig. 5.5a. The effective medium $c_{||}$ (= 4270 $\pm$ 20 m/s) of the acoustic branch ***(1)*** decreases by about 15% (due to decrease of c_m) whereas the stop bandwidth Δf_g^* ($\sim$ 0.47) increases by 30% (due to the increase of ΔZ) compared to the native fiber (Fig. 5.2). As expected, the phononic properties of the native fiber are essentially recovered by stretching the supercontracted fiber to strain 0% (Fig. 5.6 at 0% strain).

The worm-like amorphous chains become stiff only when significantly stretched. Similarly, the stress-strain curves of supercontracted silk exhibit a large plateau [129, 133]. A stronger dependence on strain for the native fiber (Fig. 5.5) has to be anticipated, because now the pre-strained chains become stiffer with an only small additional strain. The stretching of the native fiber has a higher impact on the sound velocity cm of the moderately oriented dispersion

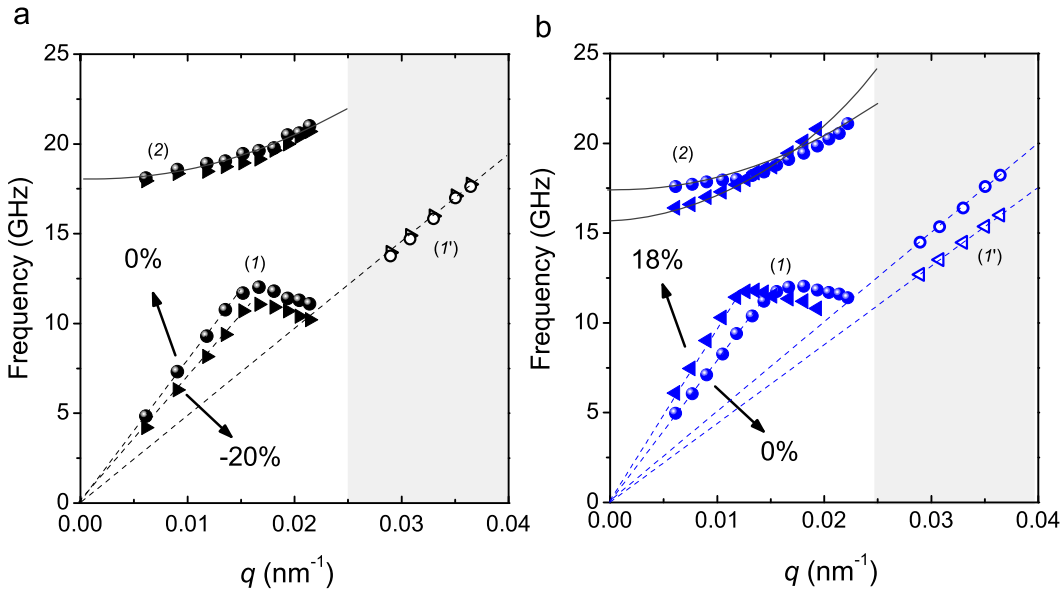

Figure 5.5.: The effect of strain on the dispersion diagram and the mechanical anisotropy of native and supercontracted fibers. Dispersion diagrams for wave propagation parallel (modes ***(1)***,***(2)***) and normal (mode ***(1')*** (at $q_\perp > 0.025$ nm^{-1}) to: **a,** A supercontracted fiber at -20% (black solid and open triangles respectively) and 0% strain (black solid and open circles respectively) and **b,** A native fiber at 0% (blue solid and open circles respectively) and 18% strain (blue solid and open triangles respectively). Strain values are calculated with respect to the unstretched native fiber length and hence the values for the supercontracted sample are negative.

medium of the native fiber than on c_p. This imparts both the contrast ΔZ (and hence the stop band width) and the effective medium sound velocity, $c_\parallel$. At 18% strain (Fig. 5.5b), $c_\parallel$ (= 6260 $\pm$ 60 m/s) increases by about 27%, whereas the bandwidth Δf_g^* ($\sim$ 0.24) decreases by about 30%, compared to the (unstrained) native fiber. What distinguishes the stretching of the native fiber from the stretching of the supercontracted fiber is now the clear decrease of the value of $q_\parallel$ beyond which the bending of ***f(1)*** occurs. This corroborates the notion that the characteristic spacing along the fiber increases upon stretching. Since the mechanical properties of silk in the normal direction are minimally affected by pre-strain, the mechanical anisotropy $M_\parallel$ / $M_\perp$ consistently increases with strain (Fig. 5.6b); just before breaking (at about 18% strain), the fiber reaches a high $M_\parallel$ / $M_\perp \sim 5$. Notably, the longitudinal modulus anisotropy in semicrystalline systems with similar chemical structures is much lower (Fig. 5.4).

Based on this study, the structure is schematically depicted in Fig. 5.7. The nanocrystals are

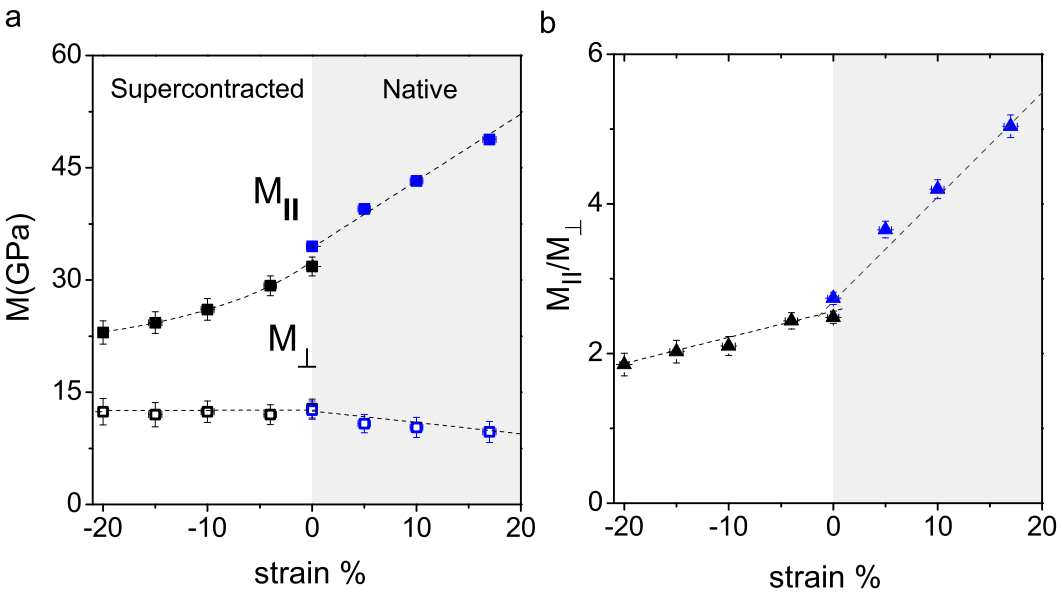

Figure 5.6.: ***a,*** Longitudinal moduli parallel and normal to the fiber for the native (blue solid and open squares respectively) and supercontracted (black solid and open squares respectively) silk. **b,** Mechanical anisotropy versus strain for the native (blue triangles) and supercontracted (black triangles) silk.

non-uniformly distributed in the fiber. Crystallinity varies continuously with a characteristic length scale of a few hundred nm. The variation of elastic modulus and anisotropy follows the crystallinity. According to the results of Fig. 5.6b, the anisotropy of the supercontracted sample is lower compared to the native fiber. Given that the orientation of nanocrystals remains high [129] this implies that the domains must be less elongated that in the native fiber, reflecting the shrinking and thickening during supercontraction. Stretching the native fiber boosts the mechanical anisotropy. The increased modulus in the parallel direction is primarily due to the stretching of the amorphous chains (Fig. 5.6). Therefore, pre-strain controls the phononic as well as the nanomechanical properties.

5.4. Conclusions

The dispersion relation for the elastic wave propagation in the spider dragline silk is anisotropic and displays a novel unidirectional large stop band at hypersonic frequencies, which has a different origin from Bragg-type gaps in periodic phononic crystals. In analogy to recent studies

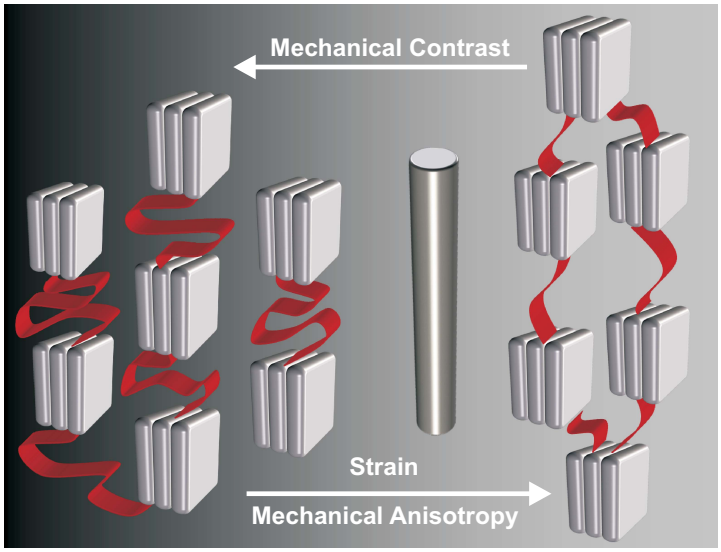

Figure 5.7.: Scheme of the structure of dragline spider silk. The fiber (rod in the middle) and magnified structures are not drawn to scale. The alanine-rich highly ordered nanocrystals with size $\sim$ 5 nm (grey blocks) are interlinked by amorphous glycine-rich chains (indicated in red) varying widely in pre-strain: While in the supercontracted state the chains are nearly relaxed, a pre-strain in the range of 0.3-0.6 [133, 135] is observed in the native and stretched fiber. The average crystallinity at submicron length scales varies non-periodically in the fiber, giving rise to the phononic band gap. The mechanical anisotropy increases and the elastic impedance contrast ΔZ (indicated by the gradient color of the background) decreases with increasing pre-strain in the direction of the arrow.

on disordered colloidal films [35] where the spherical particles act as local resonant elements, the presence of the gap in this natural material, is attributed to the existence of a correlation length of the elastic modulus of the non-periodically distributed nanocrystals embedded in the amorphous matrix. Rationalized as a hybridization gap, it opens from the overlap of such particle bands with the acoustic field of the extended states in the effective medium. The extraordinary phononic properties relate to the hierarchical structure at different length scales, whereas the direction dependent modulus is due to the high orientation order along the fiber. This unprecedented results reveals the major role of multilevel structural organization on the flow of the elastic energy. Similar findings are anticipated in a manifold of natural [141] and artificial hybrid materials, facilitating the design of novel systems with tailorable and functionally optimized properties [142].

6. Epilogue

In the present dissertation, Brillouin light scattering (BLS) was employed to explore elastic waves propagation in structured polymer based systems and elucidate the structure- nanomechanical properties relationships. The choice of the samples has provided a platform for engineering sound propagation in the GHz frequency range and aimed at probing different matter-phonon interactions. The possible thickness induced mechanical anisotropy and interfacial effects were investigated by studying thin amorphous polymer films and periodic polymeric multilayer structures. Modulation and control of elastic energy flow was then examined by focusing on hybrid multiphase artificial and biological materials possessing strong acoustic impedance mismatch. These studies extend BLS from a characterization method for thin films to a metrology for more complex confined polymeric, inorganic and biological structures. By probing complex elastic excitations and localized acoustic vibrations, BLS is found to be a powerful tool for non-contact, non-destructive analysis of elastic constants for nanoscale materials.

By utilizing the reflection scattering geometry, the moduli directional dependence of a highly anisotropic system was investigated even in length scales for which chain confinement effects become more pronounced. Non-propagating vibrations from polyimide coatings in the micron and sub-micron range were probed and related to out of plane elastic moduli. The fine structure revealed in Brillouin spectra showed that the elastic behavior is size-independent in the whole thickness range investigated. Furthermore surface waves with finite in-plane wave vectors $q_{||}$, were used to extract the in-plane elastic constants. The independence of elastic properties on thickness was verified by modeling the data with the layer-multiple-scattering method on a system that possesses transverse isotropic symmetry. Besides an adequate method for probing out-of-plane elastic properties in films, the reflection geometry of the BLS experimental setup, introduced here, provided the basis for direction-dependent studies of elastic moduli in a wide range of sample geometries.

Next, 1D periodic polymeric films comprised of alternating PMMA and PC thin layers were used to investigate phonon propagation as a function of periodicity and composition. For periodicities much less than the phonon wavelength, the dispersion relation displayed an effective homogeneous medium behavior with the propagation of two phonons with longitudinal and transverse polarization. The confinement in the layered structure impacted only the shear modulus, which was found to increase with decreasing layer thickness. Finite element analysis was used to compute the theoretical phonon dispersion relation and provide interpretation of the observed modes. Complex features of the phonon dispersion relation were attributed to elastic waves propagating within the individual polymer layers. This high sensitivity of phonon dispersion to structure and composition allowed the probing of the mechanical properties down

to the single-layer level where a strikingly different dependence of the longitudinal and shear moduli on confinement effects in the polymer nanolayers was observed. In addition, temperature dependent measurements of sound velocities revealed the presence of distinct glass transition temperatures, indicative of phonon localization in films with large layer thicknesses in agreement with theoretical predictions.

Staying in multilayer structures but increasing the impedance contrast of the component layers, led to the first experimental observation of a hypersonic Bragg gap in a system with 1D periodicity. The probed dispersion relations of a multilayer stack of alternating SiO_2 and PMMA nanolayers were modeled by Finite element analysis and an excellent agreement was found. It was shown that a porosity of 30% leads to a 20 GHz reduction in the gap opening frequency; yet, its presence does not impede the gap opening in these systems.

Finally, the fourth system was selected in the course of the work mainly on the account of its superior mechanical properties compared with synthetic semicrystalline polymers and its inherent hierarchical structure. Probing elastic excitations in spider dragline fibers, revealed the existence of a unidirectional hypersonic phononic band gap. This finding, the first realized in a biological structure, was attributed to the strong mechanical coupling between localized bands with the acoustic field. By that the existence of a strain-dependent correlation length of the mechanical modulus in the submicron range along the fiber axis was established, in analogy with recent findings observed in disordered colloidal films. Additionally a strong mechanical anisotropy for spider silk was found.

Moving forward in the development of new and miniaturized components in the age of nanotechnology, Brillouin spectroscopy could find applications for probing elastic constants of nanostructured materials in which deviations from bulk properties are expected. In the case of phonon propagation in multilayer polymeric and hybrid films, many possibilities and challenges lay ahead. Tailoring and optimized the acoustic and mechanical properties of such structures are feasible by controlling parameters like thickness, periodicity and ordering of the individual components. Concerning the building blocks, the combination of electrical conductive and optical transparent coatings such as TiO_2 or tin-doped indium oxide (ITO) in place of SiO_2, is anticipated to lead to novel control of elastic energy flow. In addition, the choice of optically anisotropic multilayer assembly with periodicity commensurate the wavelength of the visible light may allow the occurrence of confinement-induced enhancement of photon-phonon interactions. These features would offer the possibility of novel applications for phonon engineering. Finally, besides probing elastic constants of engineered artificial systems, Brillouin spectroscopy can be extended to complex biomaterials. The correlation between the structure and the mechanical properties could provide new insights into hierarchical structures and self assembly on molecular and mesoscopic length scales. An understanding of the structural origin of exotic properties found in biological systems is not only of fundamental interest but also needed in view of promising biomimetic applications.

Acknowledgements

Many people deserve recognition, and I apologize for not including everyone I have interacted with, during the last three years. I truly feel that every personal contact has contributed to my personal and professional growth.

I would like to give my most sincere thanks to my supervisor Prof. x. xxxxx. I was fortunate to work with him the last five years and as I look now back, I see that I have gained much more than research experience from our personal contact. I am also grateful to Prof. x.-x. xxxx for offering me the opportunity to work with him. The friendly atmosphere in his group and the academic freedom provided excellent research conditions. He showed faith in me when everything was going wrong. I would like to deliver my appreciation for his support.

Much of the work in this thesis resulted from collaborative efforts. My great thanks to XXXXXXXXXXXXXX and Prof. x. XXXXX, for fabricating and providing the hybrid films. I appreciate greatly XXXXXXXXX immediate and professional response to my requests.
Prof. X. XXXXXX and Dr. X. XXXXXXXXXXXX (Institute of Experimental Physics I, University of Leipzig) for their collaboration on spider silk.
X. X. XXX and Prof. X. X. XXXXXX (Dept. Mat.Sci and Eng., MIT) for the Finite element analysis calculations.
XXXXX XXXXX and Prof. X. XXXXXX (Dept. Chem., MIT) for simulations of the Lamb modes and discussions about ISTS.
Dr. X. XXXXXXX (Dept. Chem. Eng., University of Wisconsin) for the preparation of supported thin films and for intensive discussions.
My sincere thanks to XXXXXX XXXX for his consistent help on designing the strain holder.

My office mates XXXXXXX XXXX, XXX XXXXX and Dr. X. XXX for their help in various topics and for providing a nice working environment. I learned a lot from these guys. It was a privilege working together.

The Mensa companion XXXX X. XXXXXXXX, XXXXXXXXXXXX, XXXXXXXXXXXXXXXXXXXX and XXXXXXXXXXXXX.

The I.E.S.L group, Dr. XXXXXXXXX, Dr. XXXXXXXXXX, XXXXX. X, Dr. XXXXXXXX, Dr. XXXXXXXXXX, and Prof. XXXXXXXXXX. I still cherish those two wonderful years.

Prof. X. XXXXXXX for his tremendous inspiration and guidance during my last year as an undergraduate student. Thank you for helping me doing this trip.

Finally, the three women of my life, my mother, my little sister and XXXXXX continue to be my source of endless support. I am sorry for staying away from you for so long time. I dedicate this thesis to my loving mother.

Curriculum Vitae

Nikolaos Gomopoulos

Date of Birth: January 18, 1979
Place of Birth: Athens, Greece
Nationality: Greek

Education

10/2006 - 10/2009

Max Planck Institute for Polymer Research, Mainz, Germany
Promotion by Johannes Gutenberg University Mainz
Degree to be obtained: Doctor in natural science (Dr. rer. nat.)

9/2006- 10/2007

Marie Curie Early Stage Training Fellow
Host Institute: Max Planck Institute for Polymer Research, Mainz, Germany

10/2004 - 7/2006

Institute of Electronic Structure and Laser, F.O.R.T.H, Greece
Department of Materials Science and Technology, University of Crete, Heraklion, Greece
Degree obtained: Master in Materials Science and Technology (M.Sc)
Thesis: Investigation of Model Dendritic Host-Guest Complexes in Chloroform and Aqueous media

10/1997 - 7/2003

Physics Department, University of Ioannina, Greece
Degree obtained: Diploma in Physics
Thesis: Effect of pressure on the segmental dynamics of bisphenol-A-polycarbonate

Publications

[1] Hermans, T. M., Broeren Maarten, A. C., Gomopoulos, N., van der, S., van Genderen-Marcel, H. P., Sommerdijk Nico, A. J.M., Fytas, G., and Meijer, E.W. Self-assembly of soft nanoparticles with tunable patchiness. *Nature Nanotechnology* DOI: 10.1038/nnano.2009.232. (2009).

[2] Gomopoulos, N., Cheng, W., Efremov, M., Nealey, P. F. and Fytas, G. Out-of-Plane Longitudinal Elastic Modulus of Supported Polymer Thin Films. *Macromolecules* **42**, 7164-7167 (2009).

[3] Cheng, W., Gomopoulos, N., Fytas, G., Gorishnyy, T., Walish, J., Thomas, E. L., Hiltner, A., and Baer, E. Phonon dispersion and nanomechanical properties of periodic 1D multilayer polymer films. *Nano Lett* **8**, 1423-1428 (2008).

[4] Hermans, T. M., Broeren, M. A. C., Gomopoulos, N., Smeijers, A. F., Mezari, B.,Van Leeuwen, E. N. M., Vos, M. R. J., Magusin, P. C. M. M., Hilbers, P. A. J., Van Gen-deren, M. H. P., Sommerdijk, N. A. J. M., Fytas, G., and Meijer, E. W. . Stepwise noncovalent synthesis leading to dendrimer-based assemblies in water. *J Am Chem Soc* **129**, 15631-15638 (2007).

[5] Mpoukouvalas, K., Gomopoulos, N., Floudas, G., Herrmann, C., Hanewald, A., and Best, A. Effect of pressure on the segmental dynamics of bisphenol-A-polycarbonate. *Polymer* **47**, 7170-7177 (2006).

Publications in Preparation

[6] Gomopoulos, N., Papadopoulos, P., Kremer, F. and Fytas, G. Spider silk: A soft solid with a unidirectional phononic band gap. *submitted to Nature Materials*

[7] N. Gomopoulos, G. Saini, M. Efremov, P. F. Nealey, K. Nelson, G. Fytas. Non-destructive probing of mechanical anisotropy in polyimide films at nanoscale. *submitted to Macromolecules.*

[8] N. Gomopoulos, D. Maschke, C.Y.Koh, E. L. Thomas, W. Tremel, H.-J. Butt, G. Fytas A facile platform for realization 1D hypersonic phononic crystals.

[9] Gomopoulos, N., Koh, H., Thomas, E. L., E.Baer, E. and Fytas, G. 1D polymer based phononic structures: From multilayers to oligolayers.

[10] P. Voudouris, N. Gomopoulos, A. Le Grand, N. Hadjichristidis, G. Floudas, G. Fytas. Does Brillouin light scattering probe the primary glass transition process at temperature well above glass transition? *submitted to J.Chem.Phys.*

[11] Voudouris P., Gomopoulos N., Sainidou R., Choi J., Dong H., Bockstaller M.R., Matyjaszewski K. and Fytas G. Elastic properties of polymer-coated particle thin films along the main directions

A. appendix

When the scattering wavevector **q** is calculated for both the transmission and the reflection geomtries in the case of a film, **q** as a funcion of the scattering angle is essentially obtained from Snell's law at each boundary and the trigonometric operations. Figure A.1 shows both the transmission and the reflection geometries for the scattering wavevector calculation.

A.0.1. in-plane

Consider the scattering wavevector for the transmission geometry shown in Fig. A.1(a). Let the incident and the refraction at the air/film boundary be respectively α and β, while γ and δ at the film/air boundary, respectively. Geometrically, the real scattering angle Θ and the

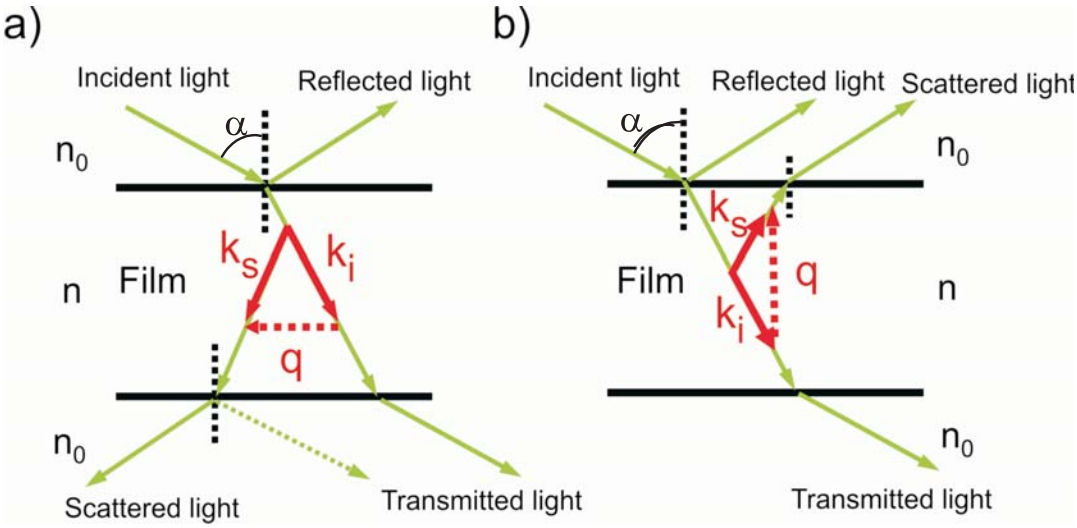

Figure A.1.: Schematics of the scattering geometry: (a) transmission geometry and (b) reflection geometry.

refraction angle γ at the second boundary can be expressed as

$$\Theta = \beta + \gamma \quad \text{(A.1)}$$

$$\delta = \theta - \alpha \quad \text{(A.2)}$$

According to Snell's law, the refraction angle β and the incident angle γ can be expressed as

$$\beta = \sin^{-1}\left(\frac{1}{n}\sin\alpha\right) \tag{A.3}$$

$$\gamma = \sin^{-1}\left(\frac{1}{n}\sin\delta\right) = \sin^{-1}\left\{\frac{1}{n}\sin(\theta-\alpha)\right\} \tag{A.4}$$

The real scattering angle Θ is expressed from Equations A.1, A.3 and A.4 as

$$\Theta = \beta + \gamma = \sin^{-1}\left(\frac{1}{n}\sin\alpha\right) + \sin^{-1}\left\{\frac{1}{n}\sin\left(\theta-\alpha\right)\right\} \tag{A.5}$$

Consequently, the scattering wavevector *q* becomes

$$q = \frac{4\pi n}{\lambda}\sin\left(\frac{\Theta}{2}\right) = \frac{4\pi n}{\lambda}\sin\left[\frac{1}{2}\left\{\sin^{-1}\left(\frac{1}{n}\sin\alpha\right) - \sin^{-1}\left\{\frac{1}{n}\sin(\theta-\alpha)\right\}\right\}\right] \tag{A.6}$$

The perpendicular component of the scattering wavevector $q_\perp$ is then expressed as

$$q_\perp = q\cdot\cos\left(\frac{\beta-\gamma}{2}\right) = q\cos\left[\frac{1}{2}\left\{\sin^{-1}\left(\frac{1}{n}\sin\alpha\right) - \sin^{-1}\left\{\frac{1}{n}\sin(\theta-\alpha)\right\}\right\}\right] \tag{A.7}$$

Therefore, the final form of the scattering wavevector $q_\perp$ for the "*in-plane*" is expressed from Equations A.6 and A.7 as

$$\begin{aligned} q_\perp = \frac{4\pi n}{\lambda}\sin&\left[\frac{1}{2}\left\{\sin^{-1}\left(\frac{1}{n}\sin\alpha\right) + \sin^{-1}\left\{\frac{1}{n}\sin(\theta-\alpha)\right\}\right\}\right] \\ &\times\cos\left[\frac{1}{2}\left\{\sin^{-1}\left(\frac{1}{n}\sin\alpha\right) - \sin^{-1}\left\{\frac{1}{n}\sin(\theta-\alpha)\right\}\right\}\right] \end{aligned} \tag{A.8}$$

For the transmission geometry, when $\alpha = \theta/2$, namely the incident angle is half of the scattering angle,

$$q_\perp = \frac{4\pi n}{\lambda}\sin\left[\sin^{-1}\left(\frac{1}{n}\sin\frac{\theta}{2}\right)\right] \tag{A.9}$$

A.0.2. out-of-plane

Consider the scattering wavevector for the reflection geometry as shown in Fig. A.1(b). Unlike the transmission geometry, light incident on the upper boundary is only considered. As is the case with the transmission geometry, let the incident and the refraction at the air/film boundary be respectively α and β, while γ and δ at the film/air boundary, respectively. Geometrically, the real scattering angle Θ and the refraction angle γ at the second boundary can be expressed

as

$$\Theta = \pi - \beta + \gamma \tag{A.10}$$
$$\delta = \pi - \theta - \alpha \tag{A.11}$$

According to Snell's law, the refraction angle β and the incident angle γ can be expressed as

$$\beta = \sin^{-1}\left(\frac{1}{n}\sin\alpha\right) \tag{A.12}$$
$$\gamma = \sin^{-1}\left(\frac{1}{n}\sin\delta\right) = \sin^{-1}\left\{\frac{1}{n}\sin(\theta+\alpha)\right\} \tag{A.13}$$

Consequently, the scattering wavevector *q* becomes

$$q = \frac{4\pi n}{\lambda}\sin\left(\frac{\Theta}{2}\right) = \frac{4\pi n}{\lambda}\cos\left[\frac{1}{2}\sin^{-1}\left(\frac{1}{n}\sin\alpha\right) + \frac{1}{2}\sin^{-1}\left\{\frac{1}{n}\sin(\theta+\alpha)\right\}\right] \tag{A.14}$$

The parallel component of the scattering wavevector $q_{\|}$ is then expressed as

$$q_{\|} = q\cdot\cos\left(\frac{\beta-\gamma}{2}\right) = q\cdot\cos\left[\frac{1}{2}\sin^{-1}\left(\frac{1}{n}\sin\alpha\right) - \frac{1}{2}\sin^{-1}\left\{\frac{1}{n}\sin(\theta+\alpha)\right\}\right] \tag{A.15}$$

Therefore, the final form of the scattering wavevector $q_{\|}$ for the "*out-of-plane*" is expressed from Equations A.14 and A.15 as

$$\begin{aligned} q_{\|} = \frac{4\pi n}{\lambda}\cos&\left[\frac{1}{2}\sin^{-1}\left(\frac{1}{n}\sin\alpha\right) + \frac{1}{2}\sin^{-1}\left\{\frac{1}{n}\sin(\theta+\alpha)\right\}\right] \\ &\times\cos\left[\frac{1}{2}\sin^{-1}\left(\frac{1}{n}\sin\alpha\right) - \frac{1}{2}\sin^{-1}\left\{\frac{1}{n}\sin(\theta+\alpha)\right\}\right] \end{aligned} \tag{A.16}$$

Bibliography

[1] Nalwa, H. S. *Handbook of nanostructured materials and nanotechnology*. San Diego, (2000).

[2] Whitesides, G. M. *Small* **1**(2), 172–179 (2005).

[3] Alivisatos, A. P. *Science* **271**(5251), 933–937 (1996).

[4] Trindade, T., O'Brien, P., and Pickett, N. L. *Chemistry of Materials* **13**(11), 3843–3858 (2001).

[5] Frank, B., Gast, A. P., Russell, T. P., Brown, H. R., and Hawker, C. *Macromolecules* **29**(20), 6531–6534 (1996).

[6] Hall, D. B. and Torkelson, J. M. *Macromolecules* **31**(25), 8817–8825 (1998).

[7] Forrest, J. A. and Dalnoki-Veress, K. *Advances in Colloid and Interface Science* **94**(1-3), 167–196 (2001).

[8] Cao, G. *Nanostructures and nanomaterials: synthesis, properties and applications*. Imperial College Press, London, (2004).

[9] Alcoutlabi, M. and McKenna, G. B. *Journal of Physics-Condensed Matter* **17**(15), R461–R524 (2005).

[10] Alba-Simionesco, C., Coasne, B., Dosseh, G., Dudziak, G., Gubbins, K. E., Radhakrishnan, R., and Sliwinska-Bartkowiak, M. *Journal of Physics-Condensed Matter* **18**(6), R15–R68 (2006).

[11] Nealey, P. F., Cohen, R. E., and Argon, A. S. *Macromolecules* **26**(6), 1287–1292 (1993).

[12] Nealey, P. F., Cohen, R. E., and Argon, A. S. *Macromolecules* **27**(15), 4193–4197 (1994).

[13] Bohme, T. R. and de Pablo, J. J. *Journal of Chemical Physics* **116**(22), 9939–9951 (2002).

[14] Yoshimoto, K., Jain, T. S., Nealey, P. F., and de Pablo, J. J. *Journal of Chemical Physics* **122**(14), – (2005).

[15] Yoshimoto, K., Papakonstantopoulos, G. J., Lutsko, J. F., and de Pablo, J. J. *Physical Review B* **71**(18), – (2005).

[16] Yoshimoto, K., Jain, T. S., Workum, K. V., Nealey, P. F., and de Pablo, J. J. *Physical Review Letters* **93**(17), – (2004).

[17] Varnik, F., Baschnagel, J., and Binder, K. *Journal of Chemical Physics* **113**(10), 4444–4453 (2000).

[18] Factor, B. J., Russell, T. P., and Toney, M. F. *Physical Review Letters* **66**(9), 1181–1184 (1991).

[19] Joannopoulos, J. D., Villeneuve, P. R., and Fan, S. H. *Nature* **387**(6635), 830–830 (1997).

[20] Meade, R. D., Brommer, K. D., Rappe, A. M., and Joannopoulos, J. D. *Applied Physics Letters* **61**(4), 495–497 (1992).

[21] Meade, R. D., Rappe, A. M., Brommer, K. D., and Joannopoulos, J. D. *Journal of the Optical Society of America B-Optical Physics* **10**(2), 328–332 (1993).

[22] Meade, R. D., Rappe, A. M., Brommer, K. D., Joannopoulos, J. D., and Alherhand, O. L. *Physical Review B* **55**(23), 15942–15942 (1997).

[23] Robertson, W. M., Arjavalingam, G., Meade, R. D., Brommer, K. D., Rappe, A. M., and Joannopoulos, J. D. *Physical Review Letters* **68**(13), 2023–2026 (1992).

[24] Robertson, W. M., Arjavalingam, G., Meade, R. D., Brommer, K. D., Rappe, A. M., and Joannopoulos, J. D. *Optics Letters* **18**(7), 528–530 (1993).

[25] Yablonovitch, E. and Gmitter, T. J. *Solid-State Electronics* **35**(3), 261–267 (1992).

[26] Yablonovitch, E., Gmitter, T. J., Leung, K. M., Meade, R. D., Rappe, A. M., Brommer, K. D., and Joannopoulos, J. D. *Optical and Quantum Electronics* **24**(2), S273–S283 (1992).

[27] Yablonovitch, E., Gmitter, T. J., Meade, R. D., Rappe, A. M., Brommer, K. D., and Joannopoulos, J. D. *Physical Review Letters* **67**(24), 3380–3383 (1991).

[28] Yablonovitch, E., Gmitter, T. J., Meade, R. D., Rappe, A. M., Brommer, K. D., and Joannopoulos, J. D. *Physical Review Letters* **67**(24), 3380–3383 (1991).

[29] Kushwaha, M. S. and Halevi, P. *Applied Physics Letters* **64**(9), 1085–1087 (1994).

[30] Kushwaha, M. S. and Halevi, P. *Applied Physics Letters* **69**(1), 31–33 (1996).

[31] Kushwaha, M. S., Halevi, P., Dobrzynski, L., and Djafarirouhani, B. *Physical Review Letters* **71**(13), 2022–2025 (1993).

[32] Kushwaha, M. S., Halevi, P., Dobrzynski, L., and Djafarirouhani, B. *Physical Review Letters* **75**(19), 3581–3581 (1995).

[33] Vasseur, J. O., Djafarirouhani, B., Dobrzynski, L., Kushwaha, M. S., and Halevi, P. *Journal of Physics-Condensed Matter* **6**(42), 8759–8770 (1994).

[34] Cheng, W., Wang, J. J., Jonas, U., Fytas, G., and Stefanou, N. *Nature Materials* **5**(10), 830–836 (2006).

[35] Still, T., Cheng, W., Retsch, M., Sainidou, R., Wang, J., Jonas, U., Stefanou, N., and Fytas, G. *Physical Review Letters* **100**(19), 194301–4 (2008).

[36] Douglas, T., Strable, E., Willits, D., Aitouchen, A., Libera, M., and Young, M. *Advanced Materials* **14**(6), 415–+ (2002).

[37] Douglas, T. and Young, M. *Nature* **393**(6681), 152–155 (1998).

[38] Douglas, T. and Young, M. *Science* **312**(5775), 873–875 (2006).

[39] Juhl, S. B., Chan, E. P., Ha, Y. H., Maldovan, M., Brunton, J., Ward, V., Dokland, T., Kalmakoff, J., Farmer, B., Thomas, E. L., and Vaia, R. A. *Advanced Functional Materials* **16**(8), 1086–1094 (2006).

[40] Nedoluzhko, A. and Douglas, T. *Physics and Chemistry Basis of Biotechnology, Vol 7* **7**, 9–45 334 (2001).

[41] Nedoluzhko, A. and Douglas, T. *Journal of Inorganic Biochemistry* **84**(3-4), 233–240 (2001).

[42] Tseng, R. J., Tsai, C. L., Ma, L. P., and Ouyang, J. Y. *Nature Nanotechnology* **1**(1), 72–77 (2006).

[43] Miller, R. A., Presley, A. D., and Francis, M. B. *Journal of the American Chemical Society* **129**(11), 3104–3109 (2007).

[44] Yoo, P. J., Nam, K. T., Qi, J. F., Lee, S. K., Park, J., Belcher, A. M., and Hammond, P. T. *Nature Materials* **5**(3), 234–240 (2006).

[45] Nam, K. T., Kim, D. W., Yoo, P. J., Chiang, C. Y., Meethong, N., Hammond, P. T., Chiang, Y. M., and Belcher, A. M. *Science* **312**(5775), 885–888 (2006).

[46] Landau, L. D. and Lifshitz, E. M. *Elasticity Theory*. Akademie-Verlag, (1983).

[47] Farnell, G. W. and Adler, E. L. *Elastic wave propagation in thin layers*. In Physical acoustics, principles and methods. Mason, W. P Thurston, R. N, New York, (1972).

[48] Sanderco.Jr. *Physical Review Letters* **28**(4), 237 (1972).

[49] Sanderco.Jr. *Physical Review Letters* **29**(26), 1735 (1972).

[50] Forrest, J. A., DalnokiVeress, K., Stevens, J. R., and Dutcher, J. R. *Physical Review Letters* **77**(10), 2002–2005 (1996).

[51] Hartschuh, R., Ding, Y., Roh, J. H., Kisliuk, A., Sokolov, A. P., Soles, C. L., Jones, R. L., Hu, T. J., Wu, W. L., and Mahorowala, A. P. *Journal of Polymer Science Part B-Polymer Physics* **42**(6), 1106–1113 (2004).

[52] Rogers, J. A., Maznev, A. A., Banet, M. J., and Nelson, K. A. *Annual Review of Materials Science* **30**, 117–157 (2000).

[53] Patterson, G. D. *Annual Review of Materials Science* **13**, 219–245 (1983).

[54] Krbecek, H., Kruger, J. K., and Pietralla, M. *Journal of Polymer Science Part B-Polymer Physics* **31**(11), 1477–1485 (1993).

[55] Kumar, S. R., Renusch, D. P., and Grimsditch, M. *Macromolecules* **33**(5), 1819–1826 (2000).

[56] Cheng, W., Sainidou, R., Burgardt, P., Stefanou, N., Kiyanova, A., Efremov, M., Fytas, G., and Nealey, P. F. *Macromolecules* **40**(20), 7283–7290 (2007).

[57] Cocson, J. K., Hau, C. S., Lee, P. M., Poon, C. C., Zhong, A. H., Rogers, J. A., and Nelson, K. A. *Polymer* **36**(21), 4069–4075 (1995).

[58] Dhar, L., Rogers, J. A., Nelson, K. A., and Trusell, F. *Journal of Applied Physics* **77**(9), 4431–4444 (1995).

[59] Sun, L., Dutcher, J. R., Giovannini, L., Nizzoli, F., Stevens, J. R., and Ord, J. L. *Journal of Applied Physics* **75**(11), 7482–7488 (1994).

[60] Forrest, J. A., Rowat, A. C., DalnokiVeress, K., Stevens, J. R., and Dutcher, J. R. *Journal of Polymer Science Part B-Polymer Physics* **34**(17), 3009–3016 (1996).

[61] Dil, J. G., van Hijningen, N. C. J. A., van Dorst, F., and Aarts, R. M. *Appl. Opt.* **20**(8), 1374–1381 (1981).

[62] Gomopoulos, N., Cheng, W., Efremov, M., Nealey, P. F., and Fytas, G. *Macromolecules* **42**(18), 7164–7167 (2009).

[63] Hartschuh, R. D., Kisliuk, A., Novikov, V., Sokolov, A. P., Heyliger, P. R., Flannery, C. M., Johnson, W. L., Soles, C. L., and Wu, W. L. *Applied Physics Letters* **87**(17), – (2005).

[64] Bandhu, R. S., Zhang, X., Sooryakumar, R., and Bussmann, K. *Physical Review B* **70**(7), – (2004).

[65] Van Workum, K. and de Pablo, J. J. *Nano Letters* **3**(10), 1405–1410 (2003).

[66] Herminghaus, S., Boese, D., Yoon, D. Y., and Smith, B. A. *Applied Physics Letters* **59**(9), 1043–1045 (1991).

[67] Factor, B. J., Russell, T. P., and Toney, M. F. *Faraday Discussions* (98), 319–327 (1994).

[68] Russell, T. P., Gugger, H., and Swalen, J. D. *Journal of Polymer Science Part B-Polymer Physics* **21**(9), 1745–1756 (1983).

[69] Lin, L. and Bidstrup, S. A. *Journal of Applied Polymer Science* **49**(7), 1277–1289 (1993).

[70] Hinrichs, K. and Eichhorn, J. *Spectroscopy Europe* **19**, 11–14 (2007).

[71] Diao, J. and Hess, D. W. *Thin Solid Films* **483**(1-2), 226–231 (2005).

[72] Hinrichs, K., Tsankov, D., Korte, E. H., Roseler, A., Sahre, K., and Eichhorn, K. J. *Applied Spectroscopy* **56**(6), 737–743 (2002).

[73] Sahre, K., Eichhorn, K. J., Simon, F., Pleul, D., Janke, A., and Gerlach, G. *Surface and Coatings Technology* **139**(2-3), 257–264 (2001).

[74] Rogers, J. A., Dhar, L., and Nelson, K. A. *Applied Physics Letters* **65**(3), 312–314 (1994).

[75] Rogers, J. A., Yang, Y., and Nelson, K. A. *Applied Physics a-Materials Science and Processing* **58**(5), 523–534 (1994).

[76] Liou, H. C., Willecke, R., and Ho, P. S. *Thin Solid Films* **323**(1-2), 203–208 (1998).

[77] Kurabayashi, K. and Goodson, K. E. *Journal of Applied Physics* **86**(4), 1925–1931 (1999).

[78] Morikawa, J. and Hashimoto, T. *Journal of Applied Physics* **105**(11), – (2009).

[79] Wilson, A. 715. Plenum, New York (1984).

[80] Senturia, S. D. In *American Chemical Society Symposium*, Bowden.J and Turner.S.R, editors (, Washington, DC, 1987).

[81] Yokota.R. In *Proceedings of 1st Oxford Kobe Materials* (, St.Catherines College Kobe Institute, 1998).

[82] PI-2600 Series Low Stress Polyimides, HD MicroSystems 250 Cheesequake Road, Parlin, NJ 08859-1241, www.hdmicrosystems.com.

[83] Auld, B. A. *Acoustic fields and waves in solids*, volume II. Krieger: Malabar, 2 edition, (1990).

[84] Baer, E., Hiltner, A., and Keith, H. D. *Science* **235**(4792), 1015–1022 (1987).

[85] Liu, R. Y. F., Jin, Y., Hiltner, A., and Baer, E. *Macromolecular Rapid Communications* **24**(16), 943–948 (2003).

[86] Weber, M. F., Stover, C. A., Gilbert, L. R., Nevitt, T. J., and Ouderkirk, A. J. *Science* **287**(5462), 2451–2456 (2000).

[87] Bansal, A., Yang, H. C., Li, C. Z., Cho, K. W., Benicewicz, B. C., Kumar, S. K., and Schadler, L. S. *Nature Materials* **4**, 693–698 (2005).

[88] Lee, J. Y., Su, K. E., Chan, E. P., Zhang, Q. L., Ernrick, T., and Crosby, A. J. *Macromolecules* **40**, 7755–7757 (2007).

[89] Sigalas, M., Kushwaha, M. S., Economou, E. N., Kafesaki, M., Psarobas, I. E., and Steurer, W. *Zeitschrift Fur Kristallographie* **220**(9-10), 765–809 (2005).

[90] Gorishnyy, T., Maldovan, M., Ullal, C., and Thomas, E. *Physics World* **18**(12), 24–29 (2005).

[91] Dainese, P., Russell, P. S. J., Joly, N., Knight, J. C., Wiederhecker, G. S., Fragnito, H. L., Laude, V., and Khelif, A. *Nature Physics* **2**(6), 388–392 (2006).

[92] Trigo, M., Bruchhausen, A., Fainstein, A., Jusserand, B., and Thierry-Mieg, V. *Physical Review Letters* **89**(22), 227402/1–4 (2002).

[93] Priadilova, O., Cheng, W., Tommaseo, G., Steffen, W., Gutmann, J. S., and Fytas, G. *Macromolecules* **38**(6), 2321–2326 (2005).

[94] Cheng, W., Gorishnyy, T., Krikorian, V., Fytas, G., and Thomas, E. L. *Macromolecules* **39**, 9614–9620 (2006).

[95] Berne, B. and Pecora, R. *Dynamic light scattering with applications to chemistry, biology and physics*. Dover Publications, New York, (2000).

[96] Urbas, A. M., Thomas, E. L., Kriegs, H., Fytas, G., Penciu, R. S., and Economou, L. N. *Physical Review Letters* **90**(10), 108302/1–501/3 (2003).

[97] Forrest, J. A., Rowat, A. C., DalnokiVeress, K., Stevens, J. R., and Dutcher, J. R. *Journal of Polymer Science Part B-Polymer Physics* **34**(17), 3009–3016 (1996).

[98] Gorishnyy, T., Ullal, C. K., Maldovan, M., Fytas, G., and Thomas, E. L. *Physical Review Letters* **94**(11), 115501/1–4 (2005).

[99] Gorishnyy, T., Maldovan, M., Ullal, C., and Thomas, E. *Physics World* **18**(12), 24–29 (2005).

[100] Joannopoulos, J. D., Meade, R. D., and Winn, J. N. *Photonic Crystals: Molding the Flow of Light*. Princeton Univ. Press, New Jersey, (1995).

[101] Martinez-Sala, R., Sancho, J., Sanchez, J. V., Gomez, V., Llinares, J., and Meseguer, F. *Nature* **378**(6554), 241–241 (1995).

[102] Jang, J. H., Ullal, C. K., Gorishnyy, T., Tsukruk, V. V., and Thomas, E. L. *Nano Letters* **6**(4), 740–743 (2006).

[103] Gorishnyy, T., Ullal, C. K., Maldovan, M., Fytas, G., and Thomas, E. L. *Physical Review Letters* **94**(11), 115501/1–4 (2005).

[104] Cheng, W., Wang, J. J., Jonas, U., Fytas, G., and Stefanou, N. *Nature Materials* **5**(10), 830–836 (2006).

[105] Still, T., Cheng, W., Retsch, M., Sainidou, R., Wang, J., Jonas, U., Stefanou, N., and Fytas, G. *Physical Review Letters* **100**(19), 194301–4 (2008).

[106] Sun, C.-K., Liang, J.-C., and Yu, X.-Y. *Physical Review Letters* **84**(Copyright (C) 2009 The American Physical Society), 179 (2000).

[107] Cheng, W., Gomopoulos, N., Fytas, G., Gorishnyy, T., Walish, J., Thomas, E. L., Hiltner, A., and Baer, E. *Nano Letters* **8**(5), 1423–1428 (2008).

[108] Weber, M. F., Stover, C. A., Gilbert, L. R., Nevitt, T. J., and Ouderkirk, A. J. *Science* **287**(5462), 2451–2456 (2000).

[109] Saini, G., Pezeril, T., Torchinsky, D., J. Yoon, S. K., Thomas, E., and Nelson, K. *J.Mater.Res* **22**(3) (2007).

[110] Sigalas, M., Kushwaha, M. S., Economou, E. N., Kafesaki, M., Psarobas, I. E., and Steurer, W. *Zeitschrift Fur Kristallographie* **220**(9-10), 765–809 (2005).

[111] Trigo, M., Bruchhausen, A., Fainstein, A., Jusserand, B., and Thierry-Mieg, V. *Physical Review Letters* **89**(22), 227402/1–4 (2002).

[112] Dainese, P., Russell, P. S. J., Joly, N., Knight, J. C., Wiederhecker, G. S., Fragnito, H. L., Laude, V., and Khelif, A. *Nature Physics* **2**(6), 388–392 (2006).

[113] Baer, E., Hiltner, A., and Keith, H. D. *Science* **235**(4792), 1015–1022 (1987).

[114] Easterling, K. E., Harrysson, R., Gibson, L. J., and Ashby, M. F. *Proceedings of the Royal Society of London. A. Mathematical and Physical Sciences* **383**(1784), 31–41 (1982).

[115] Vollrath, F. and Knight, D. P. *Nature* **410**(6828), 541–548 (2001).

[116] Vollrath, F., Madsen, B., and Shao, Z. *Proceedings of the Royal Society of London. Series B: Biological Sciences* **268**(1483), 2339–2346 (2001).

[117] Jin, H. J. and Kaplan, D. L. *Nature* **424**(6952), 1057–1061 (2003).

[118] Lefevre, T., Boudreault, S., Cloutier, C., and Pzolet, M. *Biomacromolecules* **9**(9), 2399–2407 (2008).

[119] Heim, M., Keerl, D., and Scheibel, T. *Angewandte Chemie-International Edition* **48**(20), 3584–3596 (2009).

[120] Rammensee, S., Slotta, U., Scheibel, T., and Bausch, A. R. *Proceedings of the National Academy of Sciences of the United States of America* **105**(18), 6590–6595 (2008).

[121] Scheibel, T. *Microbial Cell Factories* **3**(1), 14 (2004).

[122] Glisović, A., Vehoff, T., Davies, R. J., and Salditt, T. *Macromolecules* **41**(2), 390–398 (2008).

[123] Sponner, A., Unger, E., Grosse, F., and Klaus, W. *Nature Materials* **4**(10), 772–775 (2005).

[124] Sapede, D., Seydel, T., Forsyth, V. T., Koza, M. A., Schweins, R., Vollrath, F., and Riekel, C. *Macromolecules* **38**(20), 8447–8453 (2005).

[125] Thiel, B. L., Guess, K. B., and Viney, C. *Biopolymers* **41**(7), 703–719 (1997).

[126] Rousseau, M. E., Cruz, D. H., West, M. M., Hitchcock, A. P., and Pezolet, M. *Journal of the American Chemical Society* **129**(13), 3897–3905 (2007).

[127] Miller, L. D., Putthanarat, S., Eby, R. K., and Adams, W. W. *International Journal of Biological Macromolecules* **24**(2-3), 159–165 (1999).

[128] Gersappe, D. *Physical Review Letters* **89**(Copyright (C) 2009 The American Physical Society), 058301 (2002).

[129] Ene, R., Papadopoulos, P., and Kremer, F. *Soft Matter* (2009).

[130] Yang, Y., Chen, X., Shao, Z. Z., Zhou, P., Porter, D., Knight, D. P., and Vollrath, F. *Advanced Materials* **17**(1), 84–+ (2005).

[131] Lee, S. M., Pippel, E., Gosele, U., Dresbach, C., Qin, Y., Chandran, C. V., Brauniger, T., Hause, G., and Knez, M. *Science* **324**(5926), 488–492 (2009).

[132] Liu, Y., Shao, Z. Z., and Vollrath, F. *Nature Materials* **4**(12), 901–905 (2005).

[133] Papadopoulos, P., Slter, J., and Kremer, F. *Colloid & Polymer Science* **287**(2), 231–236 (2009).

[134] Porter, D., Vollrath, F., and Shao, Z. *European Physical Journal E* **16**(2), 199–206 (2005).

[135] Papadopoulos, P., Ene, R., Weidner, I., and Kremer, F. *Macromolecular Rapid Communications* **30**(9-10), 851–857 (2009).

[136] Fossey, S., Kaplan, D., and Mark, E. J. E. In *Polymer Data Handbook*. Oxford University Press (1999).

[137] Cheng, W., Wang, J. J., Jonas, U., Fytas, G., and Stefanou, N. *Nature Materials* **5**(10), 830–836 (2006).

[138] Seidel, A., Liivak, O., and Jelinski, L. W. *Macromolecules* **31**(19), 6733–6736 (1998).

[139] Chen, X., Shao, Z., Marinkovic, N. S., Miller, L. M., Zhou, P., and Chance, M. R. *Biophysical Chemistry* **89**(1), 25–34 (2001).

[140] Gorishnyy, T., Jang, J.-H., Koh, C., and Thomas, E. L. *Applied Physics Letters* **91**(12), 121915–3 (2007).

[141] Sharma, V., Crne, M., Park, J. O., and Srinivasarao, M. *Science* **325**(5939), 449–451 (2009).

[142] Porter, D. and Vollrath, F. *Advanced Materials* **21**(4), 487–492 (2009).